New Developments in Fermionic Many-Body Physics within Time-Dependent Density Functional Theory

Matthew Kafker

A dissertation
submitted in partial fulfillment of the
requirements for the degree of

Doctor of Philosophy

University of Washington
2025

Reading Committee:
Aurel Bulgac, Chair
Alejandro Garcia
Gerald A. Miller

Program Authorized to Offer Degree:
Physics

University of Washington

Abstract

New Developments in Fermionic Many-Body Physics within Time-Dependent Density Functional Theory

Matthew Kafker

Chair of Supervisory Committee:

Aurel Bulgac

Department of Physics

This thesis documents various recent developments in the physics of systems composed of many strongly interacting fermions, obtained within time-dependent density functional theory, which is a leading microscopic approach for the treatment of the non-equilibrium dynamics of such systems. Various aspects of the problem of nuclear fission are addressed, in particular focusing on the stage of evolution from the outer saddle of the nuclear potential energy surface, through the scission point, and beyond until full separation between the fragments is achieved, for a variety of actinide nuclei. The dynamics of neck rupture during nuclear fission are presented, and it is argued that scission neutrons are expected to be released during this stage. The saddle-to-scission dynamics of nuclei with an odd number of neutrons, and in some cases also an odd number of protons, are presented, which reveal a highly complex nuclear shape evolution and enhanced effects of time-reversal symmetry breaking in such odd systems. The intrinsic spins of the fission fragments are evaluated after scission, and it is found that, with significant probability, the spins are not oriented perpendicular to the fission axis and that their directions in space are correlated. Various aspects of the dynamics of the single-particle occupation numbers, which change in time due to the pairing interaction, are addressed, and these are used to define a notion of complexity for quantum many-body systems. It is also demonstrated that the occupation numbers evolve in time as a non-Markovian stochastic process, both in the case of fission dynamics and also in the case of quantum turbulence and subsequent thermalization of the unitary Fermi gas. Various aspects of the problem of restoring translational invariance of the many-body wave function within density functional theory are presented. Finally, preliminary results are presented concerning the problem of multi-nucleon transfer reactions, treated within time-dependent density functional theory.

CONTENTS

I. ORGANIZATION

During the course of my Ph.D., I have been a coauthor on 10 papers:

- "Non-Equilibrium Dynamics of Hard Spheres in the Fluid, Crystalline, and Glassy Regimes," M. Kafker, X. Arsiwalla, Phys. Rev. E **112**, 034103 (2025) (Editor's Suggestion), https://arxiv.org/abs/2504.04599, (2025) [1].

- "Time-Dependent Density Functional Theory Description of ^{238}U(n,f), ^{240,242}Pu(n,f) and ^{237}Np(n,f) Reactions," A. Bulgac, I. Abdurrahman, M. Kafker, I. Stetcu, Phys. Rev. Lett. **135**, 062501 (2025), https://arxiv.org/abs/2503.24268, (2025) [2].

- "Impact of the Center of Mass Fluctuations on the Ground State Properties of Nuclei," M. Kafker, A. Bulgac, https://arxiv.org/abs/2503.09470, (2025), submitted to Phys. Rev. C [3].

- "Non-Equilibrium Aspects of Fission Dynamics within the Time Dependent Density Functional Theory," A. Bulgac, M. Kafker, I. Abdurrahman, I. Stetcu, EPJ Web of Conferences 322, 07002 (2025) https://arxiv.org/pdf/2411.03546, (2024) [4].

- "Quantum turbulence, superfluidity, non-Markovian dynamics, and wave function thermalization," A. Bulgac, M. Kafker, I. Abdurrahman, G. Wlazlowski, Phys. Rev. Research **6**, L042003 (2024), https://arxiv.org/pdf/2406.00926 (2024) [5].

- "Neck rupture and scission neutrons in nuclear fission," I. Abdurrahman, M. Kafker, A.. Bulgac, I. Stetcu, Phys. Rev. Lett. **132**, 242501 (2024), https://arxiv.org/pdf/2307.13132 [6].

- "Non-Markovian character and irreversibility of real-time quantum many-body dynamics," A. Bulgac, M. Kafker, I. Abdurrahman, I. Stetcu, Phys. Rev. C **109**, 064617 (2024), https://arxiv.org/pdf/2312.14962 [7].

- "Microscopic evidence for scission neutrons," I. Abdurrahman, M. Kafker, A. Bulgac, I. Stetcu, EPJ Web of Conferences 292, 08008 (2024) [8].

- "Spatial orientation of the fission fragment intrinsic spins and their correlations," G. Scamps, I. Abdurrahman, M. Kafker, A. Bulgac, I. Stetcu, Phys. Rev. C **108**, L061602 (2023), https://arxiv.org/pdf/2307.14455 [9].

- "Measures of complexity and entanglement in many-fermion systems," A. Bulgac, M. Kafker, I. Abdurrahman, Phys. Rev. C **107**, 044318 (2023), https://arxiv.org/pdf/2203.04843 [10].

All but one of these has been published, and the only unpublished one is currently under review. Excluding the conference proceedings and the Phys. Rev. E paper (which covers very different subject matter), each of these papers will receive its own chapter in this thesis. The thesis opens with an introductory chapter which sets the stage for the rest of the thesis, and in the final chapter some preliminary results from ongoing work are presented.

II. ACKNOWLEDGEMENTS

It has been one of the great adventures—and great privileges—of my life to spend the last few years working on this Ph.D., and I am deeply grateful to a number of people, without whom its completion would have been impossible.

I would like to thank my parents for their unwavering love, extremely generous support, and impeccable guidance, which have meant the world to me, and which have been an indispensable help to me during graduate school and throughout my whole life.

I would like to thank Aurel Bulgac for giving me an opportunity to learn theoretical physics, which has been a dream of mine for more than a decade, and for pushing me to discover my limits, as well as for his exceptional leadership and kindness.

I would like to thank Catherine Provost and Larry Yaffe, whose timely help and outstanding compassion saved my Ph.D. and found me a path forward when I could not see one myself. I would also like to thank Catherine Provost for going above and beyond to make me feel welcome in the Physics Department from the moment I first arrived at UW.

I would like to thank Ionel Stetcu and Ibrahim Abdurrahman for a very positive, productive, educational, supportive, and friendly collaboration over the last several years.

And finally, I would like to thank Kaia, Luna, and Bluebert Pancake, for sharing with me a life full of love and fun, and for helping me keep the most important things in perspective.

In loving memory of Frank A. Kafker —

I wish you could have read it.

III. INTRODUCTION

A. The Quantum Many-Body Problem

Fermions are particles which obey the laws of quantum mechanics and which also respect the Pauli exclusion principle, meaning that only one fermion can occupy any given quantum state at a time. A few familiar examples of fermions are electrons, protons, and neutrons, and so the properties of most common terrestrial forms of matter, including atoms, molecules, many aspects of materials, and atomic nuclei, as well as certain kinds of ultra-cold atomic gases, can all be understood as following from the behavior of systems composed of many (mutually interacting) fermions.

The quantum mechanical description of a system of many particles is accomplished through the use of a many-body wave function (MBWF), which is a function over the configuration space of the system, and hence depends on N spatial coordinates for an N particle system. (We will neglect particle spins for this discussion.) If one wishes to describe the behavior of a quantum many-body system such as a nucleus of Uranium-236, a system which we will consider in great detail in this thesis, ideally one could simply calculate the many-body wave function for this system; however, a simple argument reveals that this is impossible. Suppose we want to represent the MBWF on a computer, in which case a common strategy is to discretize space into a three dimensional grid of points, and then the goal is to calculate the values of the MBWF at just those points. If we choose a $10 \times 10 \times 10$ grid of points, we now must calculate the values of the many-body wave function $\Psi(\mathbf{r}_1, \ldots, \mathbf{r}_{236})$ over this grid, where $\mathbf{r}_i$ refers to the position of particle i. However, each coordinate $\mathbf{r}_i$ can take on $10^3 = 1,000$ different values, independent from all the other coordinates, so in the most general case, specifying the full many-body wave function would require

$$\left(10^3\right)^{236} \approx 10^{700} \text{ complex numbers!} \tag{1}$$

If one compares this number to the number of atoms in the universe, which is roughly 10^{80}, it is clear that it is impossible to directly represent the many-body wave function for a many-fermion system consisting of more than just a few particles, and so another strategy must be employed.

B. Mean Field Theory

One solution which works fairly well in practice is to use a mean field theory, in which one assumes that the cumulative effect of the highly complex forces acting between all the various nucleons (protons and neutrons) within the nucleus is to create an average potential in which all the nucleons move approximately independently. One can derive a mean field theory by starting with a Hamiltonian for an interacting many-body system, for example,

$$\hat{H} = \sum_i \frac{\hat{\mathbf{p}}_i^2}{2m} + \sum_{i<j} \hat{V}_2(\mathbf{r}_i, \mathbf{r}_j) \tag{2}$$

and assuming the simplest possible form for the many-body wave function, namely a Slater determinant

$$\Psi(\mathbf{r}_1, \ldots, \mathbf{r}_{236}) = \frac{1}{\sqrt{A!}} \det \psi_i(\mathbf{r}_j), \tag{3}$$

where $\{\psi_i(\mathbf{r})\}_{i=1}^A$ is the set of single-particle wave functions composing the Slater determinant. Invoking the variational principle, we know that

$$E = \langle \Psi | \hat{H} | \Psi \rangle \tag{4}$$

will be an upper bound for the energy of the system. Treating the single particle wave functions $\psi_i(\mathbf{r})$ as variational parameters, we minimize the energy

$$\frac{\delta E}{\delta \psi_i^*(\mathbf{r})} = 0, \tag{5}$$

subject to the condition that the single particle states form an orthonormal set, which can be imposed with Lagrange multipliers. The result of this variational procedure is the Hartree-Fock (HF) equations [11],

$$-\frac{\hbar^2}{2m}\Delta\phi_k(\mathbf{r}) + V_H(\mathbf{r})\phi_k(\mathbf{r}) + \int d^3r' V_F(\mathbf{r}, \mathbf{r}')\phi_k(\mathbf{r}') = E_k\phi_k(\mathbf{r}), \tag{6}$$

where the Hartree potential is given by

$$V_H(\mathbf{r}) = \int d^3r' V_2(\mathbf{r}, \mathbf{r}')\rho(\mathbf{r}'), \quad \rho(\mathbf{r}) = \sum_i |\phi_i(\mathbf{r})|^2 \tag{7}$$

and the Fock potential is given by

$$V_F(\mathbf{r}, \mathbf{r}') = -V_2(\mathbf{r}, \mathbf{r}')\rho(\mathbf{r}, \mathbf{r}'), \quad \rho(\mathbf{r}, \mathbf{r}') = \sum_i \phi_i(\mathbf{r})\phi_i(\mathbf{r}')^*. \tag{8}$$

The wave functions $\phi_i(\mathbf{r})$ were obtained from the original set $\psi_i(\mathbf{r})$ by a unitary transformation while performing the variational procedure, and so a Slater determinant of these new single-particle wave functions only differs from the original Slater determinant by an overall phase factor.

The Hartree-Fock equations are a coupled set of Schrödinger equations which describe a set of A independent particles moving in a potential which is defined by the matter distribution of the system, $\rho(\mathbf{r}, \mathbf{r}')$, and the underlying two-body interaction, and so we have achieved our goal of constructing a mean field theory. Since the matter distribution (i.e., the one body density matrix) is determined in terms of the eigenfunctions of the Hartree-Fock equations according to

$$\rho(\mathbf{r}, \mathbf{r}') = \sum_i \phi_i(\mathbf{r})\phi_i(\mathbf{r}')^*, \tag{9}$$

solving the Hartree-Fock problem amounts to the solving of a system of coupled nonlinear integrodifferential equations. Furthermore, one can obtain the dynamical behavior of this system by replacing

$$E_k \to i\hbar\frac{\partial}{\partial t} \tag{10}$$

in Eq. (6), in which case on obtains the time-dependent Hartree-Fock (TDHF) equations, which look like the standard time-dependent Schrödinger equation in the presence of a mean field potential.

In practice, one can achieve better descriptions of nuclei by proceeding in a slightly different, although related, manner. Namely, rather than starting with a Hamiltonian for the interacting system as in Eq. (2) and determining the energy by evaluating the expectation value of the energy as in Eq. (4), instead one directly postulates a form for the energy (density) in terms of the (number) density distribution of the system, as well as several other relevant densities as needed, including the kinetic energy density, the current density, the spin-current density, the spin density, and for superfluid systems, the anomalous density, which is the superfluid order parameter. These nuclear energy density functionals (NEDFs) often contain a number of fitting parameters and can be thought of in many ways as being analogous to the Lagrangian densities employed in (effective) field theories. One such example of a nuclear energy density functional is the SeaLL1 functional [12], which we will

use in all the nuclear physics studies presented in this thesis,

$$\begin{aligned}\mathcal{E} = \frac{\hbar^2}{2m}(\tau_n + \tau_p) + \\ a_0 n_0^{5/3} + b_0 n_0^2 + c_0 n_0^{7/3} + \\ \left(a_1 n_0^{-1/3} + b_1 + c_1 n_0^{1/3}\right) n_1^2 + \\ \left(a_2 n_0^{-7/3} + b_2 n_0^{-2} + c_2 n_0^{-5/3}\right) n_1^4 + \\ \eta_s \frac{\hbar^2}{2m}\left(|\nabla n_n|^2 + |\nabla n_p|^2\right) + \\ W_0 \mathbf{J} \cdot \nabla n_0 + \\ g_{\text{eff}}(\mathbf{r})\left(|\kappa_p(\mathbf{r})|^2 + |\kappa_n(\mathbf{r})|^2\right) + \\ \frac{e^2}{2}\int d^3r' \frac{n_p(\mathbf{r}) n_p(\mathbf{r}')}{|\mathbf{r} - \mathbf{r}'|} - \frac{e^2\pi}{4}\left(\frac{3}{\pi}\right)^{4/3} n_p^{4/3}.\end{aligned} \tag{11}$$

Here, n stands for the number density, τ for the kinetic energy density, $\mathbf{J}$ for the spin-current density, and κ for the anomalous density. Subscripts "n" and "p" refer to neutron and protons respectively, and $n_0 = n_n + n_p$ and $n_1 = n_n - n_p$. Just as in the Hartree-Fock equations, all the various densities of the system are expressed in terms of the single-particle eigenstates of the resulting Schrödinger equation, and so one must also in this case solve a coupled nonlinear system of equations. One is justified in introducing an energy density functional because of the remarkable Hohenberg-Kohn theorem [13], first formulated for electronic systems, which states in its original form that the solution of the many-body Schrödinger equation is in one-to-one correspondence with the number density of the system, although for the systems we consider, more densities must be included. As the many-body wave function is a function of A spatial coordinates, whereas the densities are all functions of just one coordinate, this density functional theory (DFT) approach is actually computationally feasible, in contrast to directly solving the many-body Schrödinger equation, as we saw above. One challenge of the DFT approach, however, is that the Hohenberg-Kohn theorem is merely an existence proof and does not offer a recipe for actually constructing the energy density functional [13], and so in practice the determination of high quality functionals is a bit of an art form [12].

Nuclear density functional theory, when supplemented to include the pairing interaction (discussed next), is among the most accurate and flexible techniques for calculating static and dynamic properties of nuclei across the entire nuclear chart, and it achieves a root-mean-square (RMS) error when calculating binding energies of between 2 and 3 MeV [12]

without including corrections due to symmetry restoration, see Sec. X. Furthermore, for the heaviest nuclear systems, including the case of the highly non-equilibrium dynamics of neutron induced fission, nuclear density functional theory is the only fully microscopic approach which is capable of providing useful results.

C. Pairing

The density functional theory approach we have introduced is sufficient for calculating the ground state properties of spherical nuclei, as was first shown by Vautherin and Brink in the 1970's using the Skyrme interaction [14]. However, for the cases of open shell nuclei and for dynamics, a further ingredient must be included into microscopic approaches, such as DFT, along with the mean field potential, and that is the pairing interaction, which is a short-range attractive interaction acting between the nucleons. The pairing interaction must be included in nuclear mean field theories because it neatly explains a variety of phenomena which otherwise appear anomalous: a gapped low energy spectrum for even-even nuclei, a lower than expected level density in certain open-shelled nuclei, the odd-even effect in nuclear binding energies, nuclear moments of inertia and deformations (for which one often obtains incorrect estimates in the absence of pairing), and the presence of low-lying 2^+ states for even systems in the vicinity of closed shells [11]. In the 1980's, G. Bertsch realized that pairing is also crucial for nuclear shape dynamics during nuclear fission [15–19] due to its role in redistributing the single-particle occupation numbers as the nucleus deforms.

I now offer a brief review of the pure pairing problem, as I find it helpful when interpreting the many results related to the pairing interaction which will be presented in this thesis. We start by considering just two particles in a nuclear "shell" characterized by single-particle angular momentum $j = l + 1/2$. For the purposes of this exercise, we will forget about the other shells. Within this j-shell, we suppose the particles interact according to the Hamiltonian

$$H_{\text{pairing}} = -G \sum_{m'>0} \sum_{m>0} a^\dagger_{m'} a^\dagger_{-m'} a_{-m} a_m \tag{12}$$

where $G > 0$ is a constant, and $m = -j, -j+1, ..., j-1, j$ is the quantum number for the projection of the angular momentum. Restricting our attention to the subspace spanned by two-particle states of the form $|m, -m\rangle = a^\dagger_m a^\dagger_{-m}|0\rangle$, and applying the anticommutation rules

for fermionic creation and annihilation operators

$$\{a_m, a_{m'}\} = 0, \quad \{a_m^\dagger, a_{m'}^\dagger\} = 0, \quad \{a_m, a_{m'}^\dagger\} = \delta_{m,m'}, \tag{13}$$

it is clear that

$$\langle m, -m | H_{\text{pairing}} | m', -m' \rangle = -G \tag{14}$$

for all m, m' within this subspace. (Note that all other two-particle matrix elements of this Hamiltonian clearly vanish, as they will be killed by the two annihilation operators on the right in the pairing Hamiltonian in Eq. (12). Given that in coordinate space, time-reversed orbitals with quantum numbers m and $-m$ generally have the same spatial profile, it is in this sense that the pairing Hamiltonian corresponds to a short-range attractive interaction.)

Hence, within the two-particle subspace spanned by time-reversed pairs $|m, -m\rangle$, the pairing Hamiltonian is given by a constant matrix of dimensions $\Omega \times \Omega$, where $\Omega = j + 1/2$ is the number of states with $m > 0$, which is simple to diagonalize. There is a unique ground state separated by the other degenerate eigenstates by an energy gap $E = -G\Omega$. The ground state wave function is given by

$$\psi_{\text{Cooper pair}} = \frac{1}{\sqrt{\Omega}} \begin{pmatrix} 1 \\ 1 \\ \vdots \\ 1 \end{pmatrix} \leftrightarrow |\psi_{\text{Cooper pair}}\rangle \propto \sum_{m>0} a_m^\dagger a_{-m}^\dagger |0\rangle \equiv S^+|0\rangle, \tag{15}$$

which is the famous Cooper pair, which plays a central role in the BCS theory of superconductivity [20]. *One crucial aspect of this solution is that in the presence of the pairing interaction, time-reversed pairs of single-particle states are "spread" over the available states. For the mean field theory calculations we present in this thesis, this will be reflected in the single particle occupation numbers, which express the average number of particles found within each single-particle state for a given many-body wave function.* In this case of pure pairing in a degenerate shell, time-reversed pairs are spread uniformly over the available states, but if the levels are no longer degenerate, the Cooper pair wave function still describes a distribution of the single-particle occupation numbers which is instead given by [11]

$$|\psi_{\text{Cooper pair}}\rangle \propto \sum_{m>0} \frac{v_m}{u_m} a_m^\dagger a_{-m}^\dagger |0\rangle \equiv S^+|0\rangle, \tag{16}$$

where $|v_m|^2 \equiv n_m$ are the single particle occupation numbers, which are related to the energies of the single particle states. In the case where we have $N > 2$ particles, but where N is still even, one can show [11] that the ground state (GS) is still unique and has the same pairing gap, and the wave function is given by a "condensate" of $N/2$ Cooper pairs

$$|\mathrm{GS}\rangle \propto (S^+)^{N/2}|0\rangle. \tag{17}$$

In the case where N is odd, which will be important in Sec. V below, the ground state of the pure pairing Hamiltonian will always be degenerate. For $N = 3$, the GS is given by

$$\left(\sum_{m>0, m\neq i} a_m^\dagger a_{-m}^\dagger\right) a_i^\dagger|0\rangle \equiv S^+ a_i^\dagger|0\rangle, \tag{18}$$

where the degeneracy arises because one can choose any state single-particle state i in the shell to "block" without changing the energy. In the case of $N > 3$, with N odd, the ground state is given by

$$|\mathrm{GS}\rangle \propto (S^+)^{(N-1)/2} a_i^\dagger|0\rangle. \tag{19}$$

D. The Time-Dependent Superfluid Local Density Approximation

The theoretical formalism which we use throughout this thesis is an extension of time-dependent density functional theory to include pairing interactions, known as the time-dependent superfluid local density approximation (TDSLDA). The previous discussion of pairing was, as we noted, the simplest possible case. Bardeen, Cooper, and Schrieffer [20] were the first to introduce a highly correlated many-body wave function for describing fermionic superfluids, now known as the BCS wave function,

$$|\mathrm{BCS}\rangle = \prod_{k>0} \left(u_k + v_k a_k^\dagger a_{\overline{k}}^\dagger\right)|0\rangle, \tag{20}$$

where $\overline{k}$ refers to the time-reversal of state k, and one can show that in terms of the generalized pair creation operator

$$S^+ \equiv \sum_{k>0} \frac{v_k}{u_k} a_k^\dagger a_{\overline{k}}^\dagger, \tag{21}$$

the BCS wave function can be written as [11]

$$|\mathrm{BCS}\rangle \propto |0\rangle + S^+|0\rangle + \frac{1}{2}(S^+)^2|0\rangle + \cdots = \exp(S^+)|0\rangle, \tag{22}$$

and so the BCS wave function represents a system with pairing correlations as a superposition of pairing condensates, each with different particle number N. The BCS wave function describes well the case of electronic superconductors, as in this case the pairing correlations are confined to a narrow range of energies around the Fermi level and the single particle states in this interval do not have significant energy dependence. However, in the case of the systems considered in this thesis, which include nuclei, cold atom systems, and also neutron and proton matter in neutron star crusts, the pairing interaction is strong and the mixing occurs between states which are well-separated in energy, and so TDSLDA uses a more general ansatz for the form of the many-body wave function for a system in the presence of pairing correlations [7]. In analogy with a Slater determinant wave function, which in terms of fermionic creation operators is written as

$$|\Psi\rangle = \prod_k a_k^\dagger |0\rangle, \tag{23}$$

the (TD)SLDA many-body wave function is treated as a vacuum with respect to Bogoliubov quasiparticles,

$$|\Phi\rangle \propto \prod_k \alpha_k |0\rangle, \tag{24}$$

where the quasiparticle operators are defined via a unitary Bogoliubov transformation from the standard quantum field operators as

$$\alpha_k^\dagger = \int d\xi \left[u_k(\xi)\psi^\dagger(\xi) + v_k(\xi)\psi(\xi) \right] \tag{25}$$

$$\alpha_k = \int d\xi \left[v_k^*(\xi)\psi(\xi) + u_k^*(\xi)\psi(\xi) \right], \tag{26}$$

where $\xi = (\mathbf{r}, \sigma, \tau)$, σ refers to the particle spin, and τ to the particle's isospin, see [10] and the references therein. In this definition, we introduced the Bogoliubov quasiparticle wave functions

$$\begin{pmatrix} u_k(\xi) \\ v_k(\xi) \end{pmatrix}, \tag{27}$$

and upon minimizing the energy, treating these new wave functions as variational parameters, one arrives at the SLDA equations [21], which are very closely related to the Hartree-

Fock Bogoliubov (HFB) equations [11], and which are given by

$$\begin{pmatrix} h_{\uparrow\uparrow}(\vec{r})-\mu & h_{\uparrow\downarrow}(\vec{r}) & 0 & \Delta(\vec{r}) \\ h_{\downarrow\uparrow}(\vec{r}) & h_{\downarrow\downarrow}(\vec{r})-\mu & -\Delta(\vec{r}) & 0 \\ 0 & -\Delta^*(\vec{r}) & -h^*_{\uparrow\uparrow}(\vec{r})+\mu & -h^*_{\uparrow\downarrow}(\vec{r}) \\ \Delta^*(\vec{r}) & 0 & -h^*_{\downarrow\uparrow}(\vec{r}) & -h^*_{\downarrow\downarrow}(\vec{r})+\mu \end{pmatrix} \begin{pmatrix} \mathrm{u}_{k\uparrow}(\vec{r}) \\ \mathrm{u}_{k\downarrow}(\vec{r}) \\ \mathrm{v}_{k\uparrow}(\vec{r}) \\ \mathrm{v}_{k\downarrow}(\vec{r}) \end{pmatrix} = E_k \begin{pmatrix} \mathrm{u}_{k\uparrow}(\vec{r}) \\ \mathrm{u}_{k\downarrow}(\vec{r}) \\ \mathrm{v}_{k\uparrow}(\vec{r}) \\ \mathrm{v}_{k\downarrow}(\vec{r}) \end{pmatrix}. \tag{28}$$

The SLDA/HFB equations are a generalization of the standard mean field Schrödinger equation defined above, due to the presence of the pairing field $\Delta(\vec{r})$ on the off-diagonal, which is calculated from the anomalous density, the superfluid order parameter, according to

$$\Delta_{n,p}(\vec{r}) = -g_{\mathrm{eff}}(\vec{r})\kappa_{n,p}(\vec{r}). \tag{29}$$

For the sake of completeness, we also include here the definition of all the various densities in terms of the quasiparticle wave functions,

$$n(\vec{r}) = \sum_{k,\sigma} \mathrm{v}^*_{k,\sigma}(\vec{r})\mathrm{v}_{k,\sigma}(\vec{r}), \tag{30a}$$

$$\kappa(\vec{r}) = \sum_{k} \mathrm{v}^*_{k\downarrow}(\vec{r})\mathrm{u}_{k\uparrow}(\vec{r}), \tag{30b}$$

$$\tau(\vec{r}) = \sum_{k,\sigma} \vec{\nabla}\mathrm{v}^*_{k,\sigma}(\vec{r}) \cdot \vec{\nabla}\mathrm{v}_{k,\sigma}(\vec{r}), \tag{30c}$$

$$\vec{s}(\vec{r}) = \sum_{k,\sigma,\sigma'} \vec{\sigma}_{\sigma\sigma'}\mathrm{v}^*_{k,\sigma}(\vec{r})\mathrm{v}_{k,\sigma'}(\vec{r}), \tag{30d}$$

$$\vec{J}(\vec{r}) = \frac{1}{2i}(\vec{\nabla}-\vec{\nabla}') \times \vec{s}(\vec{r},\vec{r}')\Big|_{\vec{r}=\vec{r}'}, \tag{30e}$$

$$\vec{j}(\vec{r}) = \frac{1}{2i}\sum_{k,\sigma}\left[\mathrm{v}_{k,\sigma}(\vec{r})\vec{\nabla}\mathrm{v}^*_{k,\sigma}(\vec{r}) - \mathrm{v}^*_{k,\sigma}(\vec{r})\vec{\nabla}\mathrm{v}_{k,\sigma}(\vec{r})\right]. \tag{30f}$$

A nonzero pairing field Δ will act to redistribute the single-particle occupation numbers $n_k = \int d\xi |v_k(\xi)|^2$, transferring some weight from the v-components to the u-components (and vice versa), which is how one encodes the effects of the pairing interaction into a mean field theory expressed in terms of single-particle wave functions. The precise profile and dynamics of the occupation number distribution during various physical processes of interest will be one of the central focuses of this thesis. We note that it is always possible to instantaneously transform to a basis in which the many-body wave function takes on the BCS form of Eq. (20); however, under dynamics the many-body wave function will note stay

in this BCS form, so the Bogoliubov vacuum ansatz of Eq. (24) must be used instead, see the discussion in Secs. VII and VIII.

TDSLDA is the first time-dependent mean field formalism in the literature which properly handles pairing correlations, accounting for self-consistency, the regularization and renormalization of the known divergence of the anomalous density matrix at short distances [22, 23], and which does not rely on simplifying assumptions such as that the many-body wave function always assumes the BCS form. As we will show in this thesis, the combination of a well-constructed mean field and the proper treatment of pairing correlations leads TDSLDA to be the leading microscopic approach for the study of nuclear fission dynamics, and also to be one of the leading approaches for simulating the dynamics of cold atom systems. TDSLDA offers several predictions which should in principle be measurable in experiments on nuclear and cold atom systems, and also it offers fundamental insights into the quantum mechanics of strongly interacting many-fermion systems.

IV. NECK RUPTURE AND SCISSION NEUTRONS IN NUCLEAR FISSION

In this section, we review the results presented in the paper "Neck Rupture and Scission Neutrons in Nuclear Fission" by I. Abdurrahman, M. Kafker, A. Bulgac, and I. Stetcu, Phys. Rev. Lett. **132**, 242501 (2024) [6].

A. Abstract

During the process of nuclear fission, the nucleus becomes increasingly deformed, until eventually splitting in two. Immediately prior to the splitting, termed scission, a neck is formed between the two emerging fission fragments (FFs). It is widely believed that the rupture dynamics of the neck are quite violent, although there is no unambiguous experimental evidence that this is in fact the case. From a theoretical perspective, the saddle-to-scission and neck rupture stages of nuclear fission are technically challenging to treat because they are both highly nonequilibrium processes in a strongly interacting quantum many-body system. Here, we use the time-dependent superfluid local density approximation (TDSLDA), an extension of time-dependent density functional theory to superfluid systems, to characterize the scission mechanism from a fully microscopic perspective for the first time in the literature. In addition, we document the spectrum and spatial distribution of scission neutrons (SNs), as well as some upper bounds on the emission of charged particles. We find that the emitted scission neutrons have a distinctive angular distribution, with neutrons being emitted in approximately equal numbers along the fission axis ahead of each fragment and in a ring-shaped cloud around the fission axis centered on the location where the neck ruptured. The SNs are found to carry an average energy around 3 ± 0.5 MeV for the fission of ^{236}U, ^{240}Pu and ^{252}Cf, with a surprisingly high maximum energy of 16 - 18 MeV. Based on the emitted number of particles, we estimate a (conservative) lower bound that $9 - 14$ % of the total number of neutrons emitted during the fission process are produced at scission.

B. Introduction

Nuclear fission was first discovered in an experiment in 1939 performed by Hahn and Strassmann [24]. Later that same year the primary mechanism was explained by Meitner and Frisch [25], who also gave the process its name. Nuclear fission is a highly complex

dynamical behavior of a strongly interacting quantum many-body system, with different stages of the process taking place over dramatically different timescales spanning many orders of magnitude. Indeed, when one considers the total duration of the fission process, from the absorption of the incident neutron and formation of the compound nucleus, to the separation of the nucleus into fragments, the subsequent emission of prompt neutrons and γ rays, and finally the further β decays of the fragments until they have attained their equilibrium state, the total elapsed time can be on the order of billions of years [26]! This should be contrasted with the another relevant timescale for the fission problem, the time for a nucleon to cross the nucleus, which is $\mathcal{O}(10^{-22})$ seconds. We begin by describing the various stages of the fission process in more detail, as this will provide the context for our new results on the neck rupture and release of the scission neutrons.

In the case of neutron-induced fission, the process begins with the absorption of a low-energy incident neutron [24] by a heavy target nucleus and the subsequent formation of the compound nucleus. This compound system [27] evolves through a variety of distinct stages before ultimately splitting in two. Firstly, the nucleus progressively deforms in a quasi-equilibrium manner until reaching the outer saddle point, which is the point where balance between the restoring force from the surface tension and the repulsive Coulomb force shifts, and it becomes energetically favorable to continue deforming until the nucleus fully separates. The time required for this process is $\approx 10^{-14}$ seconds [26], and during this process, the nuclear shape evolution is rather complex. Initially, the nucleus is prolate with axial symmetry, and then it evolves into a region where it is triaxial, before finally returning to an axially symmetric elongated configuration with reflection asymmetry near the outer fission barrier [28]. Starting from the outer fission barrier, the second stage of dynamics sets in, which is highly non-equilibrium in character, namely the descent from the outer saddle to the scission configuration [29–31], which lasts $\approx 5 \times 10^{-21}$ seconds [26] and during which the primordial FF properties are established. The third stage of fission dynamics is the process of scission itself, also called the neck rupture, which is by far the fastest stage of the dynamics, as we will show below, lasting only $\approx 10^{-22}$ seconds, and during which the compound nucleus rapidly separates into two distinct fission fragments. It is at this stage that we argue a small number of neutrons will also be released, which is the subject of this study; these are the so-called scission neutrons. Following scission, a fourth stage begins in which the FFs are accelerated by the Coulomb interaction, which takes about $\mathcal{O}(10^{-18})$

seconds to complete, by which time the shapes of the FFs, which emerge deformed from scission, relax to their equilibrium values. It is an interesting fact that whereas the initial compound nucleus in fission is a relatively cold system with a very small spin, the FFs emerge from scission very hot and with relatively large spins, which was convincingly demonstrated using TDSLDA simulations [30, 32]. The excitation energy of the fission fragments is then released, first through the evaporation of "prompt" neutrons (isotropically in the rest frame of each fragment), which takes $\mathcal{O}(10^{-14})$ seconds, and subsequently by the emission of γ rays, which can last up until $\mathcal{O}(10^{-3})$ seconds. Following the prompt emission, a much slower process of β decays occurs. It is sometimes possible to even have γ emission following these β decays.

All the stages of the fission process described above can be understood as quasiequilibrium processes which are relatively slow, with the exception of the saddle to scission evolution and the neck rupture, which are the stages of the fission process we focus on with TDSLDA. In most studies of fission prior to the introduction of TDSLDA in 2016 [29], fission dynamics beyond the outer saddle point were described in terms of the nuclear potential energy surface (PES), which is determined by calculating the nuclear ground state energy in a confining potential of a given deformation, and then repeating this process over a large set of nuclear deformations. In other words, the dynamics were determined entirely by the evolution of the nuclear shape alone [11, 26, 33, 34], which is not compatible with recent microscopic studies that demonstrate the crucial role played by dissipation in converting the potential energy of the compound nucleus into internal excitation energy during the descent from saddle to scission [29–31, 35]. Getting such approaches to agree with experiment generally requires adjusting many parameters [36]. It should be noted, however, that many different approaches are able to calculate FF mass and charge distributions [36–41], which TDSLDA currently cannot do, even though these approaches rely on mutually contradictory physics assumptions. We interpret this to mean that the fragment mass and charge distributions are not in fact very sensitive to the details of fission dynamics.

We now turn our attention in detail to saddle-to-scission and neck rupture dynamics. Near the top of the outer saddle, the nuclear density begins to form a "wrinkle," which is the precursor to the neck which will eventually form between the two FFs. This wrinkle forms early in the saddle to scission evolution, and does not move as the nucleus evolves towards scission, as we will demonstrate below, but one can argue that this is expected, as a significant

change in its position would require a large amount of energy that would not be available from fluctuations [42–46]. Starting from the outer saddle the nucleus begins its descent towards scission, which is a relatively slow and dissipative process [29–31], during which the nucleus becomes increasingly elongated and the neck increasingly pronounced. It was first demonstrated unambiguously by TDSLDA simulations that during this stage, due to dissipative effects produced by the pairing interaction, the nucleus has a very small collective velocity [29–31] and the internal excitation energy of the nucleus gradually increases. The neck progressively shrinks during the elongation until it hits a critical diameter of about 3 fm, whereupon an instability sets in and the the neck violently and very quickly ruptures, in precisely the location the initial wrinkle formed much earlier at the top of the outer saddle. Brosa *et al.* [47] argued that scission was the stage of fission where the fragment properties, including the total kinetic energy (TKE), were defined. The Brosa model advocated by these authors treats the nucleus as a very viscous fluid, where the neck is taken to be very long, and the neck ruptures at a random point along this elongated neck, thereby producing FF distributions. This approach is widely invoked in phenomenology used today [48–55], even though as we will show it does not have any basis in microscopic theoretical calculations, and furthermore, the claim that the assumptions used in this approach are supported by experimental data is not necessarily the only possible interpretation. It is also worth noting that the assumptions in the Brosa random neck rupture model contradict the assumptions in other popular approaches for determining FF properties, such the scission-point model of Wilkins *et al.* [56], where the FF formation is based on statistical equilibrium [57, 58], and also the Brownian motion or Langevin models [36, 39, 59–61]. We will also demonstrate below that the violent process of the neck rupture leaves behind "debris," in the form of scission neutrons, which were conjectured to exist as early as 1939 Bohr and Wheeler [62], and which have been a contentious topic in the literature ever since and lasting to this day. (In the supplemental material accompanying this paper [6], we include a history of discussions in the literature of scission neutrons, and the various claims of their existence and properties, or their nonexistence, over the years.) Potentially other heavier fragments, usually referred to as ternary fission products [63–65], can be created as well, but as we will argue below, it is much more difficult to see these other kinds of emission in the kinds of TDSLDA simulations we consider for in this study.

Run #	Nucleus	Q_{20} [b]	Q_{30} [b$^{3/2}$]	β_2	β_3
1	^{236}U	184.33	19.66	1.88	0.86
2	^{236}U	159.64	17.80	1.63	0.77
3	^{236}U	135.25	12.74	1.38	0.55
1	^{240}Pu	157.20	20.18	1.56	0.85
2	^{240}Pu	153.11	18.34	1.52	0.77
3	^{240}Pu	140.08	10.6	1.39	0.45
4	^{240}Pu	141.85	8.56	1.40	0.36
5	^{240}Pu	144.71	6.63	1.43	0.28
6	^{240}Pu	145.64	6.63	1.44	0.28
1	^{252}Cf	240.80	36.53	2.20	1.39
2	^{252}Cf	227.19	32.50	2.07	1.24
3	^{252}Cf	199.17	23.52	1.82	0.90
4	^{252}Cf	168.29	13.44	1.54	0.51

TABLE I. The initial quadrupole and octupole deformations used for all the simulations in this study.

C. Results

We started our TDSLDA simulations by placing the compound nucleus near the top of the outer fission barrier in a very large simulation volume, which we employed so as to allow the emitted particles enough space and time to decouple from the FFs after the neck rupture. We simulated the nuclear fission reactions ^{235}U(n$_{th}$,f), ^{239}Pu(n$_{th}$,f), and ^{252}Cf(sf), using the nuclear energy density functional (NEDF) SeaLL1 [12] in simulation volumes $48^2 \times 120$ and $48^2 \times 100$ fm^3, with a lattice constant of 1 fm, using the LISE TDSLDA code [21]. The SeaLL1 functional has only 8 parameters, each related to specific nuclear properties which have been known for decades, and it achieves very high accuracy while simultaneously using the smallest number of phenomenological parameters in any accurate nuclear EDF presented in the literature to date [12, 66]. The initial deformations we used for this study are listed in Table I, and were also chosen along the rim of the outer fission barrier. (For a TDSLDA study of how the FF properties depend on the choice of initial deformation, see [29–31].) It is

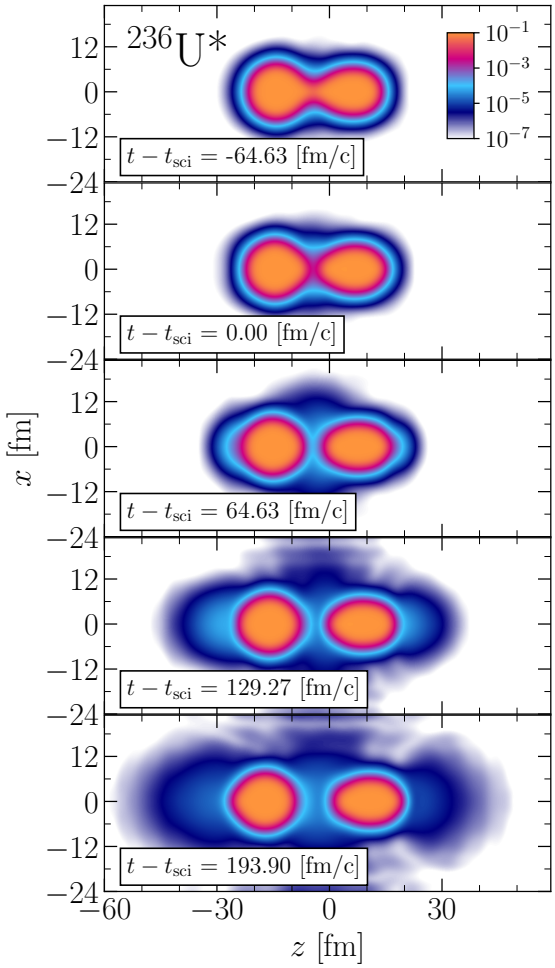

FIG. 1. Time series of neutron number density, in units of fm^{-3}, presented in a log scale around the moment of scission, revealing a low amplitude neutron cloud emitted with a distinctive angular distribution.

worth mentioning that simulating nuclear fission in the box of size $48^2 \times 120$ fm^3 considered in this study required immense computational resources, simultaneously using all 27,648 GPUs on the Summit supercomputer for 15 hours straight for a single simulation run, making each one a plausible candidate for the largest numerical simulation ever performed to date at that time (2022). Despite the immense computational resources we employed, we were still only able to follow the emitted SNs for a short period of time before they were reflected back at the boundary of the box, producing interference patterns, see Fig. 1. As the simulation box is elongated along the fission axis, and thinner perpendicular to the fission axis, the scission neutrons emitted in this transverse direction (about half of the total number of SNs) reflect

at the boundary earlier than the SNs emitted along the, and this has probably affected their properties slightly, although we argue below that the effect is minor.

In Fig. 2, we show the density in the neck, for both neutrons and protons, which is first projected onto the fission axis by integrating over the transverse coordinates

$$n_{\mathrm{neck},\tau}(t) = \int dxdy\, n_\tau(x, y, z_{\mathrm{neck}}, t), \quad \tau = n,\, p, \tag{31}$$

where the z_{neck} is the position along the fission (z) axis where the neck has the smallest radius. We see that during saddle to scission evolution, the neck decreases in diameter rather slowly until a critical thickness is reached, whereupon it becomes unstable and undergoes a rapid decay which is well characterized by an exponential fit, where the characteristic timescale does not appear to depend on the initial deformation of the nucleus (at least for the asymmetric fission cases considered here). Note that the invariance of this characteristic timescale is in marked contrast to the time to evolve from saddle to scission, which depending on the initial deformation (Q_{20}, Q_{30}) typically varies from 1,000 to 3,000 fm/c.

These fully microscopic quantum many-body TDSLDA simulations of the scission process reveal several new aspects of the phenomenon. The first new aspect of the scission process is that the location of the neck is determined early, near the outer saddle point, with the formation of the initial "wrinkle" in the density, and this initial wrinkle does not move once it has begun forming. Contrary to the popular Brosa model [47], the neck rupture location is not random according to microscopic calculations. Once the neck reaches a critical diameter of about 3 fm, an instability sets in, where the nuclear surface tension for the elongated compound can no longer counteract the strong electrostatic repulsion between the two proto-fragments, and so the system violently splits in two. One relevant aspect of this story is that as the nucleus heats up, as TDSLDA demonstrates that it does during the descent from saddle to scission, the nuclear surface tension decreases. It goes without saying that the geometry of the nucleus changes dramatically during the neck rupture: beforehand, the nucleus is a single compact shape with a neck region characterized by a negative Gaussian curvature, whereas after the nucleus has separated into two fragments, each with surfaces with predominantly positive Gaussian curvature.

The second novel aspect of the scission process revealed in this study is that the proton neck ruptures before the neutron neck, see Fig. 2, such that for about 50-100 fm/c, the neck is entirely composed of neutron matter prior to fully rupturing. This situation is reminiscent

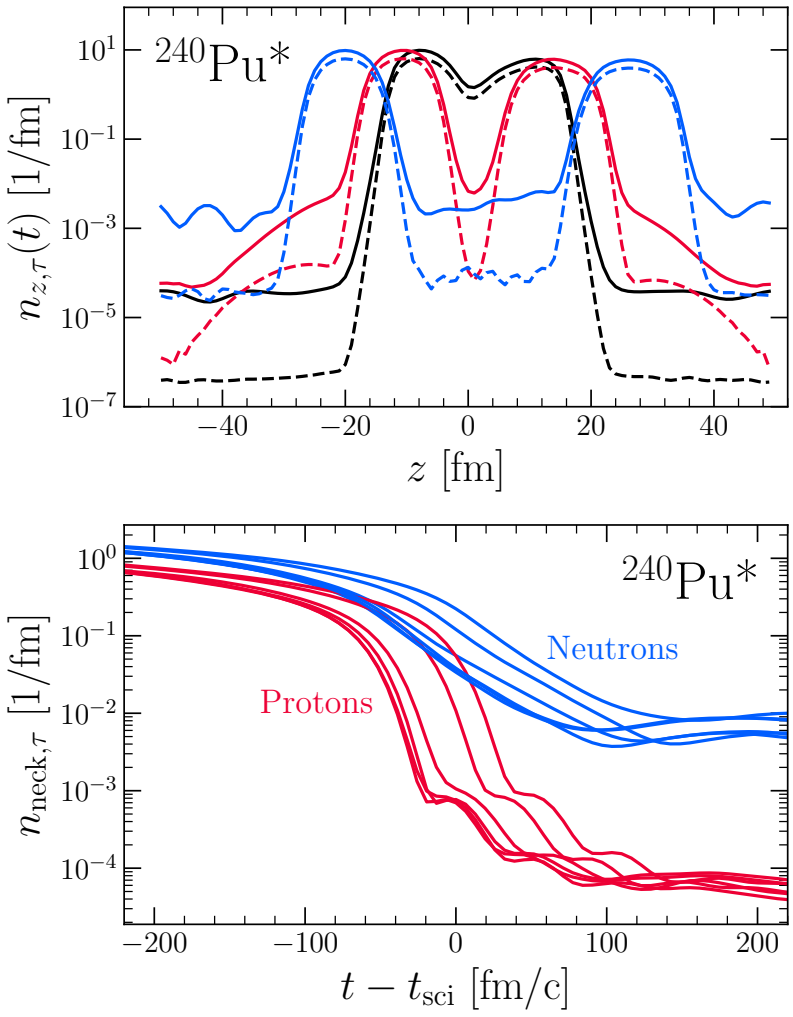

FIG. 2. In the top panel we display the neutron and proton densities projected onto the fission axis using Eq. (31) in a logarithmic scale at several times: before scission at -258.53 fm/c (black lines), when the neck is barely formed; after scission at 129.27 fm/c (red lines); and after the FFs separated respectively at 517.06 fm/c (blue lines). Neutrons/protons are represented via solid/dashed lines respectively. We clearly observe the formation of the "wrinkle" at early times which does not move significantly during saddle-to-scission evolution. In the bottom panel, we look at the time dependence of this "projected" number density evaluated at the neck location, presented again in a logarithmic scale, for a variety of initial deformations, each represented by a different curve. The neck rupture dynamics are clearly exponential in character once the instability sets in, and we find that the characteristic timescale of the exponential decay in the density is $n_{\mathrm{neck},\tau}(t) \sim \exp(-t/\tau)$, with $\tau \approx 35.0 \pm 2.2$ fm/c for neutrons and 15.3 ± 0.3 fm/c for protons.

of the neutron skin in heavy nuclei, where the RMS radius of the neutron matter distribution in a heavy nucleus exceeds that of the proton distribution, such that near the nuclear surface, the neutron density is significantly greater than the proton density. We note also that after the rapid exponential decay of the neck, the neutron and proton densities almost immediately attain equilibrium values.

The third novel aspect is that the scission process is unarguably the fastest stage of fission dynamics, beginning from the formation of the compound nucleus and extending all the way until the emission of the fission products has concluded. If we consider the timescales for the rupture of the neck, 15 fm/c and 35 fm/c for proton and neutron necks respectively, these are far faster than even than the time it takes a nucleon traveling at the Fermi velocity to travel the length of the compound at the scission configuration, which is about 160 fm/c, and which we can consider the minimum timescale over which any sort of thermal equilibrium between the two proto-fragments could possibly be established.

The fourth new feature of the scission process is that the neck dynamics have a somewhat universal character, at least for the case of asymmetric fission, in the sense that regardless of the time it takes the compound to evolve from the outer saddle to the scission configuration, and regardless of the initial deformation, the rupture dynamics always occur with essentially the same timescale, see Fig. 2. Furthermore, as was mentioned above, the proton neck also always ruptures first, due to the presence of a well-defined neutron skin. The fact that the proton and neutron neck ruptures are essentially the same for all asymmetric fission trajectories makes them dissimilar to other aspects of the fission process, such as the time to define the various properties of the fragments, which vary based on the initial conditions [30, 31].

The final new feature of the scission process we report here is that the mechanism underlying scission is completely at odds with previous models, including the Brosa random neck rupture model and the scission-point models. TDSLDA is the only theoretical treatment of the scission problem which does not rely on uncheck assumptions or uncontrolled approximations, and which produces results which on average are in agreement with experimental data [29–31, 67].

We next turn to the scission neutrons clearly emitted during the neck rupture process, see Fig. 1. We first note to the reader that we did not seek out the scission neutrons, nor did we have to perturb the compound nucleus in any way to observe the SNs; rather, we found that

in all TDSLDA simulations we have performed, which now number in the several hundreds, a low density neutron cloud is present, very similar to the one shown in Fig. 1. We now offer an explanation for why the SNs are released. The neck rupture, as we have already argued, is a highly non-equilibrium process, and is followed by a very rapid "resealing" of the "break" created in the nuclear surface by the rupture. Unlike gas escaping a punctured balloon, which would proceed rapidly and with not too much obstruction, the presence of the neutron skin and the strong surface tension causes the nuclear matter to behave like a fluid. Surface tension quickly closes the "wound" in the nuclear surface, but a small fraction of the matter is nevertheless allowed to escape like a gas, with no droplet formation. (TDSLDA only includes two-particle collisions, and so the potential condensation of the emitted gas into light charged nuclei cannot be treated in this framework. Note also that we consider this condensation process to be separate from the case of the ternary fission of a preformed fragment.) The nuclear matter which is not prevented from escaping by the nuclear surface "erupts" in an azimuthally symmetric cloud surrounding the location where the neck rupture occurred. After a short delay, see Fig. 1, a second set of neutron clouds appear ahead of each fragment. The delay is consistent with the time it takes for the nucleons to propagate from the neck through each fragment and out the other side, and so it seems plausible that the explanation for these "longitudinal" SNs is the "catapult" mechanism (which is more properly described as a slingshot mechanism), which was proposed by Mädler [68] in 1984, and which states that it is the rapid reabsorption of the neck "stumps" into the fission fragments which pushes matter through the FFs and out the other side. We reiterate that the distinctive shape of the scission neutron clouds, with a cloud in front of each fragment and a ring shape cloud surrounding the fission axis, is seen in all TDSLDA fission simulations performed thus far.

It is reasonable to ask whether the FFs will ever catch up with the scission neutrons, seeing as we can only follow the emitted particles for a very short time before they reach the boundary of the box. Recalling that the total kinetic energy (TKE) is about 171-186 MeV, after the FFs are fully accelerated by the Coulomb force, the light and heavy FFs will have an average kinetic energy per particle of approximately 1 MeV and 0.5 MeV respectively. If we compare this to the average kinetic energy per particle for the scission neutrons, which are presented in Fig. 3, we see the average values of 3.51 ± 0.25 MeV, 3.42 ± 0.27 MeV, and 2.67 ± 0.24 MeV for ^{236}U, ^{240}Pu, and ^{252}Cf respectively, and so we conclude the the

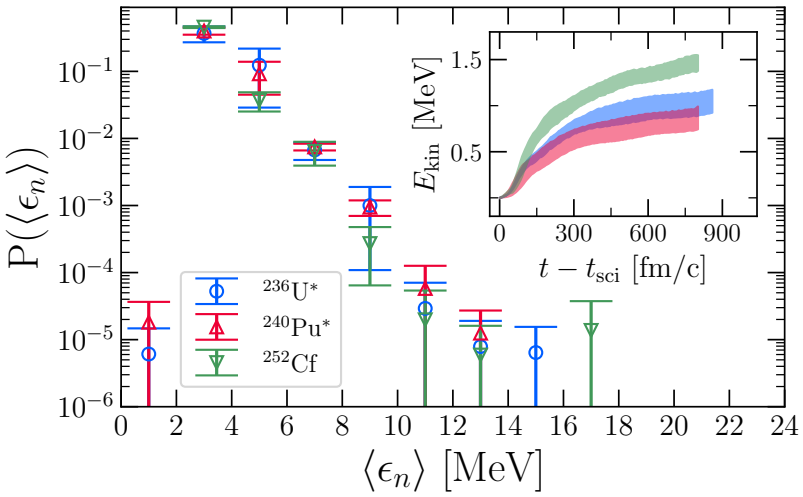

FIG. 3. The estimated distribution of the kinetic energy per particle for the emitted scission neutrons. The uncertainties correspond to the standard deviation taken over the different trajectories included in this study, see Table I. The distributions are normalized to the total number of scission neutrons, such that $\sum \mathrm{P}(\langle\epsilon_n\rangle) \times \frac{\Delta E}{\mathrm{MeV}} = N_{\mathrm{sci}}$, with $\Delta E = 2$ MeV. The inset shows the kinetic energy for the entire SN cloud as a function of time, where the shaded regions refer to the mean ± standard deviation over the trajectories considered in this study.

SNs are emitted with velocities that exceed the final velocity of the fission fragments, so the neutrons will escape to infinity, which means that in principle they should be accessible to experiment. It was noted by R. Capote [69] that our results are consistent with high-energy neutrons observed via dosimetry measurements [70], and thus there is very probably the need to include SNs in the analysis of prompt neutron spectra [71]. Finally, we also note that we estimated the interaction energy of the SNs using the neutron matter equation of state [12],

$$E_n^{\mathrm{int}} = \int dV [a_n n_n^{5/3} + b_n n_n^2 + c_n n_n^{7/3}] \ll E_n^{\mathrm{kin}}, \tag{32}$$

and found them to be essentially noninteracting, as the interaction energy comprises less than 1% of their kinetic energy.

The next question which is of crucial importance is to determine how many neutrons are emitted, which is shown in Fig. 4. The total number of emitted neutrons is about 0.30 ± 0.05, 0.26 ± 0.05, and 0.55 ± 0.02 per fission event for ^{236}U, ^{240}Pu, and ^{252}Cf respectively, which is a considerable portion (roughly $9 - 14$ %) of the total emitted prompt neutrons, see

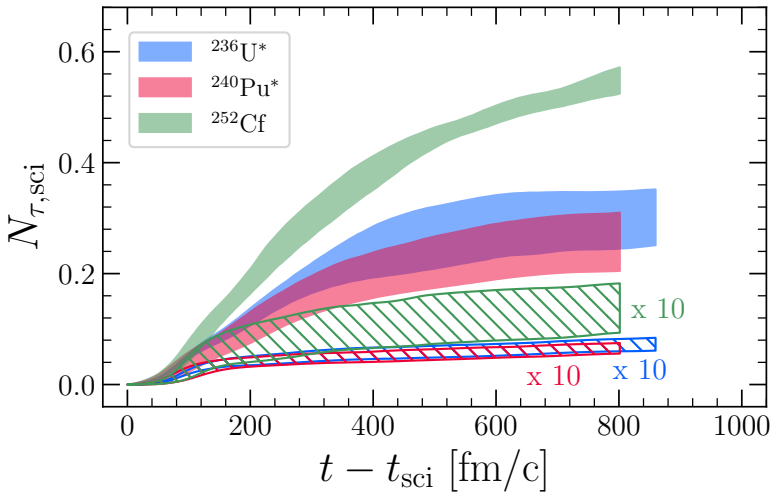

FIG. 4. Total number of emitted neutrons and protons as a function of time. The neutrons are represented by the solid regions and the protons, which are enhanced by a factor of 10 to show the trend on the same scale as the neutrons, are shown in dashed regions. Again, the interpretation of the shaded region refers to the mean plus or minus one standard deviation over the trajectories we considered for this study.

Refs. [63, 65]. Seeing as the curves in Fig. 4, particularly for the case of ^{252}Cf, have not fully flattened yet, it is likely that the numbers reported here are an underestimate of the true signal. As a point of comparison, in several studies, Carjan *et al.* [72–76] estimated an upper bound of 25 – 50 % of prompt fission neutrons are emitted during scission. We also see from Fig. 4 that protons are emitted at scission as well, but the number is smaller by a factor of about 50-100 relative to the number of emitted neutrons. We plot the proton and neutron emission side by side in Fig. 5, which shows that proton emission is clearly much less than neutron emission, and primarily along the fission axis. Finally, we note that the number of emitted particles in the ring-shaped and longitudinal clouds is approximately equal, as we show in Fig. 6.

It is also reasonable to ask to what extent the boundaries affect the number and properties of the emitted neutrons. To assess this question, we calculated the number of emitted neutrons using several distinct approaches, and we find the variation amongst these approaches is minor, at the level of 10% or so. To calculate the number of emitted neutrons, we defined a surface surrounding the compound/fragments, and we calculated the number

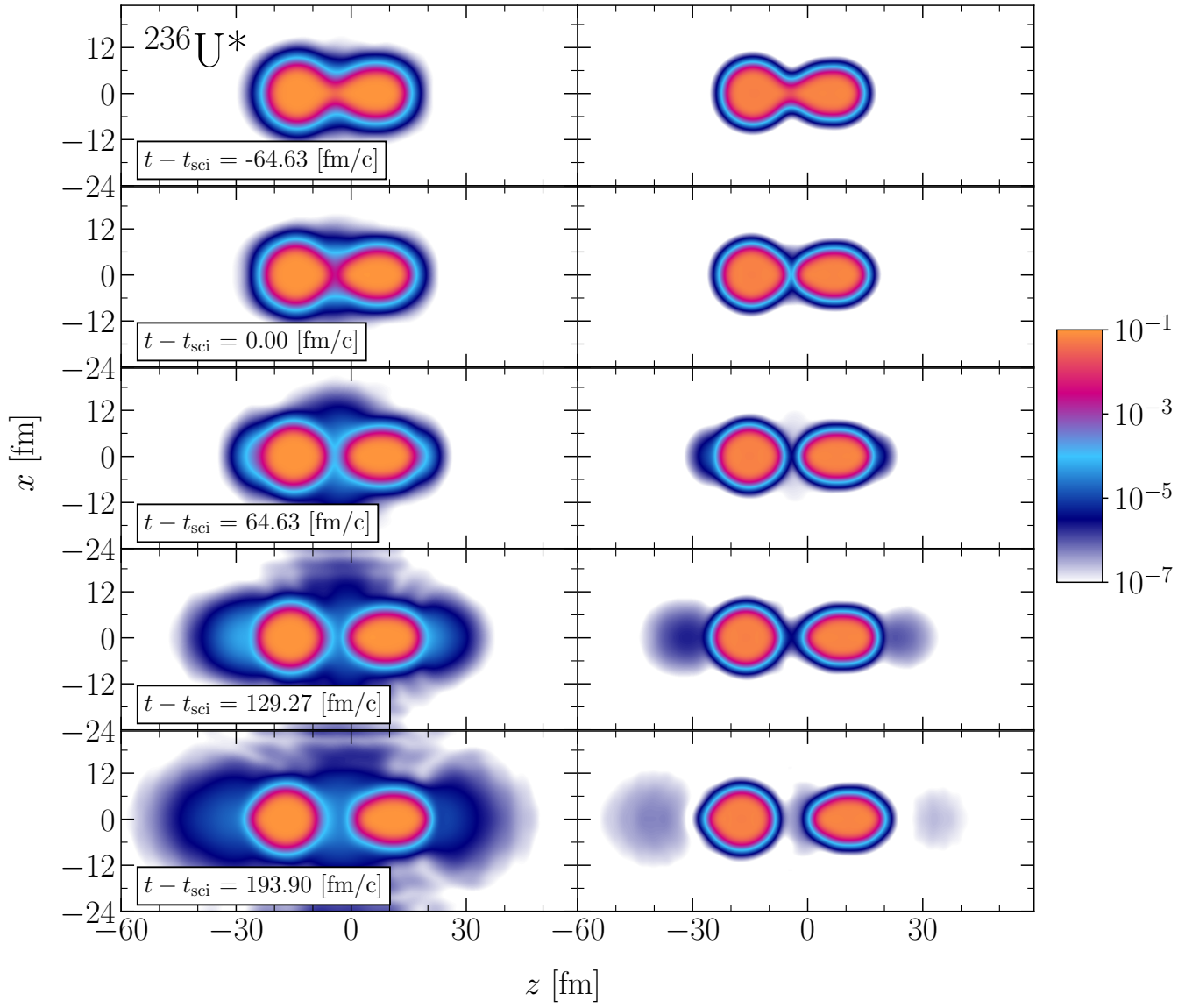

FIG. 5. Spatial profiles of emitted scission neutrons and protons, presented in a logarithmic scale.

of particles outside that surface, see Fig. 7. We considered two types of boundary surfaces, a stadium shaped surface and two bounding spherical surfaces, which are characterized by a single parameter, which is the radius of the sphere. Furthermore, we calculated the number of emitted neutrons by integrating the neutron number density outside the bounding region, and also by performing a flux integral of the neutron current density over the bounding surface. (These two results should be equivalent according to the continuity equation.) In all cases, we find close agreement between the methods, as Fig. 7 clearly shows. On the other hand, we note that interference at the boundaries of the box does affect the current density

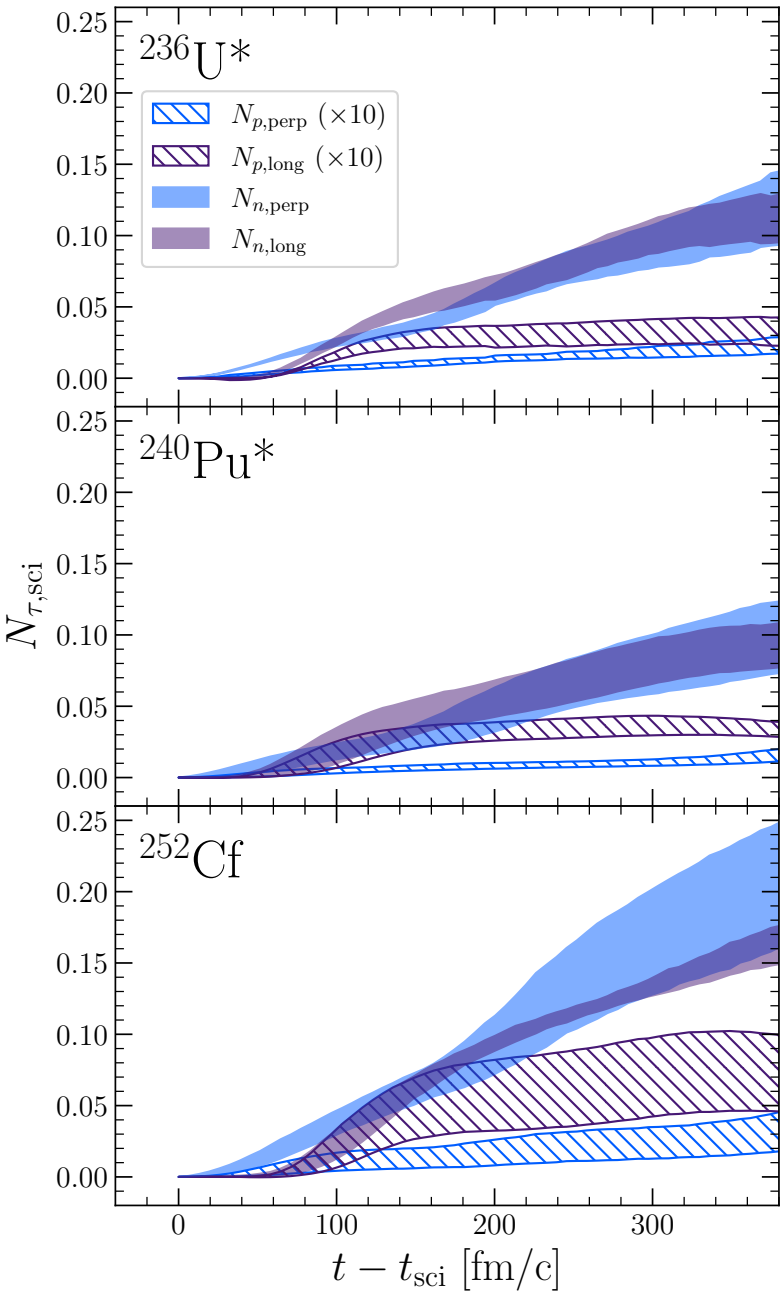

FIG. 6. Time series of nucleon emission split into transverse ring-shaped cloud and longitudinal clouds, showing approximately equal emission in each case.

there, which is an aspect that will have to be addressed in future work, as it is likely that a joint energy-angle distribution of the SNs will be required to disentangle scission neutrons from evaporated prompt neutrons in future experiments.

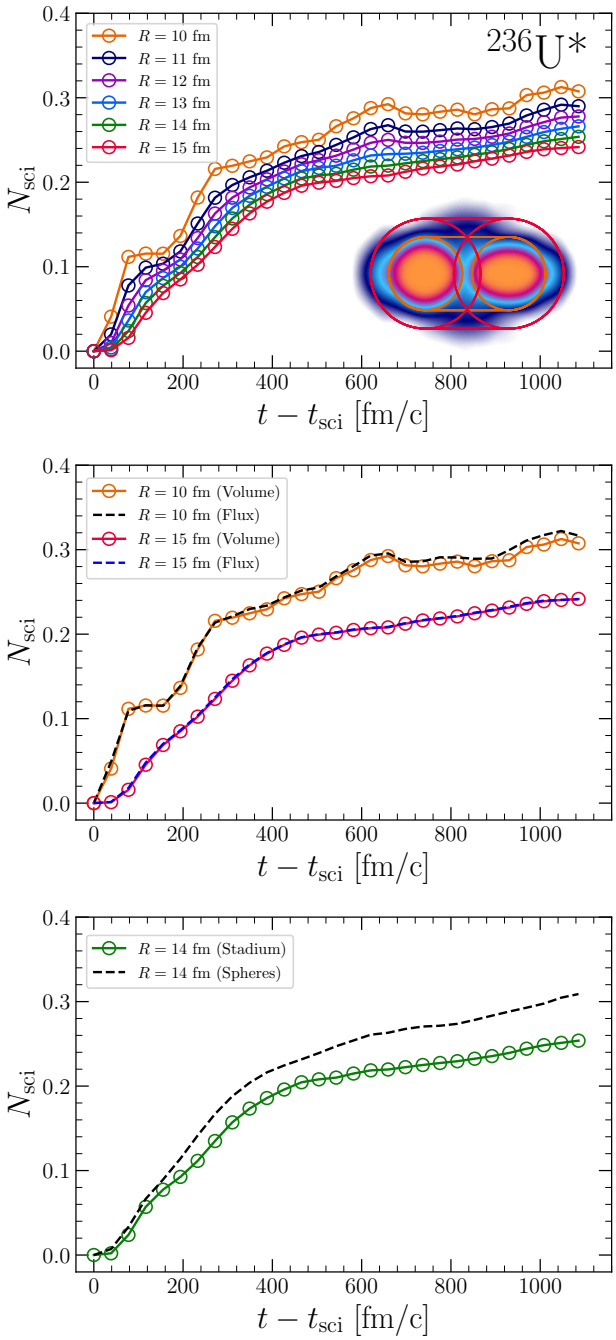

FIG. 7. Comparison of various methods for counting the number of scission neutrons. In the top panel, we show the number of emitted neutrons as a function of the radius of the bounding surface. In the middle panel, we compare the flux integration and volume integration methods for calculating the emitted particle number. In the bottom panel, we compare integration using the spherical bounding surface and the stadium bounding surface. The spheres include emitted neutrons which are found between the fragments, and so the number counted using this surface exceeds that of the stadium.

D. Conclusions

In summary, we implemented TDSLDA simulations of the scission process in very large simulation volumes, and in so doing presented several novel aspects of scission, which is the fastest and most non-equilibrium stage of nuclear fission dynamics. We found that within TDSLDA, the neck rupture is not a random process, as is advocated in various phenomenological approaches. We also find that the dynamics of the rupture process are very similar, regardless of the nuclear system considered or the initial deformation of the compound at the outer saddle point, for asymmetric fission calculations. The "universality" also applies to the emission of SNs, which always appear in a distinctive three-cloud profile, with one appearing in front of each fragment and one in a ring shape around the neck rupture location, with approximately equal numbers emitted along the axis and perpendicular to it. The features of the neck rupture presented here may serve as valuable input to a variety of (semi)phenomenological approaches used to study FF properties [49–52].

The possibility that there might be scission neutrons was first proposed by Bohr and Wheeler [62] in 1939, and as such is almost as old as the study of nuclear fission itself. The existence of SNs has been a highly contentious topic for decades [72–96], see also *Historical Note* in Ref. [65], and their experimental confirmation is still an open question. We note that earlier studies using simplified models [72, 75, 76] share some features with our neutron properties, these studies do not show emission perpendicular to the fission axis, which for us constitutes half the emitted SNs. We also stress that a small fraction of our emitted SNs carry a surprisingly high amount of kinetic energy, upwards of 18 MeV, as shown in Fig. 3, which is similar to previous observations in the literature [69, 71]. Finally, we found that along with the emitted neutrons, a very small fraction of protons are emitted at scission as well, primarily along the fission axis, and the number of these protons should suggest a theoretical estimate for the emission of α-particles and other charged nuclei, at least for axially symmetric fission in the absence of fluctuations, like we consider in this study.

V. INDUCED FISSION OF ODD-MASS AND ODD-ODD NUCLEI WITHIN TIME-DEPENDENT DENSITY FUNCTIONAL THEORY

In this section, we review the results presented in the manuscript "Time-Dependent Density Functional Theory Description of ^{238}U(n,f), ^{240,242}Pu(n,f), and ^{237}Np(n,f) Reactions" by A. Bulgac, I. Abdurrahman, M. Kafker, and I. Stetcu, Phys. Rev. Lett. **135**, 062501 (2025) [2].

A. Abstract

In nuclei where the number of protons and/or neutrons is odd, the spin density is nonzero, which produces a pseudomagnetic field that favors the splitting of Cooper pairs of nucleons. Such pseudomagnetic fields will always contribute to the nuclear mean field in the case of nuclear dynamics, even in the case where the neutron number N and the proton number Z are both even; however, the effects on Cooper pairs are significantly enhanced for the dynamical evolution of odd nuclei when compared to even-even nuclei. In this paper, we presented for the first time a microscopic study of the induced fission of several odd-mass or odd-odd compound nuclei in time-dependent density functional theory (TDDFT) extended to include pairing correlations, where we did not make any simplifying assumptions and where we used controlled numerical approximations. Specifically, we considered a very large number of initial conditions for the induced fission of the odd-neutron compound nuclei ^{239}U, ^{241,243}Pu, and the odd-proton, odd-neutron compound nucleus ^{238}Np. Because of the nonzero pseudomagnetic field created by the unpaired odd nucleon, the time-reversal symmetry of the nucleus is spontaneously broken, which is an aspect of the simulation of odd systems which has been very often neglected in the past, even in the most advanced treatments. We find that the properties of the fission fragments (FFs) prior to neutron and gamma emission—aspects of the fission process which we do not include in TDDFT calculations—are quite similar to the properties of FFs from neighboring even-even nuclei, although with a noticeably wider standard deviation in almost all cases. We also find that the the saddle-to-scission evolution time can be significantly longer in the case of odd-mass or odd-odd nuclei when compared with neighboring even-even nuclei, which can be explained by the higher level density of odd systems at lower excitation energy. As a result of this

higher level density, these systems are easier to excite, and provided the excitation energy of the compound is not too high, the potential energy surface (PES) is much rougher than in the case of even-even systems or odd systems with higher excitation energy, and thus the nuclear shape evolution in this case will become "convoluted" or "confused" as it evolves from the top of the outer fission barrier to the scission configuration. Finally, we test the validity of the Pauli blocking approximation, which is often invoked in the literature and which is expected to inhibit fission due to the fact that the blocked single-particle orbital cannot participate in a Cooper pair and thus pairing is "inhibited." We find that, surprisingly, the Pauli blocking approximation is strongly violated during fission dynamics.

B. Introduction

Odd-mass and odd-odd nuclei have a much higher level density than even-even nuclei at the same excitation energy. This is perhaps most easily seen in the case of the pure pairing interaction in a degenerate shell where the single-particle states are labeled by a single quantum number m, which might be the projection of the angular momentum along one of the system axes, see Sec. III C. For a system with just two particles, the ground state is a Cooper pair

$$\sum_{m>0} |m,-m\rangle = \sum_{m>0} a_m^\dagger a_{-m}^\dagger |0\rangle, \tag{33}$$

and there is no degeneracy. However, if we have three particles in the shell instead, the ground state becomes

$$\left(\sum_{m>0,m\neq i} a_m^\dagger a_{-m}^\dagger\right) a_i^\dagger |0\rangle. \tag{34}$$

We call i the "blocked" state, and the ground state of the odd system is degenerate because one can choose to block any state i in the shell. Similar arguments hold for the case when more particles are present in the shell.

The higher level density of odd systems at the same excitation energy applies not only near the ground state, but everywhere along the path the nucleus takes on the potential energy surface, all the way from the ground state to scission, including when the nucleus is navigating the fission barrier. The fact that the nuclear PESs are close together means there is an enhanced probability that time-reversed pairs of nucleons will jump from one surface

to another, as a result of the pairing interaction. The possibility to jump between potential energy surfaces has been known to be relevant in chemistry for a long time [31, 97, 98]. In this study we consider induced fission with low energy neutrons [99, 100], which produces compound nuclei near the top of the outer fission barrier which are "cold," according A. Bohr [63], and in which there are a large number of accessible fission channels for odd-mass or odd-odd systems. The theoretical treatment of odd-mass and odd-odd systems is more technical than that of even-even systems, as one must include the effects of a variety of densities in the density functional which otherwise vanish for static calculations of even-even nuclei, or else one must rely on certain simplifications or approximations which are not well supported by strong theoretical arguments. As a result, there are far fewer mean field theory or DFT studies of odd nuclei in the literature when compared with the number of studies of even-even nuclei. That there are significant differences in the fission behavior of odd and even systems has been known since the Manhattan Project, as ^{240}Pu contamination of ^{239}Pu samples led to predetonation of nuclear explosions due the significantly higher spontaneous fission rate of the even-even isotope, and so to circumvent this issue, the implosion mechanism was implemented in the design of fission weapons. However, this is just one example, and more generally the systematics of spontaneous fission half-lives of even-even (E-E) versus odd-even (O-E), even-odd (E-O), and odd-odd (O-O) compound nuclei are commonly presented in discussions of fission [42, 62, 63, 65]. As was mentioned above, the spontaneous fission half-lives of E-E nuclei are several orders of magnitude smaller than those of E-O, O-E, or O-O nuclei, despite the fact that the fission barriers are very similar [63]. In this chapter of the thesis, we will provide a small part of the explanation of the differences in these half-lives, although a full explanation of the phenomenon will require a treatment of tunneling, which is an aspect not yet included in TDDFT extended to include pairing correlations, see the discussion in Sec. XI.

In odd-mass and odd-odd nuclei, new order parameters appear in the static mean fields proportional to the spin density, a quantity similar to a local spin magnetization in the Ising model, and these order parameters give rise to a pseudomagnetic field $\mathbf{B}(\mathbf{r}) \propto \mathbf{s}(\mathbf{r})$ [101], and this pseudomagnetic field then acts on the nucleon spins just as a magnetic field acts on a spin 1/2 particle $\mathbf{B}(\mathbf{r}) \cdot \boldsymbol{\sigma} \propto \mathbf{s}(\mathbf{r}) \cdot \boldsymbol{\sigma}$. More specifically, the single-particle Hamiltonian

in density functional theory takes the form [102]

$$h(\mathbf{r}) = -\nabla \cdot \frac{\hbar^2}{2m^*(\mathbf{r})}\nabla + U(\mathbf{r}) - i\mathbf{W}(\mathbf{r}) \cdot (\nabla \times \sigma) \tag{35}$$
$$+ \mathbf{S}(\mathbf{r}) \cdot \sigma + \frac{1}{i}\left(\nabla \cdot \mathbf{A}(\mathbf{r}) + \mathbf{A}(\mathbf{r}) \cdot \nabla\right)$$

and the terms on the second line, specifically the mean fields $\mathbf{S}(\mathbf{r})$ and $\mathbf{A}(\mathbf{r})$, which depend on the spin and current densities, are non-zero in the case of dynamic calculations, including the highly non-equilibrium dissipative dynamical process of nuclear fission [21, 29–31], and also in static calculations of odd nuclei. These new "pseudomagnetic field" potentials do not respect time-reversal invariance, just as true magnetic fields do not. We will demonstrate below that the effect of these pseudomagnetic fields is significantly enhanced in the case of the induced fission of odd-mass and odd-odd compound nuclei when compared with the induced fission of even-even compound nuclei. As was mentioned above, a full microscopic explanation of the dramatically different spontaneous fission lifetimes between even and odd systems requires a treatment of quantum tunneling through the fission barrier. It was demonstrated by Caldeira and Leggett [103] that the time to tunnel through a barrier is dramatically affected by dissipation, and as our results below will indicate, the effects of dissipation in even and odd systems are quite different; hence, we expect that tunneling will be significantly different in even and odd systems as well. We focus on the time-reversal properties of the many-body wave function as well because it is known that this is crucial for the description of β-decay of FFs and also for P-even-T-odd asymmetries of angular correlations of FFs with light particles emitted during fission which is induced with cold polarized neutrons [104].

The inclusion of pairing is crucial to the theoretical treatment of nuclear fission. It was demonstrated using the extension of TDDFT to superfluid systems, known as the time-dependent superfluid local density approximation (TDSLDA), that induced fission dynamics of even-even compound nuclei is a highly non-equilibrium dissipative process [29–31], a finding which has now been accepted by the community [35] and which is in full agreement with experimental findings. The source of the dissipation is ultimately the pairing interaction, as time-reversed pairs of single-particle states may be scattered by the pairing interaction between upward-moving and downward moving single-particle energy levels as the nucleus deforms, thereby increasing the nucleus' internal excitation energy during the descent from saddle to scission, and also allowing the nucleus to deform with smaller than expected en-

ergy. Because of this redistribution of the single-particle occupation numbers, pairing plays a crucial role in the evolution of the nuclear shape, as was first demonstrated by G. Bertsch in the 1980's and 1990's [15, 17–19, 105, 106]. In odd systems, we know this picture will be modified to some degree. The extra odd nucleon cannot participate in the Cooper pair because of the Pauli exclusion principle, see Eq. (34), and the corresponding single-particle state cannot contribute to the anomalous density, which is the superfluid order parameter and is responsible for the redistribution of the single-particle occupation numbers. As a result, it must be the case that pairing correlations are inhibited relative to neighboring E-E nuclei. The effects of this inhibition are not *a priori* obvious, as when pairing is removed, it becomes very difficult to force the nucleus to fission without supplying large amounts of excitation energy, and when pairing is artificially enhanced, fission proceeds much more quickly and is nearly adiabatic.

Due to the technical difficulty of treating odd nuclei in a microscopic framework with pairing correlations, two approximations are often invoked, the Pauli blocking approximation [11] and the equal filling approximation (EFA) [107]. The Pauli blocking approximation is basically an extension of Eq. (34) to the case of a Hartree-Fock-Bogoliubov many-body wave function (MBWF), which is a superposition over states with different numbers of particles. In the Pauli blocking approximation, a single quasiparticle level is "blocked" and thus does not contribute to the anomalous density, but it does contribute to all the other one-body densities, thereby leading to the spontaneous breaking of time-reversal symmetry. On the other hand, in the case of the EFA, the nucleus is treated as even-even, with both the "blocked" quasiparticle level and its time-reversed partner instead each being occupied with equal probability, and thus the level is not truly "blocked" at all, and time-reversal symmetry is not broken. As the nucleus is treated as E-E, the pseudomagnetic fields vanish exactly, $\mathbf{B}(\mathbf{r}) \propto \mathbf{s}(\mathbf{r}) \equiv 0$, and instead the average proton and/or neutron number is adjusted to be an odd number [107]. Because no levels are excluded from the anomalous density, the effect of pairing correlations in the EFA is expected to be stronger than in the Pauli blocking approximation.

The EFA was used in the most recent and detailed microscopic fission calculations of odd-mass nuclei within density functional theory [108, 109], which also contained brief reviews of older and more simplified theoretical studies. A heuristic argument might suggest that employing the Pauli blocking or equal filling approximations lead to minor corrections–after

all, the correction to the particle number is at the level $1/A$, and so perhaps the corrections to other observables might be at the same level. Of course, we know this argument does not work and we must be much more careful, as spontaneous fission lifetimes constitute one example of an observable which is modified by several orders of magnitude when the particle number is merely changed by one [63]. In static calculations of odd nuclei, with the exception of the Pauli blocked state, all single-particle occupation probabilities are doubly degenerate, but as we will show below, under time evolution the time-reversal symmetry breaking terms destroy this double degeneracy, with significant consequences for the nuclear shape dynamics. This effect is present for even and odd systems, but the magnitude of the effect is significantly enhanced in the case of odd systems.

C. Results

We present the results of a large number of induced fission calculations for odd-mass and odd-odd compound nuclei within TDSLDA [67, 110], which does not rely on the Pauli blocking or equal filling approximations.. Specifically, we performed 23 simulations for ^{239}U, 43 simulations for ^{241}Pu, 35 simulations for ^{243}Pu, and 48 simulations for ^{238}Np, for a total of 149 trajectories, each prepared with different initial quadrupole and octupole deformations, (Q_{20}, Q_{30}), and started outside the outer fission barrier. The initial conditions were chosen at various deformations along the outer barrier, and were initially treated as E-E during the preparation of the deformed ground states. We call these even-even nuclei the "seed" nuclei, and their N and Z values were tuned via artificially adjusting the chemical potential to be identical to the target odd-mass or odd-odd nucleus. To produce a genuinely odd nucleus, we followed the established prescription in the literature [11, 108, 109, 111] and "flipped" various low energy quasiparticle states with occupation probabilities approximately 0.5. The "seed" nuclei are valuable to have for the sake of comparison, as from the perspective of the liquid drop formula, they have identical volume, surface, Coulomb, and symmetry energies, and hence the only difference is in the pairing gap(s) and the particle number parity of the MBWF. Accordingly, we also simulated the fission of these "seed" nuclei as well, producing 6 ^{239}U trajectories, 13 ^{241}Pu trajectories, 10 ^{243}Pu trajectories, and 11 ^{238}Np trajectories, see Fig. 8.

For all the fission calculations performed for this study, we employed the SeaLL1 nuclear

TABLE II. A summary of the fission fragment properties for all the fission trajectories performed in this study. The FF particle numbers, the TKE, and the number of runs performed for each system, with their standard deviations listed in parentheses. Runs are categorzied as "symmetric" and "asymmetric" depending on the initial octupole deformation Q_{30} of the compound nucleus being smaller or larger than ≈ 2.5 b$^{3/2}$. The "Treatment" column contains entries O–O, O–E, E–E, which respectively stand for the evenness/oddness of the neutron and proton many-body wave functions. In case of ^{235}U(n,f) and ^{239}Pu(n,f) we have included in the table the corresponding fragment properties obtained in previous studies [32, 112, 113], but never reported until now. Our results for TKE agree with Madland systematics to within 1 MeV for ^{239}Pu(n,f) and ^{235,238}U(n,f) [114]. Average properties of FFs from TDSLDA simulations can be compared with CGMF results, see the supplemental online material for this paper, which in turn are based on available experimental data [115]. However, it is challenging to make a direct comparison with experimental data for all observables, given that corrections must be included into the experimental analysis to extract the pre-neutron emission information.

	Treatment	Type	TKE	Z_H	Z_L	A_H	A_L	No. Runs
^{235}U(n,f)	E–E	asym.	168.71(4.03)	52.07(0.84)	39.94(0.84)	134.85(2.24)	101.16(2.24)	22
^{235}U(n,f)	E–E	sym.	142.35(3.05)	47.36(1.35)	44.64(1.35)	121.60(3.58)	114.40(3.58)	2
^{237}Np(n,f)	O–O	asym.	174.68(4.34)	52.34(0.56)	40.66(0.53)	135.11(1.45)	102.90(1.35)	46
^{237}Np(n,f)	E–E	asym.	175.36(2.75)	52.18(0.27)	40.84(0.27)	134.52(0.73)	103.50(0.72)	10
^{237}Np(n,f)	O–O	sym.	151.04(1.30)	49.53(0.05)	43.50(0.05)	127.37(0.05)	110.69(0.02)	2
^{237}Np(n,f)	E–E	sym.	148.24	49.90	43.10	128.36	109.66	1
^{238}U(n,f)	O–E	asym.	169.08(3.56)	51.85(0.49)	40.15(0.49)	135.43(1.29)	103.54(1.32)	23
^{238}U(n,f)	E–E	asym.	169.40(1.36)	51.60(0.32)	40.40(0.32)	134.79(0.80)	104.21(0.80)	6
^{239}Pu(n,f)	E–E	asym.	176.85(1.00)	53.09(0.21)	40.91(0.21)	136.49(0.43)	103.51(0.43)	5
^{239}Pu(n,f)	E–E	sym.	150.03(1.16)	49.87(1.02)	44.13(1.02)	128.46(2.57)	111.54(2.57)	2
^{240}Pu(n,f)	O–E	asym.	173.88(4.18)	52.71(0.75)	41.29(0.75)	136.03(1.79)	104.93(1.80)	36
^{240}Pu(n,f)	E–E	asym.	173.98(3.00)	52.79(0.75)	41.21(0.75)	136.15(1.66)	104.85(1.66)	10
^{240}Pu(n,f)	O–E	sym.	151.58(3.59)	50.70(0.76)	43.19(0.75)	131.11(1.92)	109.69(1.76)	7
^{240}Pu(n,f)	E–E	sym.	151.26(2.64)	51.00(0.42)	42.88(0.47)	131.48(1.23)	109.41(1.27)	3
^{242}Pu(n,f)	O–E	asym.	171.50(4.96)	52.51(0.61)	41.49(0.61)	136.62(1.41)	106.40(1.42)	32
^{242}Pu(n,f)	E–E	asym.	170.04(2.99)	52.58(0.59)	41.42(0.60)	136.78(1.40)	106.21(1.42)	9
^{242}Pu(n,f)	O–E	sym.	151.41(1.38)	50.78(0.34)	43.22(0.34)	132.54(0.83)	110.48(1.00)	3
^{242}Pu(n,f)	E–E	sym.	151.62	50.72	43.28	131.95	111.05	1

energy density functional [12], which is an accurate modern functional, but the functional

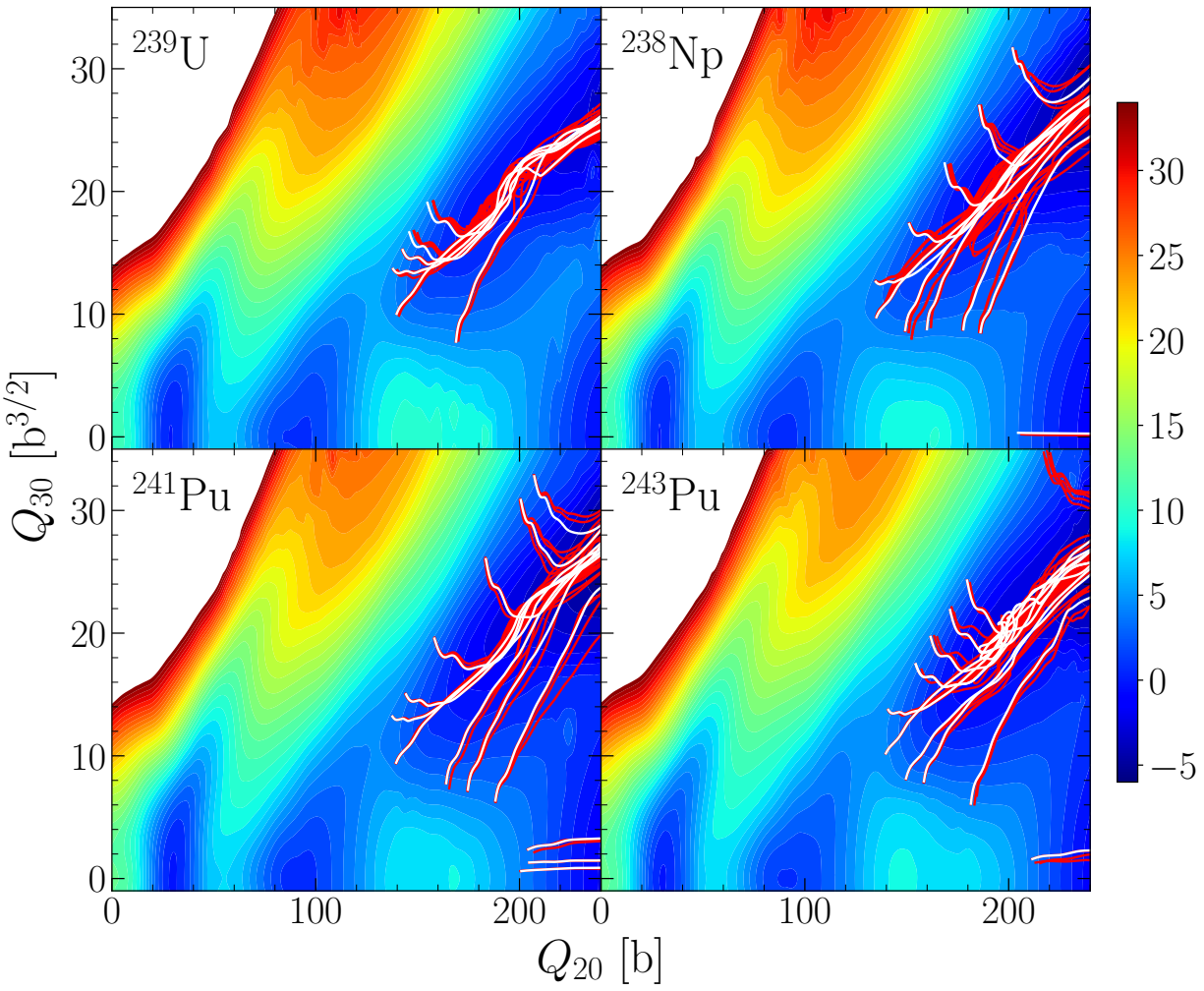

FIG. 8. All the TDSLDA fission trajectories considered in this study are plotted over the corresponding potential energy surface for the appropriate nucleus. Even-even "seed" nuclei are shown in white and genuine odd nuclei are shown in red. The nearly-symmetric trajectories which are defined by having a relatively small value of $Q_{30}(t = 0)$ are not visible as they extend beyond the limits of the plot. We show them instead in Fig. 12. The initial conditions were chosen along the rim of the outer fission barrier according to the same criteria as in previous studies [9, 29–32, 116].

parameters were tuned overwhelming to describe even-even nuclei, see [117] for one of the most recent studies and for earlier references. The magnitude of the time-reversal symmetry breaking terms in the functional are accordingly only known from a limited number of studies [12, 101, 118], and are thus not as strongly constrained, and so it is possible that the actual role of these terms could be even larger than what we present here.

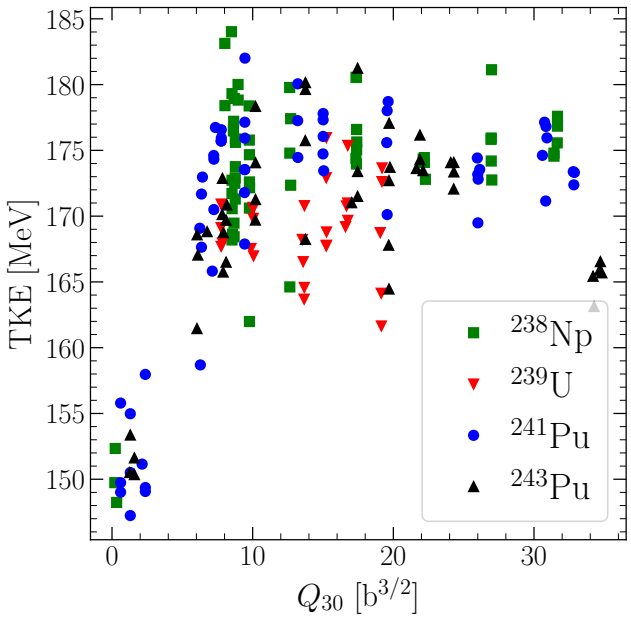

FIG. 9. The total kinetic energy of the fission event as a function of the initial left-right asymmetry of the nucleus for all fission trajectories considered in this study. Notice that the trajectories split rather cleanly into two groups, depending on whether or not $Q_{30}(0) \lesssim 2.5$ b$^{3/2}$.

We present the fragment properties from all the trajectories considered in this study in Table II, and several differences can be observed. In particular, we find that for genuinely odd systems, the distribution of the TKE and also the particle numbers are often as much as twice as wide as for the even-even "seed" nucleus comparison case, as measured by the standard deviation. We emphasize that we are simply reporting the mean and standard deviation *of our datasets*, which will not be directly comparable to experiment, as we have not accounted for neutron and gamma emission, and furthermore we do not yet have a method for assigning a probability distribution to the initial configurations along the outer rim of the fission barrier. Nevertheless, the difference is striking, and it suggests that proper treatment of time-reversal symmetry breaking may be necessary to accurately reproduce FF distributions in time-dependent treatments of the fission process.

Another interesting aspect we observed from our simulations is that the value of the TKE can be significantly affected by the choice of the initial octupole deformation, $Q_{30}(0)$, see Fig. 9. For values $Q_{30}(0) \lesssim 2.5$ b$^{3/2}$, the fragment distributions are nearly symmetric and the TKE is noticeably smaller, which is consistent with what we have observed in earlier

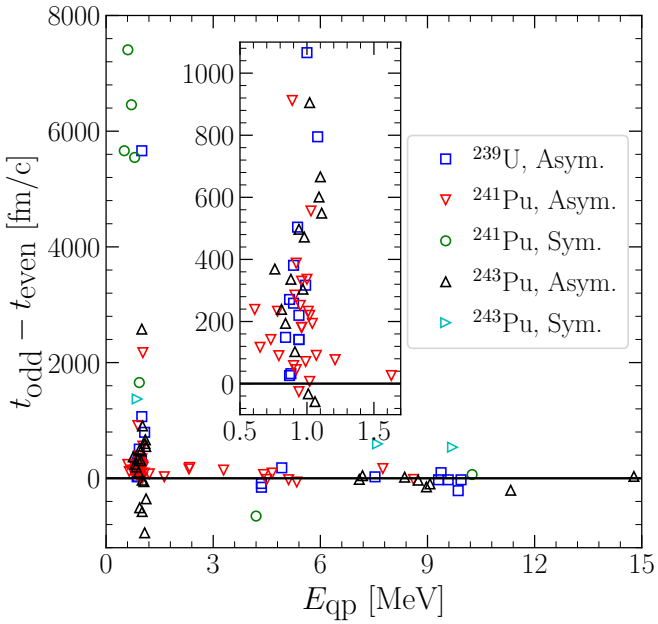

FIG. 10. Difference in saddle-to-scission times for odd nuclei and their corresponding even-even "seed" nucleus. Odd systems with initial "blocked" quasiparticle states with energies $E_{qp} < 1$ MeV often show dramatically longer saddle-to-scission times, sometimes as much as a factor of four longer than their even-even "seed" nucleus counterparts. Invariably it is the case that longer saddle-to-scission times are accompanied by "circuitous" or "confused" evolution of the nuclear shape prior so scission, see Fig. 12.

TDSLDA studies of induced fission of E-E compound nuclei [30]. Furthermore, it is very often the case that trajectories with low initial octupole deformation appear to be "confused," as the nuclear shape may wander considerably on the PES prior to scission, leading in some cases to dramatically longer saddle-to-scission times, provided the quasiparticle excitation is not too high in energy, see Figs. 10, 11, and 12. When implementing the prescription to transform the even-even seed nucleus to an odd nucleus, we chose a rather wide range of energies for the quasiparticle states to block, which led to a wide distribution of initial energies of the compound nuclei. When these initial quasiparticle states had low energies, the compound has a relatively low intrinsic energy near the outer barrier, but still the level density is significantly higher than in the case of an even-even nucleus similarly prepared, as we mentioned in the introduction. As a result, there is a larger number of potential energy surfaces per unit energy for these odd systems, and so the pairing interaction can scatter

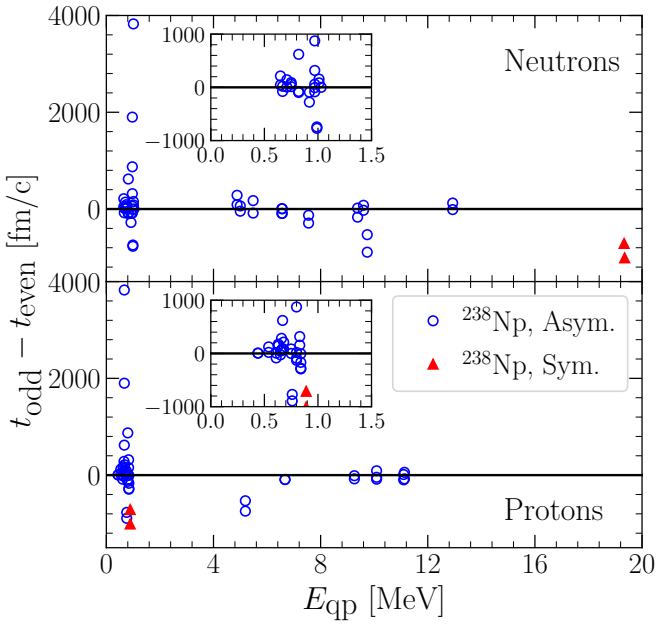

FIG. 11. Same as Fig. 10, but ^{238}Np, so both the neutron and proton quasiparticle energies are shown.

pairs more frequently between these closely spaced surfaces, which leads to an enhanced role of dissipative effects. This behavior was also observed in [45], where TDSLDA was supplemented to include stochastic terms. At the level of the nuclear shape, the frequent jumps between these many low-lying PESs lead to a very "rough" landscape on which the nuclear shape evolves, and it is this "roughness" which is origin of the circuitous trajectories shown in Fig. 12 and the correspondingly longer saddle-to-scission times.

Another significant result from our simulations is shown in Fig. 13. We prepared an odd system using the procedures referenced above, and then we transformed the initial state into the canonical basis, a transformation which does not at all affect dynamics, see [7] and Sec. VIII. Under dynamics, the canonical basis does not remain canonical (i.e., the single-particle states do not remain eigenstates of the density matrix), and we can also follow the occupation probabilities of the single-particle states as a function of time. Fig. 13 clearly demonstrates that an initially blocked state does not remain so over time, meaning that the Pauli blocking approximation is strongly violated under dynamics. One can always instantaneously transform to the canonical basis by diagonalizing the density matrix at a given time, in which case there will be a single non-degenerate level corresponding to the

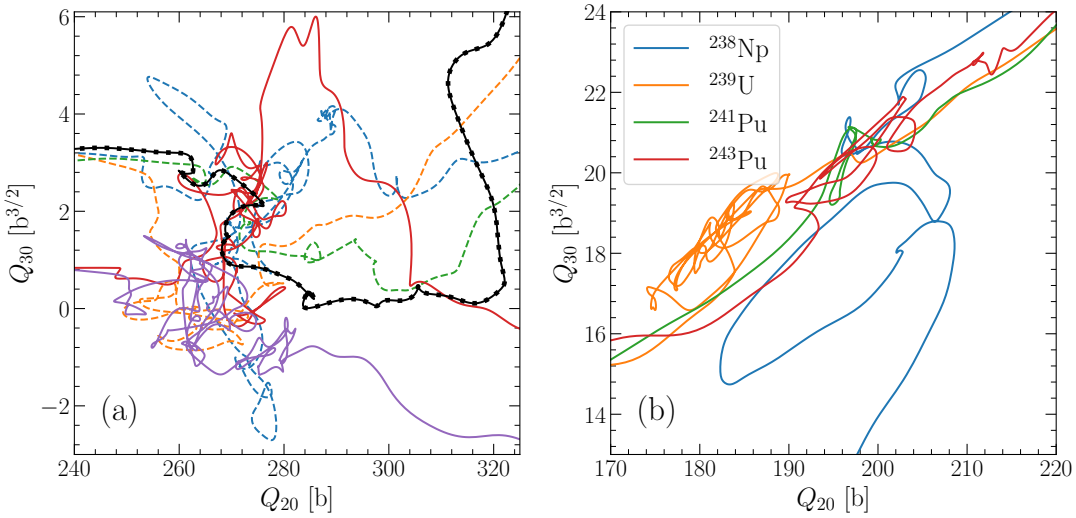

FIG. 12. Nuclear shape evolution for TDSLDA trajectories which exhibit long saddle-to-scission times, see Figs. 10 and 11. On the left are trajectories for ^{241}Pu only, and all of them have low initial octupole deformation Q_{30}, and as a rule, low final TKE. The trajectory for just one even-even "seed" nucleus is shown in black with dots. On the right are shown trajectories for all four isotopes which do not have small initial Q_{30}, but which still exhibit longer saddle-to-scission times. Note that these asymmetric circuitous trajectories occur with less frequency than nearly-symmetric circuitous trajectories. In all cases where the nuclear shape evolution is circuitous, the saddle-to-scission time is longer than for a "smoother" trajectory started from a similar initial deformation.

Pauli blocked state, but it is important to remember that one cannot straightforwardly use this basis for dynamics, and that the canonical occupation probabilities are not the same as the occupation probabilities one obtains in static density functional theory calculations from the v_k solutions of the Hartree-Fock-Bogoliubov equations.

Finally, we can see clearly the significantly enhanced effect of the time-reversal symmetry breaking terms, the dynamically generated pseudomagnetic field terms in the mean field, by observing the evolution of the initially doubly-occupied "Kramers doublets," see Fig. 14. The initial state is prepared in the canonical basis, where because of the time-reversal symmetry, all the canonical single particle states are doubly occupied, with the exception of the one Pauli blocked level, for the case of an odd compound nucleus. For an even-even system, all the canonical single-particle levels will be doubly occupied. But we see that under dynamics, for both even and odd compound nuclei, these initially doubly degenerate

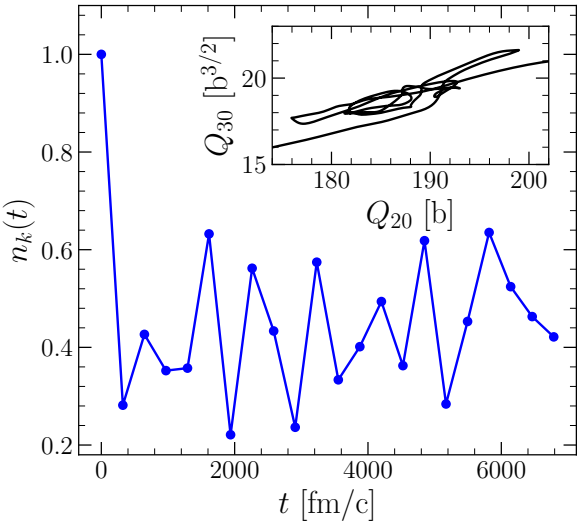

FIG. 13. The time-dependent occupation probability $n_k(t) = \langle v_k(t)|v_k(t)\rangle$ for a chosen Pauli blocked quasiparticle state in ^{239}U. For the initial state, the system is prepared in the canonical basis, the eigenbasis of the number density matrix, which one can always do without altering the dynamics [7]. In the canonical basis, an odd system always has a single quasiparticle state occupied with probability precisely 1.0. Under dynamics, however, the quasiparticle wave functions do not remain in the canonical basis. The inset shows the evolution of the nuclear shape during the time interval 280-5000 fm/c.

levels cease to be degenerate, which is a direct consequence of the time-reversal symmetry breaking contributions to the mean field. The effects are significantly enhanced for the odd nucleus, as one can see in Fig. 14, and as the single-particle occupation probabilities play such a crucial role in the nuclear shape evolution, as we discussed extensively above in this section and the Introduction, this breaking of the Kramers degeneracy can be understood as another aspect of the different nuclear shape dynamics and the modified role of dissipation for odd-mass and odd-odd nuclei.

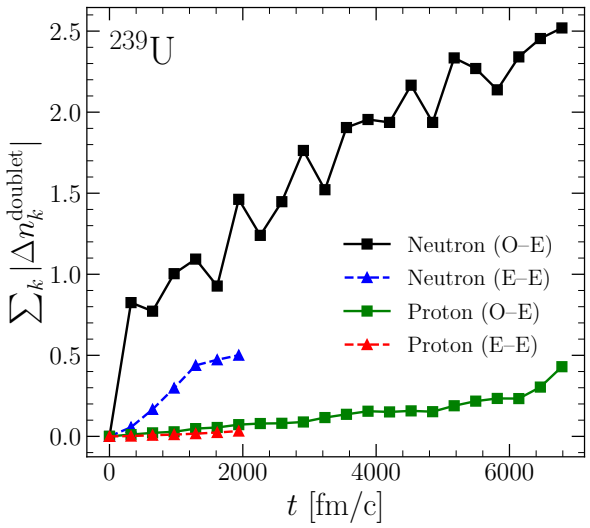

FIG. 14. The degree of breaking of "Kramers doublets" as a function of time, as measured by the sum of the absolute difference of the occupation probabilities of states which are doublets at $t = 0$. The run starts in the canonical basis and the neutron level which is occupied with precisely $n_k(0) = 1$ is excluded from the sum. The breaking of these doublets is due to the presence of time-reversal symmetry breaking terms in the TDSLDA quasiparticle Hamiltonian.

VI. SPATIAL ORIENTATION OF THE FISSION FRAGMENT INTRINSIC SPINS AND THEIR CORRELATIONS

In this section, we review the results presented in "Spatial orientation of the fission fragment intrinsic spins and their correlations" by G. Scamps, I. Abdurrahman, M. Kafker, A. Bulgac, and I. Stetcu, Phys. Rev. C **108**, L061602 (2023) [9].

A. Abstract

The generation and dynamics of fission fragment (FF) angular momentum is still not well understood, despite fission having been discovered over 80 years ago, as was demonstrated by new experimental and theoretical results in 2021. In particular, in the case of the intrinsic spins of the fission fragments, their magnitude, spatial orientation, and correlations are not understood. It is important to understand the FF intrinsic spin properties as these play a crucial role in defining the angular distribution of emitted prompt neutrons, as well as their correlations, and subsequent emission of γ rays and their correlations. Here we present an evaluation of the fission fragment intrinsic spins within a microscopic framework, time-dependent density functional theory extended to superfluid systems, known as the time-dependent superfluid local density approximation (TDSLDA). We evaluate the FF intrinsic spins, for both even- and odd-mass fission fragments, as well as their spatial correlations. We find the the FF intrinsic spin dynamics have a three dimensional character, as the "twisting" spin modes are excited, and the FF intrinsic spins are not confined to the plane perpendicular to the fission axis, as has been widely claimed in semiphenomenological models.

B. Introduction

The FF intrinsic spins were measured with a high degree of accuracy in an experiment in 2021 by Wilson *et al.* [119]. The FF spins had been measured previously in similar experiments almost 50 years ago [120, 121]. Around the same time in 2021, there were several new theoretical studies as well, coming from both phenomenological and microscopic approaches, which aimed to determine various properties of the FF angular momenta and their correlations [32, 122]. Immediately following this period, more theoretical studies were performed [112, 123–130], and ultimately a productive workshop was convened [131].

Perhaps the simplest case to consider, both theoretically and experimentally, for the problem of determining the FF intrinsic spins is the spontaneous fission of ^{252}Cf. This is because the ground state of ^{252}Cf is a cold isolated quantum system with spin and parity $S_\pi = 0^+$. After the nuclear neck ruptures, the FFs are known to be highly excited, and it was shown using TDSLDA that the heavy FF (HFF) is generally colder than the light FF (LFF) [29–31]. TDSLDA simulations also revealed that the HFF has smaller average intrinsic spin than the LFF [32], which contradicted the previous consensus in the literature, which stated that the LFF had a larger average intrinsic spin than the HFF, see for example [49, 50, 52, 120, 122, 132]. As TDSLDA was the first fully microscopic framework to offer input on this question, the fact that it contradicted the existing consensus in the literature indicated that the assumptions made in modeling fission dynamics and decay properties of FF needed to be examined more carefully. Subsequent theoretical and phenomenological studies incorporated these new results [123, 124]. Recently, TDSLDA was also used to investigate the relative angular momenta of the FFs [112]. As the total angular momentum of the system must be conserved, for the case of ^{252}Cf, we have

$$\hat{\boldsymbol{S}}_H + \hat{\boldsymbol{S}}_L + \hat{\boldsymbol{\Lambda}} = \boldsymbol{S}_0 \approx \boldsymbol{0}, \tag{36}$$

where $\hat{\boldsymbol{\Lambda}} = \hat{\boldsymbol{R}} \times \hat{\boldsymbol{P}}$ is the relative orbital angular momentum perpendicular to the fission axis, $\hat{\boldsymbol{R}}, \hat{\boldsymbol{P}}$ are the the relative separation between the FFs and their relative linear momentum respectively, $\boldsymbol{S}_0$ is the intrinsic spin of the compound (or ground state, in the case of spontaneous fission), and finally $\Lambda_z = 0$. To approximate the final equality as zero is exact for the case of ^{252}Cf, but it is also a reasonable approximation in the case of induced fission with low-energy incident neutrons on, for example, ^{235}U, ^{239}Pu targets. At this point, a very important question arises which has not yet been resolved experimentally or theoretically [127]: are the FF intrinsic spins $\boldsymbol{S}_{H,L}$ perpendicular to the fission axis? Evidently, the sum of these two spins, $\hat{\boldsymbol{S}}_H + \hat{\boldsymbol{S}}_L$, is, in the case of ^{252}Cf(sf). On this question there are strong disagreements between microscopic TDSLDA predictions [112, 126] and phenomenological predictions of the FREYA model [122, 124, 127, 133]. As the orientation of the FF intrinsic spins will affects the direction of emission of prompt neutrons and gammas, it is one of the most pressing experimental questions in the field of nuclear fission today [134]. In this study, we again used TDSLDA to investigate the properties of the FF intrinsic spins, and we find a stark disagreement with predictions from the phenomenological predictions from

the FREYA model [122, 124, 127], the only other source of clear information available in the literature.

The first indication that TDSLDA differed from FREYA on the question of the distribution of the opening angle between the intrinsic spins was reported in Refs. [112, 126]. FREYA results [122, 124, 127] suggested that the opening angle distribution between the FFs should be nearly uniform, whereas the microscopic results were clearly not uniform. One assumption adopted by FREYA, at least prior to the publication of this study, and which we argue based on the results below is not supported by microscopic calculations, is that the FF intrinsic spins are necessarily perpendicular to the fission axis, which means that the twisting and tilting modes [135–137] are artificially excluded from fission dynamics. However, a drawback of the theoretical study [112] was that and angular momentum projection on several angles was technically too difficult, so some assumptions about the angular momentum "triangle" in Eq. (36) were made. In this study, on the other hand, two technical developments (which are reported in the supplemental information for this paper [9]) enable us to easily evaluate the triple distribution $P(\Lambda, S_H, S_L)$ exactly, without having to rely on any such assumptions.

C. Results

The angular momentum projection for the fission fragments is performed using well-known and established projection techniques [11, 138–141], which we illustrate here for a specific fragment,

$$\hat{P}^{S}_{MK} = \frac{(2S+1)}{16\pi^2} \int d\Omega \mathcal{D}^{S*}_{MK}(\Omega)\, e^{i\alpha\hat{S}_z} e^{i\beta\hat{S}_y} e^{i\gamma\hat{S}_z}, \tag{37}$$

$$P(S_F, K_F) = \langle\Psi|\hat{P}^{S_F}_{K_F K_F}|\Psi\rangle, \tag{38}$$

where $\Omega = (\alpha, \beta, \gamma)$ represents a separate set of the three Euler angles for each FF, $|\Psi\rangle$ is the many-body wave function, and $P(S_F, K_F)$ refers to the joint probability distribution that either the light or heavy fragment has intrinsic spin $S_F = S_L, S_H$ and the projection of that intrinsic spin, K_F, on the fission axis in the fragment's rest frame. M is the projection of the FF intrinsic spin S onto the fission axis in the laboratory frame. The angular momenta $\hat{S}_{x,y,z}$ are defined in a spatial region around a specific FF in its center-of-mass frame [32]. Here, we wish to evaluate $P(S_F, K_F)$ for each FF, as well as the triple angular momentum

distribution

$$P(\Lambda, S_H, S_L) = \sum_{k_H k_L} \langle \Psi | \hat{P}^{\Lambda}_{0,0} \hat{P}^{S_H}_{K_H K_H} \hat{P}^{S_L}_{K_L K_L} | \Psi \rangle, \tag{39}$$

which can be shown to be given exactly by the expression

$$\begin{aligned} P(\Lambda, S_H, S_L) = & \sum_{K_H K_L K'_H K'_L} (-1)^{K'_H - K_H + K'_L - K_L} \\ & \times C^{\Lambda,0}_{S_H,-K_H,S_L,-K_L} C^{\Lambda,0}_{S_H,-K'_H,S_L,-K'_L} \langle \Psi | \hat{P}^{S_H}_{K_H K'_H} \hat{P}^{S_L}_{K_L K'_L} | \Psi \rangle, \end{aligned} \tag{40}$$

where $C^{J,M}_{j_1,m_1,j_2,m_2}$ are Clebsch-Gordan coefficients. We note that a similar formula was presented by T. Døssing during the previously mentioned *Workshop of Fission Fragment Angular Momenta* [131] and also discussed in Refs. [126, 129, 130]. The Clebsch-Gordan coefficients emerge naturally, and ensure that angular momentum conservation, see Eq. (36), is automatically satisfied. The LISE TDSLDA [21] code with the SeaLL1 nuclear energy density functional was used to simulate the fission dynamics and evaluate the many-body wave function $|\Psi\rangle$ used in Eq. (39). Furthermore, to evaluate the fragment FF intrinsic spin probability distributions, at the final time of the simulation, we performed a unitary transformation to the canonical quasi-particle states [66] as they provide the most economic representation of a many-body wave function, which in turn renders the numerical calculations less expensive computationally. Furthermore, the overlaps in Eq. (40) involve the evaluation of Pfaffians [139, 140], and these were calculated numerically using the algorithms published by Wimmer [142].

For each FF, we define the angle between the intrinsic spin $\boldsymbol{S}_{H,L}$ and the fission axis (in the fragment's rest frame) as

$$\cos\theta_F = \frac{K_F}{\sqrt{S_F(S_F+1)}}, \text{ where } F = H, L \tag{41}$$

and we also define the opening angle between the two intrinsic spins as [32]

$$\varphi_{HL} = \arccos\left(\frac{\Lambda(\Lambda+1) - S_H(S_H+1) - S_L(S_L+1)}{2\sqrt{S_H(S_H+1)S_L(S_L+1)}} \right). \tag{42}$$

There is no issue in defining these angles provided that $S_{H,L} \neq 0$. Once we have the triple distribution $P(\Lambda, S_H, S_L)$, it is straightforward to extract the probability distributions for the two angles defined above, $P(\theta_F)$ and $P(\varphi_{HL})$.

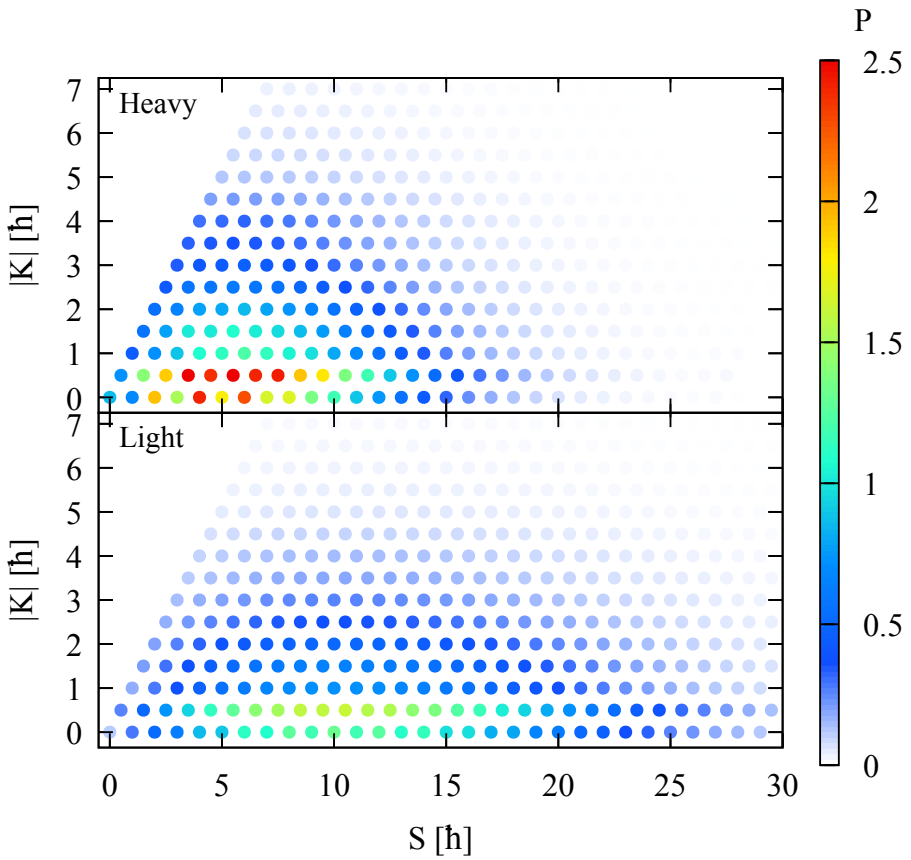

FIG. 15. The joint distribution for the fragment intrinsic spin and its projection onto the fission axis in the fragment rest frame, given by Eq. (38). The distribution for the HFF is evaluated in the top panel, and the LFF in the bottom panel. Since for both fragments it is the case that $P(S,K) = P(S,-K)$, we show the distribution of $|K|$.

We show the distributions for the FF intrinsic spins and their projections in Figs. 15 and 16. As one might have expected, these distributions are supported for both integer and half-integer values of K. Integer values of K correspond to even-even or odd-odd fragments, whereas a half-integer value of K means the fragment is odd-mass. We see from Fig. 15 that the spread of intrinsic spins for the LFF is wider than that for the HFF, in agreement with the results reported in [32, 123]. Another surprising aspect of these figures is that there is no odd-even staggering in the fragment yields, which is consistent with the lack of odd-even staggering in experimental fragment mass yields, although we remind the reader that TDSLDA does not incorporate prompt neutron and gamma emission, and correcting

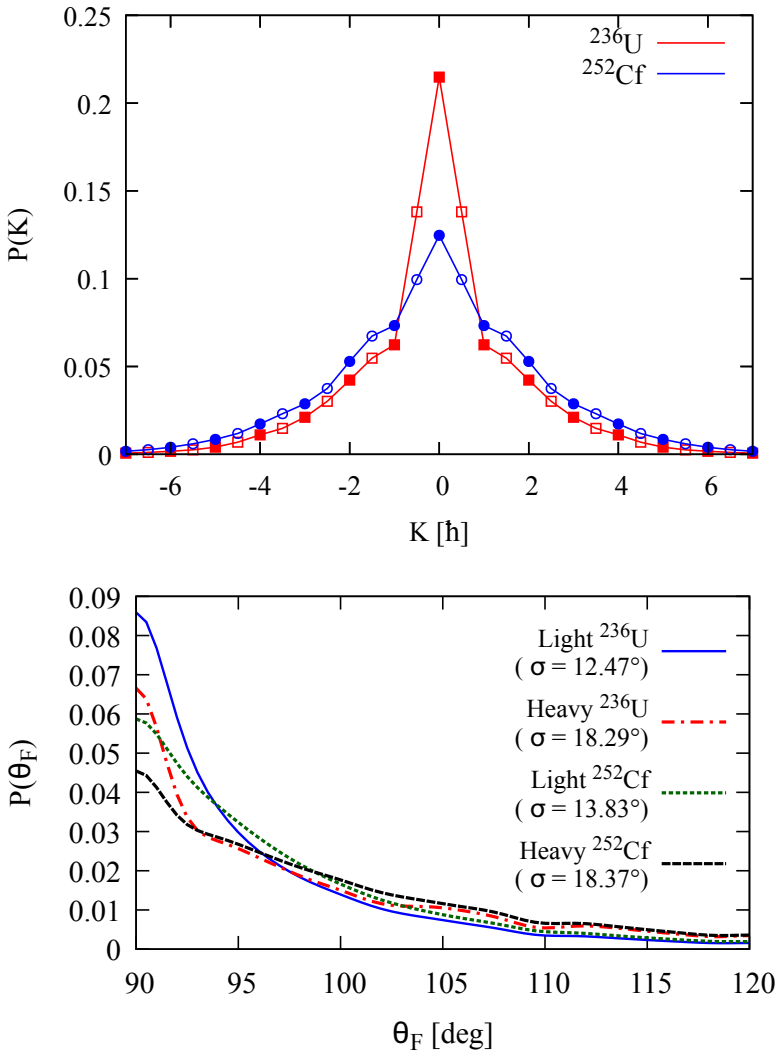

FIG. 16. In the top panel, we show the probability distribution for the quantum number K, the projection of the FF intrinsic spin onto the fission axis in the fragment rest frame. Since $K_H + K_L = 0$ the distributions for the HFF and LFF are identical. Integer values of K are represented by filled symbols and half-integer values with empty symbols. In the bottom panel, we show the probability distribution for the angle between S and K, computed using Eq. (41). The data here are convolved with a Gaussian of width 2° and shown here only for angles $\theta_F \geq 90°$, since $P(\theta_F)$ is symmetric with respect $\theta_F = 90°$.

for this emission is subject to model dependence.

However, the most remarkable aspect of the FF intrinsic spin probability distributions is shown in Fig. 16, where the distributions

$$P(K) = P_H(K) = P_L(K) = \sum_{S_{L,H}} P(S_{L,H}, K_{L,H}) \tag{43}$$

show the significant probability of finding a nonzero value of K, which is to say a significant probability that the FF intrinsic spin is not oriented perpendicular to the fission axis, and therefore that the twisting spin modes are active and cannot be neglected. This feature is in stark contrast with assumptions that have been made in the FREYA model for the past 15 years [122, 124, 127, 133], that the FF intrinsic spins are perpendicular to the fission axis and that therefore the tilting and twisting modes are not active in nuclear fission. The argument for suppressing these modes is also used in the treatment of particle transfer in heavy ion collisions [143, 144]. This assumption also played a key role in the claimed agreement [124] with the recent experimental results obtained by Wilson *et al.* [119] in 2021. We remind the reader that one difference between TDSLDA and FREYA is that in FREYA the intrinsic spins are treated classically and there is accordingly no difference between integer and half integer spins for the FFs, and therefore one cannot make any statement as to whether even-odd staggering is present in the FREYA fragment distributions.

In Fig. 16, one observes that there is a sharp peak in the K distribution for $K \leq 1/2$, connected to rather long tails in the distribution. For ^{252}Cf and ^{236}U, we have $P(-1/2) + P(0) + P(1/2) \approx 0.33$ and ≈ 0.49 respectively, meaning that more than half the time one expects to find a fragment with spin projection $|K| \geq 1$! Thus, with high probability, the FF intrinsic spins are in fact not perpendicular to the fission axis after all, according to fully microscopic time-dependent density functional theory calculations. Instead, they are likely to be found with some projection along the fission axis, although they will necessarily be opposite to one another, as $K_H + K_L = 0$. As a result of this, returning to the angular momentum triangle of Eq. (36), more than half the time, the plane defined by the triangle forms an angle θ_F significantly different than 90° with the fission axis, which is demonstrated clearly by the lower panel of Fig. 16. One obtains very similar values for θ_F using the expectation values of $K_F^2 \approx 1.6 - 4.4$ reported in [32]. Another aspect which is relevant in the generation of angular momentum of the fission fragments is the reorientation effects due to the Coulomb interaction acting between the separated FFs, which can increase the

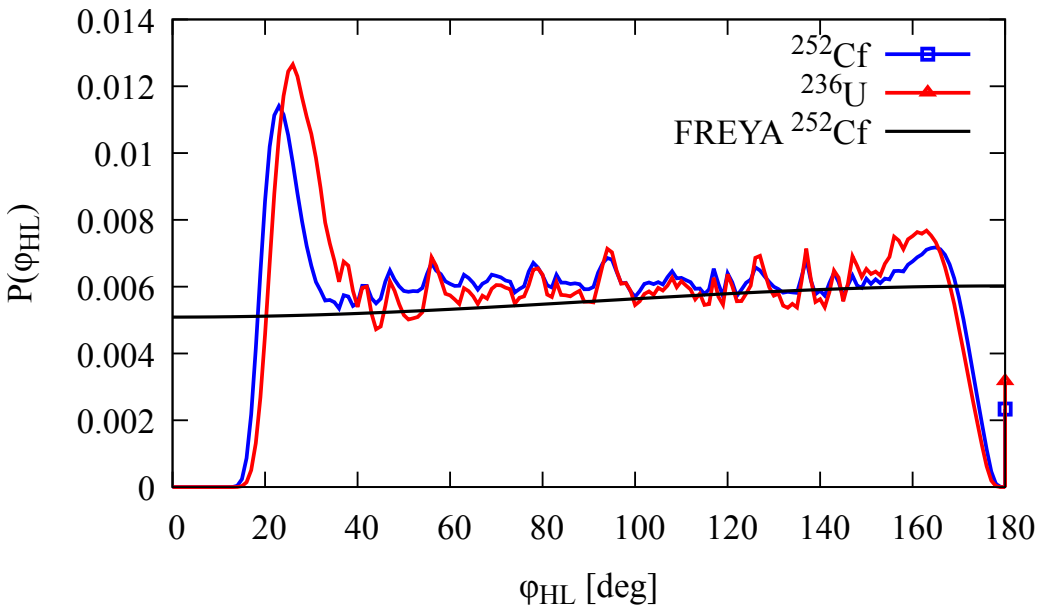

FIG. 17. The probability distribution for the opening angle φ_{HL} between the fragment spins, calculated using Eqs. (42) and (40). Again, this distribution was produced by convolving with a Gaussian with width 2° for smoothing purposes. The data point at 180° is shown separate from the rest of the curve, as when visualized at higher resolution this spin configuration is clearly distinct from those for $\varphi_{HL} < 180°$, although the distinction is not as sharp as those close to $\varphi_{HL} = 0°$.

intrinsic spins by 1-2 $\hbar$ [129, 130].

Another point of disagreement between the microscopic and phenomenological approaches is the opening angle distribution between the fragment spins, shown in Fig. 17. The first microscopic results for this distribution were presented in [112, 126] and stood starkly in contrast to the FREYA results [122, 124, 127], a fact which generated considerable discussion at the 2022 fission workshop [131]. However, as mentioned above, technical difficulties meant that the early microscopic results had to rely on two-angle formulas rather than full angular momentum projection [112, 126], an approximation which we do not make here, as the technical challenges have been overcome, and the resulting exact distribution is shown in Fig. 17. The opening angle distribution is nearly uniform in the region $\varphi \in (40°, 160°)$, but decays sharply around 0° and 180^0. Note that a totally flat distribution would indicate no correlation between the fragment spin directions, which is close to what is seen in FREYA

results [122, 124, 127, 133]. Note also that the probability that the opening angle exceeds 90° is approximately 0.53, which indicates a slight bias towards the bending modes in comparison with the wriggling modes. The microscopic results also show peaks at $\varphi_{HL} \approx 20°$, and $\approx 165°$, with the former being slightly larger in magnitude than the latter. The origin of these peaks is the Clebsch-Gordan coefficients in Eq. (40), which favor opening angles close to 0° and, to a lesser extent, 180°.

D. Conclusions

Analysis of the FF intrinsic spins from microscopic TDSLDA simulations reveal that the intrinsic spin dynamics are three dimensional in character, with the fragment spins not being confined to the plane perpendicular to the fission axis, which means that all the intrinsic spin modes conjectured to exist almost 60 years ago [135–137] are indeed active, see Figs. 15 and 16. The signal is clearest in the case of ^{252}Cf, where the distribution of the K quantum number is widest, revealing a very high probability that the FF intrinsic spins are not perpendicular to the axis. The microscopic results unambiguously demonstrate that the collective twisting modes are indeed active, which is in agreement with earlier microscopic results [32]. However, it was assumed in earlier microscopic studies [112, 126] that the FF intrinsic spin dynamics are unrestricted in 3D, which the opening angle distribution presented in Fig. 17 reveals is not the case. Of course, ultimately only experiment can reveal what actually occurs in nature, and since the FF intrinsic spin orientations will affect the properties of prompt neutrons and gammas, it is likely that if the FF intrinsic spins are actually not perpendicular to the fission axis, this will lead to measurable effects which are in principle accessible in experiments [128, 134].

It is often stated in the literature that one mechanism for generating 3D FF intrinsic spin dynamics is the breaking of pairs [134]. Before concluding, we offer some brief comments on this perspective. Pairing is included explicitly in microscopic TDSLDA calculations [29–31, 45, 46, 112, 145] in a self-consistent and time-dependent manner. During saddle-to-scission evolution, where the internal excitation energy of the compound nucleus increases, and also in studies where the initial excitation energy of the compound is increased, the neutron-neutron and proton-proton short range correlations never vanished, as indicated for example by the single-particle occupation probability distribution, even though the consid-

erable excitation energy of the system corresponds to a high temperature where a pairing condensate does not exist. What happens instead is that the phase of the pairing condensate is no longer constant across the nucleus, although the magnitude remains nonzero, which is also known to occur in heavy ion collisions at rather large collision energies [46, 66, 145, 146]. The survival of short range correlations between proton or neutron pairs to high excitation energy should not be conflated with pair breaking, however. Although long range order is lost, manifested by the loss of phase coherence of the pairing condensate, it is possible that in this case new nucleon pairs can be formed with nonzero total spin. Nevertheless, the $L = 0$ short range correlations clearly survive in the fission cases considered here.

As mentioned above, experimental input on the question of the FF intrinsic spin dynamics is highly desirable, a perspective which is shared by Randrup [127]. The only model which leads to testable predictions is the semiphenomenological code FREYA [122, 124, 127, 133], which is based on a number of fitting parameters and assumptions. As we showed convincingly in this study, FREYA and TDSLDA lead to dramatically different predictions, which derives from the assumption in FREYA that the FF intrinsic spins, which are treated classically, are exactly perpendicular to the fission axis and thus that the twisting mode is inactive. Sobotka [134] has argued that the angular distribution of the stretch $\gamma(E2)$ with respect to the fission axis is the most promising experimental signature to clarify the scission physics, and new experiments are now planned to resolve the discrepancies between old results [120, 121].

VII. MEASURES OF COMPLEXITY AND ENTANGLEMENT IN MANY-FERMION SYSTEMS

In this section, we review the results presented in the paper "Measures of complexity and entanglement in many-fermion systems" by A. Bulgac, M. Kafker, and I. Abdurrahman, Phys. Rev. C **107**, 044318 (2023) [10].

A. Abstract

There is no widely accepted, unique definition of the complexity of a many-body wave function (MBWF) for a fermionic system in the presence of interactions. The simplest possible fermionic MBWF is the Slater determinant. In many-body methods such as the shell model or the configuration interaction (CI) approach, the MBWF is represented as a superposition over Slater determinants, and in practice, the superposition usually comprises a very large number of terms. For example, in the case of (CI), the number of Slater determinants can reach upwards of 20 billion terms [147]. Although this number is often used informally to characterize the complexity of the MBWF, it is not a unique characterization, as it depends on the basis of single-particle wave functions (SPWFs) one uses, as well as the number of single-particle states one includes in the calculation. We propose a new definition of the MBWF complexity which is not situation-dependent, making use of the canonical wave functions/natural orbitals [11, 20, 148–152] and their corresponding canonical occupation probabilities, which are determined entirely by the one-body density matrix and so are intrinsic properties of any many-fermion system, irrespective of the representation. The orbital entanglement entropy vanishes for the case of a single Slater determinant, and is the simplest measure of the complexity of a many-fermion wave function, and since it is defined in terms of the canonical occupation probabilities, it is a unique characterization. One can obtain even more detail by considering the entanglement spectrum, which we also illustrate here. We apply these characterizations of wave function complexity to the highly non-equilibrium process of nuclear fission within time-dependent density functional theory extended to include pairing correlations, known as the time-dependent superfluid local density approximation (TDSLDA), which can simultaneously describe long range and short range correlations between fermions. We find that the minimum number of Slater deter-

minants required to represent the complex many-body wave function required to describe the nuclear fission process is about 10^{500}, and that the fission simulation considered here is equivalent to a system of 2.3×10^{10} interacting quantum spin-1/2 particles, which is a very large system in which to study quantum entanglement.

B. Introduction

It only took two years after Schrödinger [153] published his eponymous equation in 1926 for the question to arise for how to represent the wave function for an interacting system of many particles. If one discretizes the problem on a grid of size $n_s \times n_s \times n_s$, the wave function for a system of N spinless particles would require $(n_s^3)^{N-1}$ complex numbers to specify, which can become a very large number, for example in the case of a heavy nucleus. The simplest solution to this problem for the many-fermion case was presented almost a century ago, which is to use a Slater determinant and the Hartree-Fock (HF) approximation [154–157]. In the presence of pairing correlations, one uses an extension of the HF approach, namely the Hartree-Fock-Bogoliubov (HFB) approximation [11, 20, 150–152], both of which are still numerically challenging even today in three dimensions and in the absence of any symmetry.

For fermions, the simplest possible MBWF is the Slater determinant, which represents a collection of independent fermions and is the form of the MBWF used in the HF approximation. When pairing correlations are present, one instead replaces the Slater determinant with a generalized Slater determinant, where the particle creation operators are replaced with Bogoliubov quasiparticle annihilation operators [11]. Although the nuclear interaction is both strong and short-range, many nuclear properties, both single-particle and collective, can be well described using mean field theories such as HF and HFB, as well as other approaches such as Landau-Migdal theory for Fermi liquids, shell model calculations, etc. In all these mean field approaches, one typically uses a rather small number of single particle orbitals. However, when pairing correlations are present, the Fermi surface is diffuse, meaning that single particle states with rather high energy are populated with non-negligible occupation probability, so a larger number of SPWFs are required to accurately describe nuclear masses and low energy excitations. In many applications, one typically uses about twice as many SPWFs as the system particle number [11, 100].

For many years in nuclear physics, rather low momentum cutoffs have been used in

the treatment of systems with pairing correlations, meaning that the number of SPWFs included in the calculations is rather small, and the effects of the correlations are often incorporated into primarily phenomenological low energy interactions, with varying degrees of success. The argument justifying this approach is that the energy converges rapidly as a function of the momentum cutoff in a variational approach; however, as Anderson [158] remarked in the case of many-electron systems, "you may get pretty good energetics out of a qualitatively wrong state." For example, in the case of a superconductor, the contribution to the ground state energy from the condensation energy is very small, and so the system energy can calculated with reasonable accuracy without accounting for pairing correlations at all; however, of course, the proper correlated MBWF leads to other qualitative changes in the physics which would otherwise be completely missed.

Slater determinants form a complete basis for N-fermion many-body wave functions. When one expands a MBWF in terms of Slater determinants, the number of terms in the expansion depends strongly on the size of the single-particle (SP) basis of wave functions one uses. For example, in the case of CI or shell model calculations [147], which enable one to calculate the ground state and a few excited states only, in the absence of symmetry restrictions, the dimensionality of the Hamiltonian is

$$\frac{N_{sp}!}{N!(N_{sp}-N)!} \approx \left(\frac{N_{sp}}{N}\right)^N \text{ typically} \ll (n_s^3)^{N-1}, \tag{44}$$

where N_{sp} is the number of SPWFs employed in the calculation. Note that for a system of N particles, N_{sp} is the only adjustable parameter in Eq. (44). One can apply similar arguments when discussing the cases of other many-body techniques, such as coupled cluster approaches, the generator coordinate method, and certain implementations of the Quantum Monte Carlo method. However, given the strong dependence on N_{sp}, which in turn depends on the choice of single-particle basis, Eq. (44) does not constitute a unique definition of the complexity of the MBWF. For time-dependent calculations, it is known that dynamics in general are governed by statistical factors such as the number of available states for the system to evolve into. Thus, if one does not use a sufficiently large basis, the dynamics will become inaccurate, and on the flip side, performing calculations in too large of a space can become prohibitively expensive, as quantum many-body calculations already routinely push the world's largest supercomputers to their limits.

In this work we address the following questions.

- Does a useful measure of the complexity of a many-body wave function exist?
- Does a minimal set of N_{sp} single-particle wave functions exist, and what are the properties of those states? (This question already was answered in the affirmative decades ago [148, 149, 159–161].)
- How can one efficiently construct such a minimal single-particle basis?
- Having defined a proper measure of complexity, what new insight does it offer in the case of non-equilibrium processes, where local thermalization has not yet occured?

In the early 1950's, Levinger [162] described the nuclear photo effect by invoking the short range character of proton-neutron correlations and the quasi-deuteron model. More than 40 years later, it was demonstrated in several studies using realistic nucleon interactions that very high momentum SPWFs are occupied with significant probability [163, 164], a situation which would of course not occur if the nuclear MBWF was simply a Slater determinant. On the experimental side, just as in the case of Levinger's quasideuteron model, it was necessary to invoke short range correlations (SRCs), which manifest in significant occupation probabilities for high energy SP states, to explain the results of experiments on $(e, e'p)$ reactions [165, 166], as these results demonstrated that very low energy single-particle levels were occupied with an unexpectedly low probability, $n_{sp} \approx 0.6$ [164, 167]. Another theoretical approach which was popular for decades was that of Brueckner [168, 169], which also included the role of SRCs in a mean field theory treatment, although not explicitly so.

Despite the many successes of mean field theory, there are many observables which cannot be calculated accurately within a mean field approach, such as, for example, the single-fermion momentum distribution, which for both nuclear and cold atom systems has been intensively studied from both a theoretical and an experimental perspective [163–167, 170–186]. These results confirm the predictions made by S. Tan [187–189] that systems with zero-range interactions generically will exhibit occupation probabilities $n_k = C/k^4$ for single-particle states of momentum k, both in and out of equilibrium. In the case of nuclear systems, many studies have revealed that about 20% of the spectral strength is found for $k > k_F$.

C. Definition of The Canonical Basis

The complexity of the many-body wave function can be defined in a unique manner in terms of the canonical wave functions and the associated canonical occupation probabilities, which are the eigenfunctions and eigenvalues of the one-body number density matrix,

$$n(\xi,\zeta) = \langle\Phi|\psi^\dagger(\zeta)\psi(\xi)|\Phi\rangle, \tag{45}$$

where $\psi^\dagger(\xi)$ and $\psi(\xi)$ are the quantum field operators for the creation and annihilation of a particle with coordinate $\xi = (\boldsymbol{r},\sigma,\tau)$ (spatial, spin, and isospin coordinates) and $|\Phi\rangle$ is an arbitrary quantum many-body state, either static or time-dependent. The canonical basis is then given by

$$\int d\zeta\, n(\xi,\zeta)\phi_k(\zeta) = n_k\phi_k(\xi),\ 0 \le n_k \le 1, \tag{46}$$

$$\sum\!\!\!\!\!\!\int_\xi \phi_k^*(\xi)\phi_l(\xi) = \delta_{kl}, \tag{47}$$

$$N = \sum\!\!\!\!\!\!\int_k n_k, \tag{48}$$

where ϕ_k are the canonical wave functions and n_k are the canonical occupation probabilities. Having defined the canonical basis, one can then calculate the complexity for any many-fermion wave function $|\Phi\rangle$ by evaluating the orbital entanglement/quantum Boltzmann one-body entropy [46, 190–199]

$$\begin{aligned} S = &- g \sum\!\!\!\!\!\!\int_k n_k \ln n_k \\ &- g \sum\!\!\!\!\!\!\int_k [1-n_k]\ln[1-n_k], \end{aligned} \tag{49}$$

where g is the spin-isospin degeneracy, $\sum\!\!\!\!\!\!\int$ implies summation over discrete and integration over continuous variables respectively. The orbital entanglement entropy S can be thought of characterizing the degree of dissimilarity of the many-fermion wave function to a Slater determinant, for which $S = 0$. As interparticle interactions spread the single-particle strength over the entire spectrum, states will be populated with fractional occupation numbers, and so we will have $S > 0$, which is why S is a measure of the complexity of the MBWF, which is also a measure of the degree of entanglement of the system.

The canonical wave functions, which are the precisely the same wave functions as the natural orbitals and so we only use the former name here, were introduced in the 1950's

and 1960's by several authors for describing pairing correlations and superfluid fermionic systems [20, 148–151, 200, 201]. The canonical wave functions have been used extensively in chemistry [161] and lately also in nuclear physics [199, 202–214]. One can prove a very useful result about the canonical states, namely that if one wishes to express a many-fermion wave function as a superposition of Slater determinants, the canonical wave functions constitute the smallest set of single-particle orbitals in which to perform the expansion [148, 149, 159–161]. One can immediately see that this result will be crucial for defining a notion of complexity for the MBWF, since as we already established, one can dramatically alter the number of Slater determinants required to represent the MBWF by changing the single-particle basis, see Eq. (44).

From a mathematical perspective, it is obvious that the canonical wave functions form a complete orthonormal basis, but from what we can tell, a full investigation of the canonical wave functions has not yet been performed in the literature, as most authors restrict themselves to a reduced number of eigenvectors. As we will show here, it is valuable to consider the entire set of eigenfunctions, as they have distinctive (and sometimes peculiar) properties. The canonical wave functions essentially split into three categories, depending on the associated canonical occupation probabilities: (i) A subset with n_k close to 1, where the canonical wave functions behave like standard mean field SPWFs; (ii) a subset where $n_k \approx C/k^4$, where the SPWFs are localized within the nucleus but oscillate much faster than typical mean field wave functions; (iii) a subset with very small n_k, which are localized outside the system and are physically irrelevant, but mathematically required for the completeness of the set. The size of subset (i) is comparable with the particle number of the nucleus. Subset (ii) is perhaps an order of magnitude larger (or more, depending on the momentum cutoff), and has rarely been discussed in the literature. Subset (iii) is generally the largest set, as the number of linearly independent vectors is determined by the number of lattice points in the box.

D. The Canonical Basis for a Simple 1D System

We first demonstrate the properties of the canonical basis by considering a simple one-dimensional example, which nevertheless retains the qualitative features of a realistic three-dimensional system. We consider a system with a Woods-Saxon-like mean field potential

given by

$$V(x) = \frac{V_0}{1 + \frac{\cosh(x/a)}{\cosh(R/a)}} \tag{50}$$

and a pairing field given by

$$\Delta(x) = \frac{\Delta_0}{1 + \frac{\cosh(x/a)}{\cosh(R/a)}}, \tag{51}$$

where $-\infty < x < \infty$, $V_0 = -50$ MeV, $\Delta_0 = 3$ MeV, $R = r_0 A^{1/3} = 14.9$ fm, $a = 0.5$ fm, and $\mu = -5$ MeV. (Note that we have chosen this form rather than the standard Woods-Saxon form, as the standard form of the potential has a discontinuous first derivative at the origin, which leads to unphysical long momentum tails of the wave functions.) We then solve the static equations for density functional theory extended to superfluid systems, the superfluid local density approximation (SLDA), which are very similar to the Hartree-Fock-Bogoliubov (HFB) equations [31, 215], in a non-self-consistent manner, using the Discrete Variable Representation (DVR) method [216] for the numerical implementation. The equations of motion are

$$\begin{pmatrix} H - \mu & \Delta \\ \Delta & -H + \mu \end{pmatrix} \begin{pmatrix} \mathrm{u}_k \\ \mathrm{v}_k \end{pmatrix} = E_k \begin{pmatrix} \mathrm{u}_k \\ \mathrm{v}_k \end{pmatrix}. \tag{52}$$

We used a box of size $L = 80$ fm and with four different lattice constants $dx = 1, 0.5, 0.25, 0.125$ fm, and we used the mean field Hamiltonian

$$H = -\frac{\hbar^2}{2m}\frac{d^2}{dx^2} + V(x) \tag{53}$$

with no spin-orbit term. We note that the usual SLDA Hamiltonian is a 4×4 block matrix, whereas Eq. (52) is only 2×2. One can understand Eq. (52) as being the equation for the components $\mathrm{u}_k(x)$ with spin-up and $\mathrm{v}_k(x)$ with spin-down, and one can obtain the equations for $\mathrm{u}_k(x)$ with spin-down and $\mathrm{v}_k(x)$ with spin-up by changing the sign of the pairing field $\Delta(x) \to -\Delta(x)$ only [31, 215]. A nice aspect of the SLDA formalism is that the equations for nuclei and for cold fermionic atomic gases has the same structure in this case, and furthermore it is straightforward to extend these simulations to more complicated geometries, such as what one encounters in the nuclear pasta phase in the crusts of neutron stars or superconductor-normal-superconductor junctions in condensed matter physics. We note

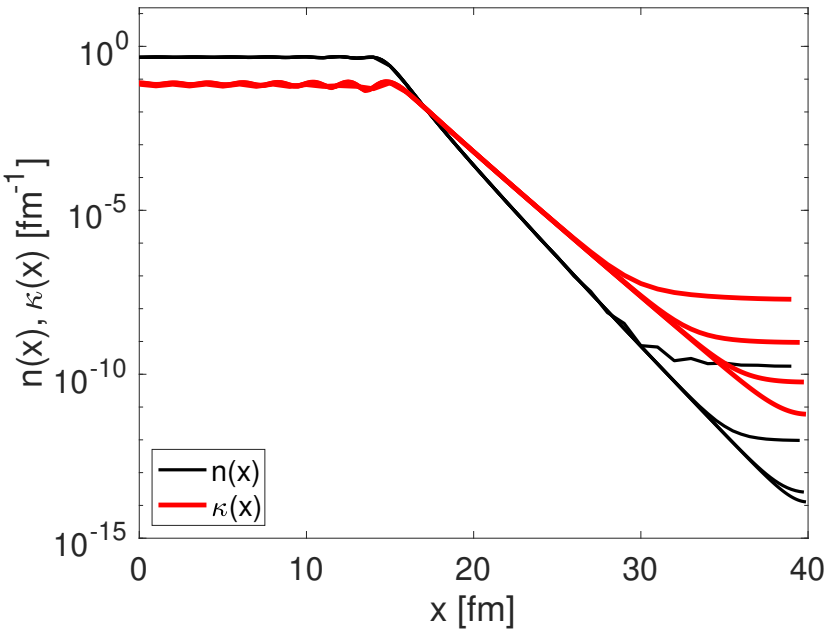

FIG. 18. Number density (black) and anomalous density (red) for the simple 1D model at various lattice spacings.

.

that the setup we consider here is equivalent to a normal-superconductor-normal junction. It is also straightforward to extend our analysis to infinite periodic systems.

We can connect this one-dimensional model to spherically symmetric three-dimensional systems with pairing correlations by considering only the spatially odd eigenstates, which are solutions to the radial Schrödinger equation with orbital angular momentum quantum number $l = 0$, in which case the full wave function in three dimensions is

$$\psi(\boldsymbol{r}) = \frac{\phi(r)}{r} Y_{lm}(\theta, \phi), \quad r = x \geq 0. \tag{54}$$

We now report the results of the solutions of these equations. Firstly, it was reported in [217] that the anomalous density $\kappa(x)$ has longer exponential tails than the number density $n(x)$, which becomes relevant particularly relevant as one approaches the neutron drip line. Indeed, we see this behavior in Fig. 18, even though it is not reflected in the spatial profiles of the potentials $V(x)$ and $\Delta(x)$, as we do not solve the SLDA equations self-consistently. Fig. 18 also shows the effect of considering smaller and smaller lattice spacings, which corresponds to choosing high values for the momentum cutoff; in this case, we see that high resolution means that we reproduce the number density and the anomalous

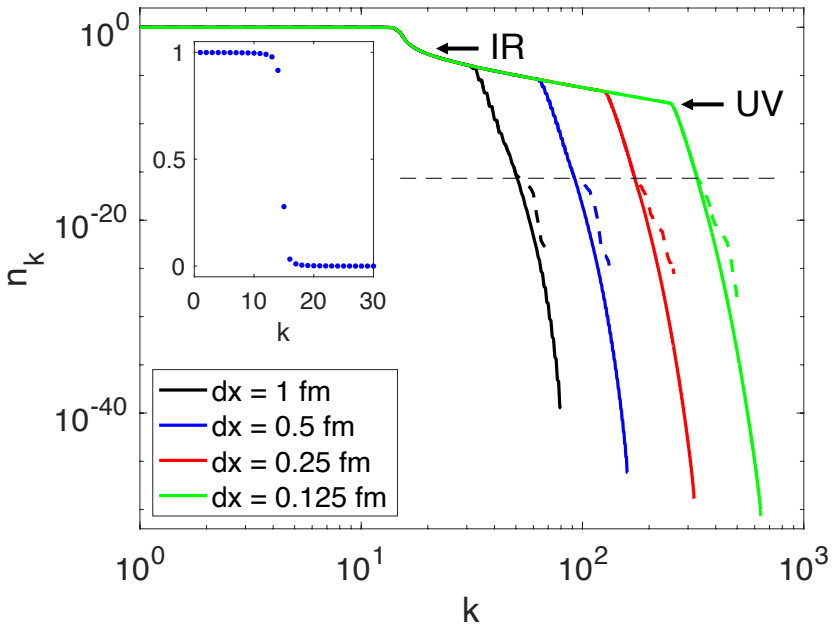

FIG. 19. The canonical occupation probabilities for four values of the lattice constant dx, which is equivalent to momentum cutoffs $\Lambda = \pi\hbar/dx$. We see clearly three regimes: a nearly constant regime, a power law regime $n_k \sim C/k^4$, and a rapidly decaying regime. Solid lines were calculated with extended numerical precision (40 digits, rather than the usual 16 for double precision floating point numbers) to accurately characterize the very small canonical occupation numbers. The inset shows the canonical numbers in linear scale close to the Fermi surface.

density (which is the superfluid order parameter) at larger distances.

We display the full distribution of canonical occupation numbers in Fig. 19. We see they clearly split into the three regimes mentioned in the introduction: (i) a nearly constant regime, (ii) a a power law regime $n_k \sim C/k^4$, and (iii) a rapidly decaying regime. As the momentum cutoff is increased, the power law regime extends to higher energies. The three regimes are separated by two "knees," which we call the infrared (IR) knee close to the Fermi level, where the behavior transitions from BCS-like behavior to the power law behavior, and the ultraviolet (UV) knee.

We plot a representative canonical wave function from each regime in Fig. 20. We see that below the IR knee, the canonical wave functions look like typical mean field wave functions. Between the IR and UV knees, in the power law regime, the orbitals are still localized

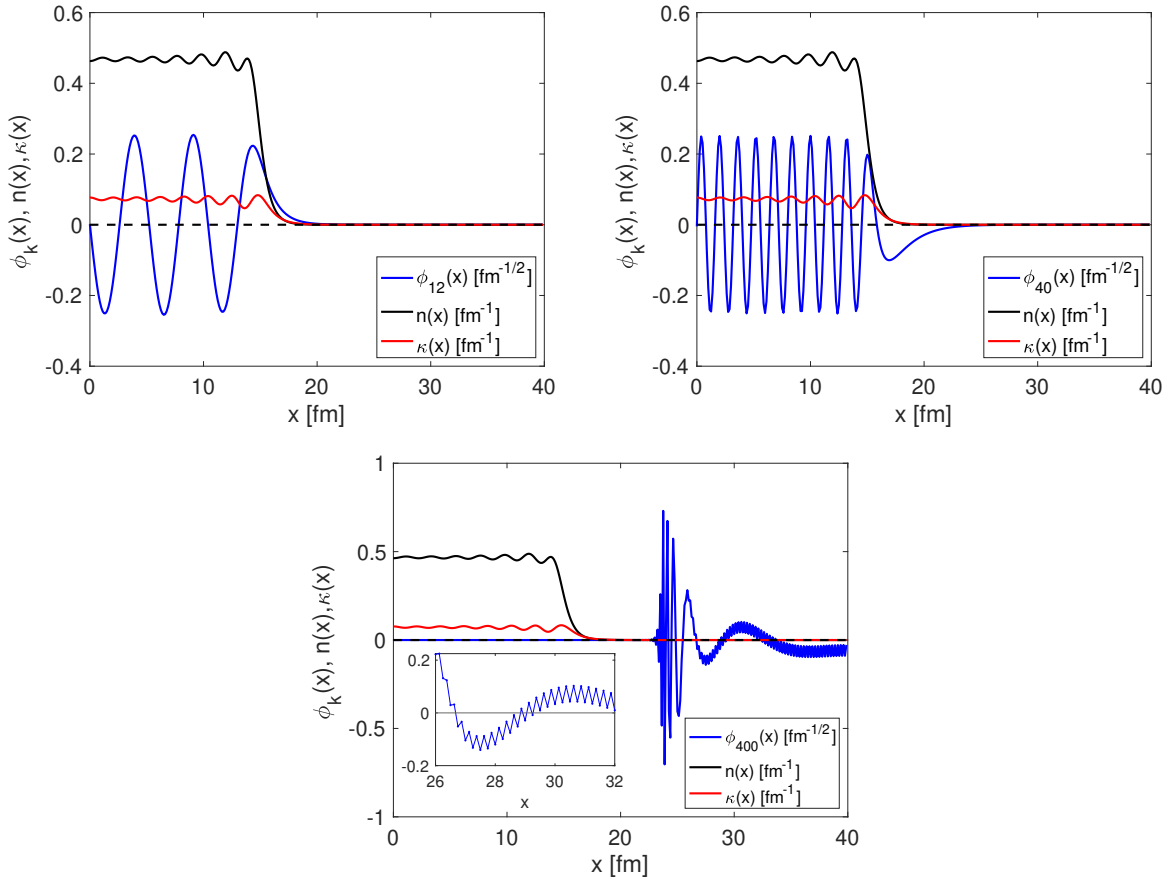

FIG. 20. Canonical from the three regimes. In the top left we show a canonical wave function from below the IR knee with $n_k = 0.978$. In the top right panel is a wave function from the power law regime between the two knees with $n_k = 1.3 \times 10^{-4}$. In the bottom panel we show a state from beyond the UV knee with $n_k = 2.6 \times 10^{-13}$. The number density is plotted in black and and anomalous density in red.

within the system; however, they exhibit much more rapid oscillations than is typical of a mean field SPWF. Finally, beyond the UV knee we see that the wave functions are localized outside the system, and take on a very strange spatial profile, which motivated us to use extended numerical precision to ensure their properties were characterized accurately. The inset for this exterior wave function shows high frequency spatial oscillations of wavelength $2dx$, meaning that these wave functions clearly cannot be solutions of a typical Schrödinger equation with a local potential. In the limit where the momentum cutoff $\Lambda = \pi\hbar/dx \to \infty$, these canonical wave functions will have no spatial derivatives, like the famous patholog-

ical Weierstrass function from mathematical analysis, which is continuous everywhere but differentiable nowhere. The appearance of these unusual wave functions is undoubtedly interesting, but they do not affect the physical properties of the system, and instead are only present to ensure the completeness of the canonical basis.

We see from Figs. 19 and 20 that, in addition to providing a basis-independent characterization of the complexity of the MBWF, the canonical basis also naturally provides its own cutoff on the number of single-particle states to include in the calculation, namely one should take all the states up to the UV knee, which occurs almost precisely at the momentum cutoff Λ, including all states in the power law regime which are localized inside the nucleus, and which is a number generally much larger than the number of single-particle orbitals one includes in typical mean field treatments of nuclei. The power law states were first predicted to exist in 1980 by Sartor and Mahaux [170] and recently put clearly in evidence experimentally in nuclei by Hen *et al.* [178], O. Hen et al. [185], and Cruz-Torres *et al.* [186]. Furthermore, they are not negligible when calculating observables. Consider for example the extremely simple case of the particle number,

$$\int_{\Lambda}^{\infty} dk k^2 n_k = \frac{C}{\Lambda}, \tag{55}$$

which evidently converges rather slowly as a function of the momentum cutoff. In previous studies in the literature focused on calculations of the nuclear binding energy, various cutoffs on the size of the canonical basis were considered, all with k smaller than the IR knee [199, 203–214], and so these authors missed the presence of the long momentum tails which we discuss here. In the case of static calculations, one can often obtain acceptable results with a reduced set of single particle states, for example by artificially adjusting the chemical potential to reproduce the desired particle number, although certain aspects of the solution will certainly be missing; however, as we will show below, in the case of dynamics, working in such reduced single-particle spaces is much more problematic and is likely to introduce serious errors.

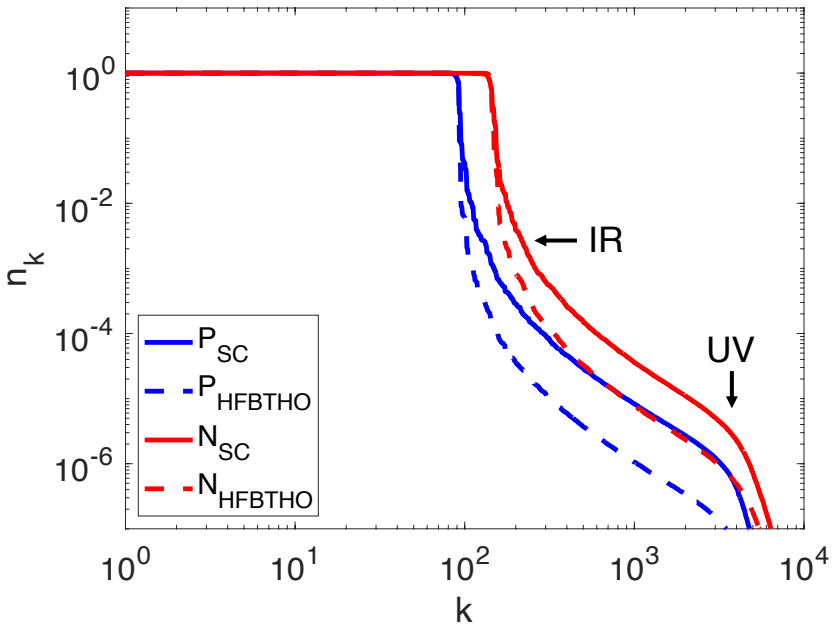

FIG. 21. The canonical occupation numbers for a three dimensional system, in this case the deformed ground state of a ^{236}U located along the outer saddle of the potential energy surface, a typical initial condition for TDSLDA simulations of neutron-induced nuclear fission from the outer saddle to scission and through to full separation of the fission fragments, calculated using two different methods. The two methods for calculating the ground state are to use a harmonic oscillator basis as in the HFBTHO code, and to calculate the ground state directly on a 3D spatial lattice. The latter case clearly manifests a higher many-body wave function complexity. The canonical occupation probabilities, up to a constant, define the entanglement spectrum $-\ln n_k$ [218]. Note that the same three regimes of canonical occupation numbers separated by the IR and UV knees appear for this realistic calculation as appear in the simplified 1D model.

E. The Canonical Basis for a Realistic Non-Equilibrium Process in a Many-Fermion System: Induced Nuclear Fission

We now apply the tools we have developed to a realistic strongly interacting system, induced nuclear fission with a low energy neutron. We simulate the evolution of this system from the outer saddle to full separation within TDSLDA, and we investigate the time-dependence of the MBWF during this process.

In order to perform such TDSLDA calculations, we first prepare the nucleus in a deformed

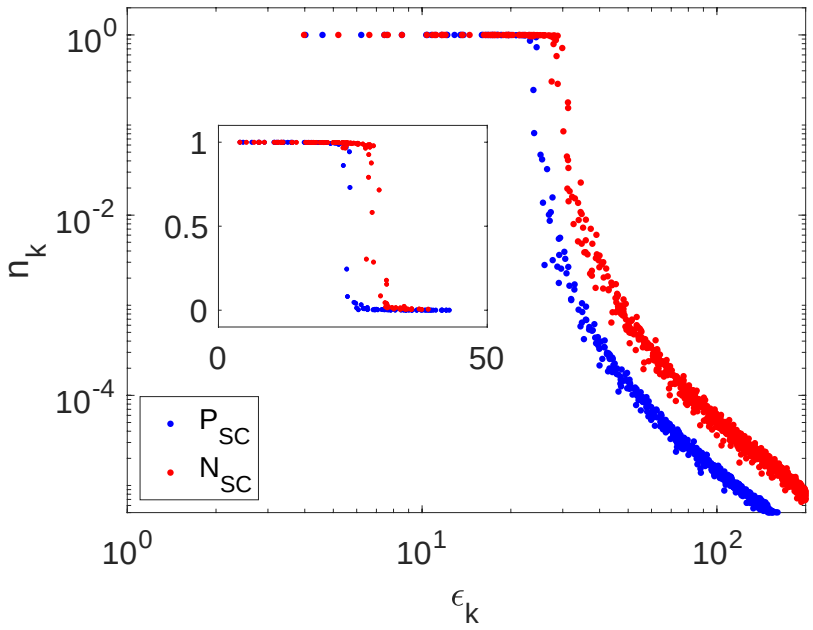

FIG. 22. The canonical occupation probabilities n_k as a function of the kinetic energy of the canonical wave functions ϵ_k. The inset shows the behavior in a linear scale around the Fermi level, which exhibits roughly the expected textbook behavior. We note that the ϵ_k are only approximately monotonic functions of k.

ground state somewhere along the outer saddle of its potential energy surface using the HFBTHO code [219, 220] which solves the self-consistent static SLDA equations using a small set of single-particle wave functions in a harmonic oscillator basis, and which is quite sufficient to estimate the total energy of a nucleus. However, we have found that the accuracy of the time-dependent simulations can be significantly improved if we subsequently place the deformed ground state wave functions on the 3D lattice and continue the self-consistent procedure [29–32, 112]. The canonical occupation numbers for the initial state in each case can be seen in Fig. 21. One plausible explanation for the improved accuracy when self-consistency is obtained on the full 3D lattice is that the wave function clearly manifests a higher degree of complexity on the lattice, as we can see in Fig. 21. We also plot the kinetic energy of that canonical wave functions

$$\epsilon_k = \left\langle \phi_k \left| -\frac{\hbar^2 \nabla^2}{2m} \right| \phi_k \right\rangle, \tag{56}$$

which between the IR and UV knees exhibit the expected behavior of $n_k \propto 1/\epsilon_k^2$, see Fig. 22.

One of the innovations of the SLDA formalism is that it is the first density functional

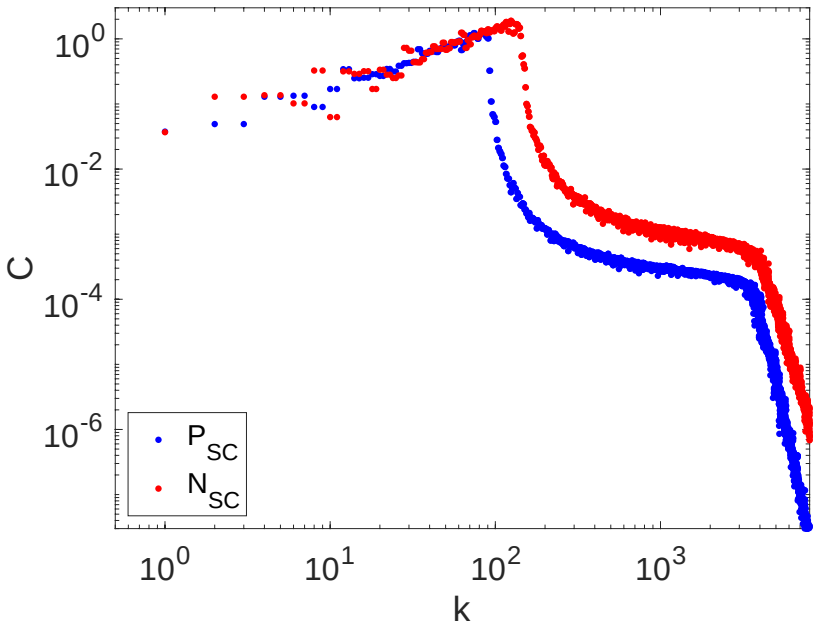

FIG. 23. The Tan contact, which is defined as $C = (2m\epsilon_k/\hbar^2)^2 n_k$ in the regime where $n_k \approx C/k^4$.

theory formalism which properly accounts for the required regularization and renormalization of the pairing field [22, 23] $\Delta(\xi)$, and it is known in systems with a local pairing field, the occupation probabilities should obey [170, 187–189]

$$(\epsilon_k)^2 n_k \approx \left(\frac{\hbar^2}{2m}\right)^2 C \quad \text{if} \quad k_{\rm IR} < k < k_{\rm UV}, \tag{57}$$

which we display in Fig. 23, and which demonstrates good agreement with these theoretical predictions. As we also argued above, the power law regime of the occupation probabilities terminates at the UV knee, whose location is determined by the momentum cutoff Λ. In realistic nuclear physics calculations, such as the ones we present here, a typical momentum cutoff is $\Lambda \approx 600$ MeV/c, which is related to the QCD chiral symmetry breaking scale Λ_χ, which is in turn controlled by the size of the nucleon, as it makes no sense to consider the interaction between two nucleons when their quark clouds strongly overlap.

It is informative for such realistic systems to characterize the convergence of various quantities of interest in the canonical basis, which we remind the reader is the most compact and economical basis of single particle wave functions in which to represent a many-fermion wave function as a sum of Slater determinants. In Fig. 24, we demonstrate the number of canonical wave functions in the canonical basis as a function of the cutoff imposed on the canonical occupation number. It is interesting that, even when we include states up to very

small occupation number, the number of single particle orbitals is still more than an order of magnitude smaller than the number of orthogonal SPWFs in the simulation volume, which is $2\times30^2\times60 = 108,000$. It is for this reason that one cannot simply use the number of single-particle orbitals as the definition of the complexity of the MBWF, because if we compare the number of Slater determinants we must use to reproduce the (particle-number-projected) MBWF from canonical wave functions, with a reasonable cutoff, to the total number of possible Slater determinants we could possibly construct in the box, we find that

$$\frac{N_{CWFs}!}{N!(N_{CWFs}-N)!} \ll \frac{N_{sp}!}{N!(N_{sp}-N)!}, \tag{58}$$

and so we see that the total size of the single-particle space, which depends on the choice of basis in which the SPWFs are represented, is generally a dramatic overestimate of the actual complexity of the many-body wave function. In Fig. 25, we plot the convergence of the particle number and entanglement entropy as a function of the cutoff on the canonical occupation number. We note that although one can reproduce observables with good accuracy using a relatively small basis of canonical wave functions at a given time, for dynamics we always require the full set of wave functions; we will explain this in more detail in the next chapter of this thesis.

However, the most interesting picture emerges for the case of dynamics, by which we mean the evolution of the nucleus from the outer saddle, through scission, to the full separation of the fission fragments. At each time, we can construct the canonical basis, and so we can look at the evolution of the orbital entanglement entropy, which we show in Fig. 26. Since nuclear fission is a typical nonequilibrium quantum process, one might expect the entropy would increase monotonically in time [46], but the actual behavior is more interesting. At all times, the canonical occupation number distribution looks like that of Fig 21, even though the phase coherence of the pairing field has been lost for times $>$ 700 fm/c, the role of the short range correlations is still always present, see also Refs. [46, 146]. But even though the canonical occupation number distribution always takes on the same profile, the evolution of the entropy is non-monotonic with time. There are two aspects of this non-monotonicity which must be discussed. Firstly, we see that for the HFBTHO initial conditions (red curves), the complexity of the many-body wave function rapidly increases at early times, until it matches that of the fully self-consistent initial conditions, which it then follows closely for the remainder of the simulation. As we mentioned earlier, this behavior can be understood

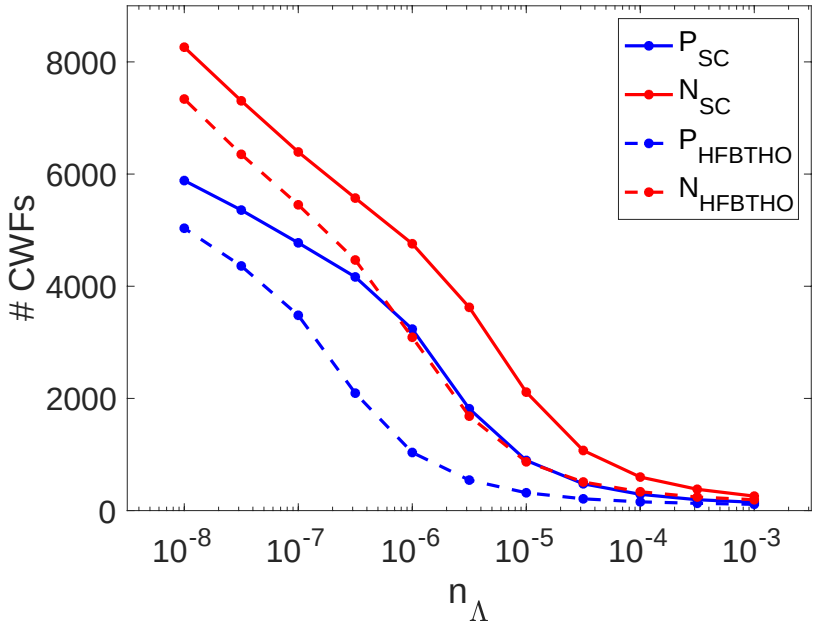

FIG. 24. The number of single particle wave functions in the canonical basis, for both protons and neutrons, for the initial state of the Uranium-236 nucleus constrained to lie on the outer saddle point of the potential energy surface, as a function of the cutoff imposed on the canonical occupation number. The most principled value of the cutoff is determined by the location of the UV knee, which for this system is to be found around $n_k \approx 10^{-6}$. The dashed lines refer to the HFBTHO solutions, and the solid lines correspond to the 3D self-consistent solutions obtained on the lattice.

by the substantially lower complexity of the HFBTHO MBWF, see Fig. 21, and so when the wave function prepared in the harmonic oscillator basis is placed within a much larger space, interactions rapidly spread the strength over that larger space. The second aspect of the nonmonotonicity which is of relevance concerns the behavior of the black curves, which correspond to the fully self consistent initial conditions prepared on the lattice. In this case, the entropy starts by decreasing monotonically until approximately the scission point. We can understand this because the neck progressively decreases in diameter during this descent to scission, thereby impeding any "communication" between the fragments, and the single particle wave functions are increasingly confined to a smaller region of space during this time, which in turn inhibits the spreading of the single-particle strength. Following scission, we see the orbital entanglement entropy increase once again, which can be explained because the fission fragments (FFs) emerge deformed and with significant excitation energy, between

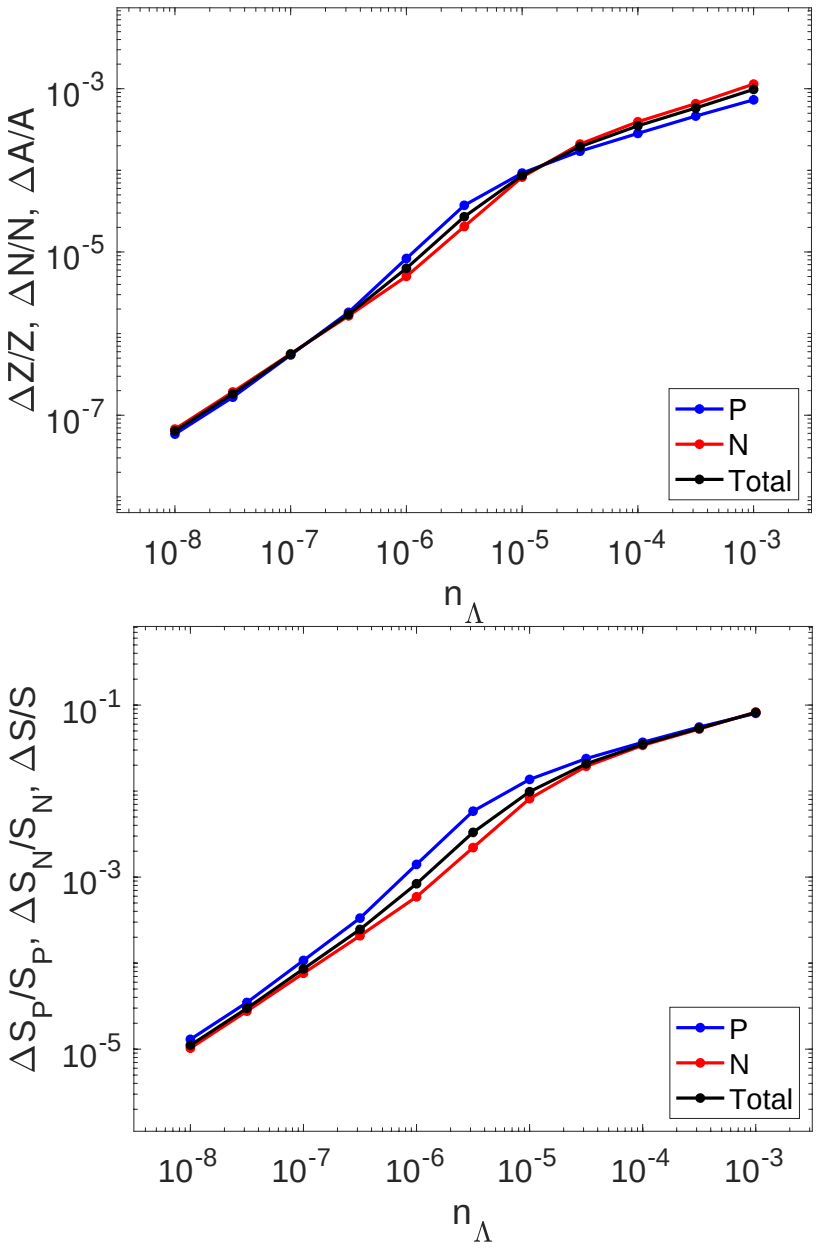

FIG. 25. Convergence of the particle number (top) and the orbital entanglement entropy (bottom) as a function of the cutoff on the canonical occupation number.

15 and 20 MeV each, and as time evolves the shapes of the fragments relax, converting deformation energy into intrinsic excitation energy. It is the fact that the fragments emerge from fission in such excited states that explains the behavior of the entropy $S(t)$ for times beyond roughly 700 fm/c.

For the same fission trajectory, we also show as a function of time the number of canon-

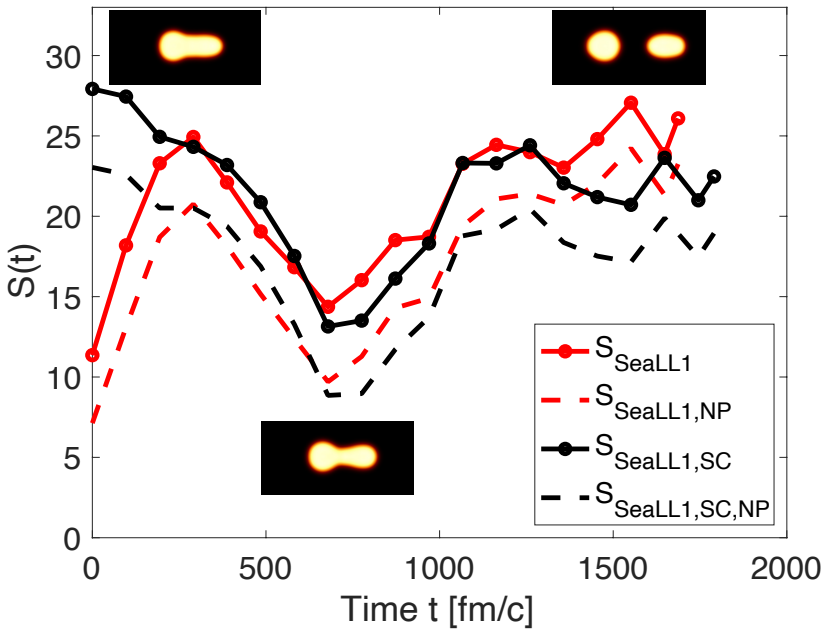

FIG. 26. The quantum Boltzmann one-body entropy evaluated as a function of time for a time-dependent calculation of the highly non-equilibrium process of nuclear fission, specifically the descent from the outer saddle point on the potential energy surface (leftmost frame) until full separation and the early stages of Coulomb acceleration of the fragments (rightmost frame). The solid curves correspond to the entropy evaluated without particle number projection, whereas the dashed curves are evaluated with particle number projection onto the system average particle number. The runs with initial conditions prepared with HFBTHO are shown in red, and the curves with full self-consistency obtained on the 3D lattice are shown in black. The profiles shown in the inset correspond to times 0, 675, and 1650 fm/c.

ical wave functions required describe the MBWF, see Fig. 27, which has, as expected, a nonmonotonic time dependence. And finally, we show the two contributions to the entropy from Eq. (49), see Fig. 28, which demonstrate that their contribution to the total entropy is essentially equal.

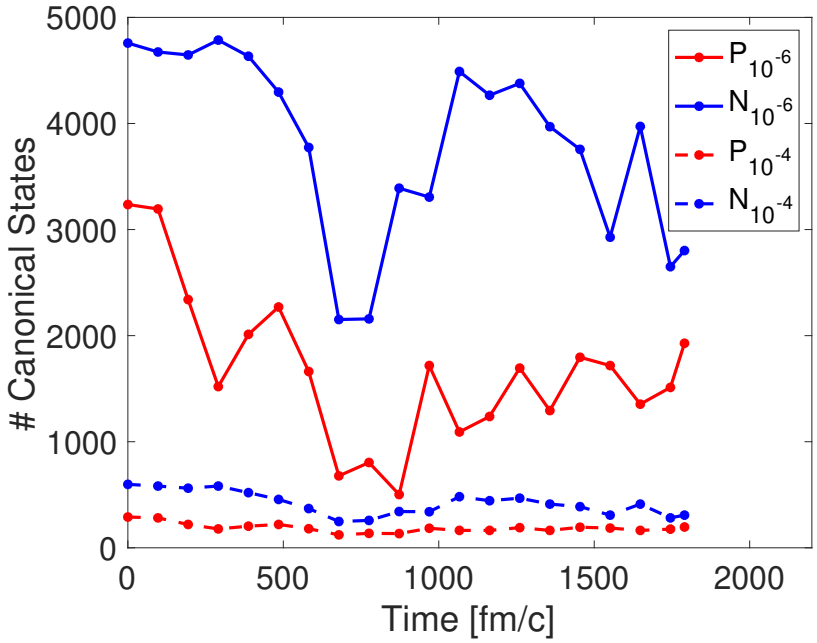

FIG. 27. Number of canonical states required to reproduce the MBWF as a function of time for fixed cutoffs $n_\Lambda = 10^{-4}, 10^{-6}$.

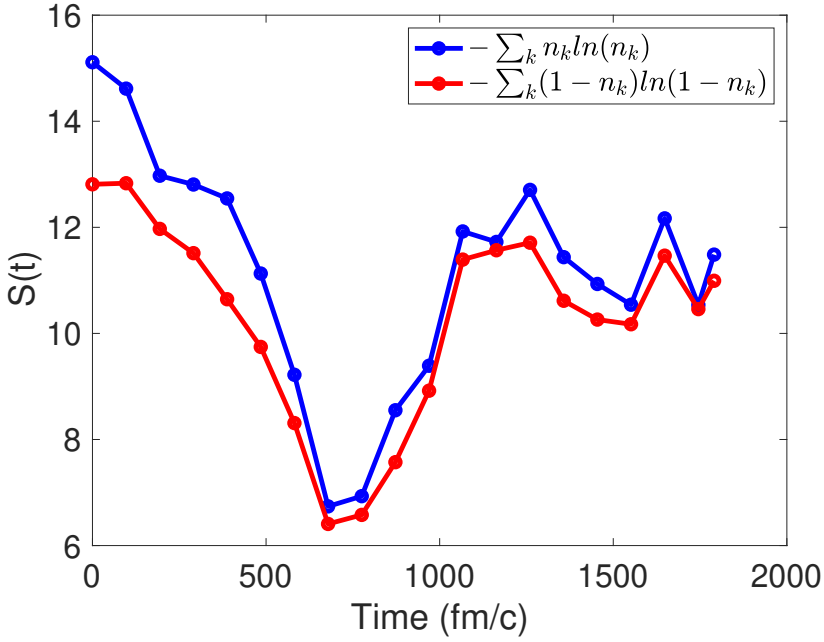

FIG. 28. The two components of the orbital entanglement entropy as a function of time during fission.

VIII. NON-MARKOVIAN CHARACTER AND IRREVERSIBILITY IN REAL-TIME QUANTUM MANY-BODY DYNAMICS

In this section, we review the results presented in the paper "Non-Markovian character and irreversibility of real-time quantum many-body dynamics" by A. Bulgac, M. Kafker, I. Abdurrahman, and I. Stetcu, Phys. Rev. C **109**, 064617 (2024) [7].

A. Abstract

The extension of time-dependent density functional theory to superfluid systems, known as the time-dependent superfluid local density approximation (TDSLDA), includes the effect of interparticle interactions through the presence of local pairing field, which is in practice equivalent to the inclusion of a collision integral in quantum kinetic equations. Simulation of the TDSLDA equations for a dynamic process, in this case, neutron-induced fission, reveals that the single-particle occupation probabilities exhibit a non-Markovian time dependence. This non-Markovian behavior is unexpected, as in the quantum Boltzmann equation, which is based on a collision integral involving phase space occupation probabilities, and which is the most-used approach for describing nuclear dynamics, has Markovian behavior by construction. The irreversibility of the dynamics of the quantum many-body system considered here is best characterized using the orbital entanglement entropy and the canonical basis, which were introduced in Sec. VII. To investigate the role of memory effects and irreversibility in the real-time dynamics of fermionic many-body systems, we employ the canonical basis and assess its utility for static and dynamic calculations, as well as for restoration of broken symmetries. Since the canonical basis is provably the most economical basis in which to represent a many-fermion wave function as a sum over Slater determinants, it is desirable to work in this basis whenever possible, and to use a cutoff on the canonical occupation number. We show that truncations of the canonical basis set can work for static calculations and for restoration of broken symmetries, but that the full set of canonical wave functions are mandatory for time-dependent calculations, otherwise the nuclear dynamics are significantly affected.

B. Introduction

We assess whether nuclear dynamics has a Markovian character or not, and we also investigate the related question, whether the dynamics of an isolated nucleus undergoing nuclear fission are irreversible, and if so, how to characterize the irrreversibility. The main tool for doing so will be the canonical basis introduced in Sec. VII. We will show that the canonical basis cannot be used to accelerate time dependent calculations, which is the case because the matter distribution evolves with time, and hence so too does the density matrix and its eigenvalues and eigenvectors. So the appealing notion, suggested by promising results presented in Sec. VII, that the parsimonious representation provided by the canonical basis might be used to accelerate dynamics, proves immediately false. Nevertheless, we show that the canonical basis is very useful for instantaneously representing the nucleus at any given time, and that it is therefore useful for static calculations and also for symmetry restoration in systems with pairing correlations. For the details of formalism of the canonical basis, the reader is directed to Sec. VII for a brief overview, but the more detailed treatments are to be found in the papers presented in this section and the previous section [7, 10].

C. Static Calculations of Initial Conditions

Just as in Sec. VII, we performed our fission simulations in a simulation box of size $30^2 \times 60$ fm^3, where initial conditions are first calculated in a harmonic oscillator basis using the HFBTHO code [219], and then subsequently the densities are placed on the full 3D spatial lattice and the static superfluid local density approximation (SLDA) equations were solved until full self-consistency is achieved [21]. All calculations in the study were performed using the SeaLL1 nuclear energy density functional [12]. In the harmonic oscillator basis, about 8,000 orbitals were used, whereas in the full 3D simulation box the number of orbitals is 108,000.

The ground state properties of the ^{236}U nucleus, evaluated at the outer saddle of the potential energy surface, obtained with self-consistent SLDA on the full 3D lattice are displayed in Table III, where the convergence is investigated as a function of the number of canonical wave functions used to represent the nuclear MBWF. We observe that, although the full set of SPWFs in our simulation volume is 108,000, the properties of the nucleus have

TABLE III. The properties of the initial state of ^{236}U, prepared on the outer saddle of the potential energy surface, obtained with self-consistent SLDA on the full 3D lattice, as a function of the number of canonical wave functions included in the calculation, where we take the canonical wave functions with the highest occupation probabilities when performing the cutoff. The static calculations are performed using the full set of quasiparticle wave functions, and then we diagonalize the one-body density matrix to obtain the canonical basis. The quantities presented in this table are then reevaluated using the truncated basis of canonical wave functions. The last two rows show the results of using the full set of quasiparticle wave functions in the standard Bogoliubov quasiparticle basis and the canonical basis. Note that this state was in fact excited by a 1.17 MeV boost in the collective quadrupole mode, so the deformed ground state is actually more deeply bound by this amount.

No. States	Energy	N	Z	Q_{20}	Q_{30}
500	-1779.19	143.94	91.99	169.73	22.29
1 000	-1780.64	143.97	92.00	169.76	22.29
2 000	-1782.64	143.99	92.00	169.78	22.29
5 000	-1785.31	144.01	92.00	169.79	22.30
50 000	-1785.41	144.01	92.00	169.79	22.30
108 000 (Canonical)	-1785.41	144.01	92.00	169.79	22.30
108 000 (Standard)	-1785.41	144.01	92.00	169.79	22.30

essentially converged when we include only 5,000 canonical wave functions, which reveals that the canonical wave functions can indeed be used as a powerful tool for accelerating (deformed) nuclear ground state calculations. Another relevant result pertaining to this table is that the ground state energy obtained within HFBTHO is -1,780.72 MeV, which differs significantly from the energy reported in the table, -1785.41 MeV. And since we included an additional quadrupole boost of 1.17 MeV in the numbers reported in the table, we see that the SLDA deformed ground state is almost 6 MeV more deeply bound than the HFBTHO ground state, and Table III reveals that this state can be achieved actually using fewer orbitals than the harmonic oscillator calculation used. In light of these results, it is notable to consider the results presented in Chen *et al.* [210], namely that the fission isomer

of ^{240}Pu was evaluated with fewer than 500 canonical states; based on what we present in Table III, in which we remind the reader that the calculation was performed in the absence of any cutoff, and then we subsequently transformed to the canonical basis and evaluated the convergence as a function of the cutoff, it seems likely to us that the results of the Chen *et al.* [210] calculations may be somewhat inaccurate due to these authors not including enough canonical wave functions. Furthermore, we note the much greater implementation complexity of their calculation procedure, which requires introducing a large number of Lagrange multipliers which must be evaluated at each iteration when solving the HFB equations. The approach we advocate here, namely self consistently solving the HFB/SLDA equations and then performing a single diagonalization to transform to the canonical basis, is comparatively simpler, even though in practice the matrices become quite large.

TABLE IV. The final state properties for the time-dependent fission simulation using the initial conditions presented in Table III. The simulation is performed with the full set of wave functions, starting from an initial condition prepared in the canonical basis. We then apply a cutoff on the final state based on the *initial* (canonical) occupation probability. We apply a cutoff in this way because directly applying a cutoff on the initial state will cause the nucleus not to fission in the first place, see discussion in main text.

No. States	Z_i	Z_f	ΔZ	N_i	N_f	ΔN
500	91.99	91.87	0.12	143.94	141.74	2.20
1 000	92.00	91.89	0.11	143.97	141.86	2.11
2 000	92.00	91.90	0.11	143.99	141.95	2.04
5 000	92.00	91.91	0.09	144.01	142.11	1.90
50 000	92.00	92.00	0.01	144.01	143.48	0.52
108 000	92.00	92.00	1.0×10^{-6}	144.01	144.01	2.9×10^{-5}

D. Time-Dependent Calculations

The situation is quite different for the case of dynamics, however, which is illustrated by the results in Tables IV and V. In this case, we prepared several nuclei in deformed

TABLE V. Same as Table IV, except with initial deformation Q_{20} = 140.02 b and Q_{30} = 14.63 $b^{3/2}$.

No. States	Z_i	Z_f	ΔZ	N_i	N_f	ΔN
500	91.97	91.61	0.36	143.96	139.74	4.21
1 000	91.98	91.64	0.34	144.00	139.92	4.07
2 000	91.99	91.66	0.33	144.02	140.06	3.96
5 000	91.99	91.69	0.30	144.03	140.33	3.70
50 000	91.99	91.97	0.017	144.03	143.23	0.80
108 000	91.99	91.99	6.5×10^{-6}	144.03	144.03	1.1×10^{-4}

initial states of ^{236}U along the outer saddle of the potential energy surface, transformed to the canonical basis, and performed a TDSLDA simulation until full fission fragment (FF) separation without applying any cutoff on the single-particle wave functions. Since the initial (canonical) occupation probabilities are sorted in decreasing order, we can apply a cutoff on the final states based on the initial values of the occupation numbers. As we will show below, we look at the cutoff using this approach because if we tried applying a cutoff directly in the initial state, the nucleus would not fission in the first place. The result of applying this cutoff procedure in Tables IV and V is that the final state properties are dramatically modified, with in particular the neutron channel missing as many as four particles using this restricted set of single-particle states! This tells us that significant redistribution of the single-particle occupation numbers must occur during dynamics, which occurs as a result of the pairing interaction, which TDSLDA accurately incorporates through the inclusion of a self-consistent pairing field [15, 16, 19, 30, 31, 105, 106, 221, 222] .

Fig. 29 shows the dramatic redistribution of the single-particle occupation numbers during a fission calculation. The initial state is prepared in the canonical basis without a cutoff, and the final occupation numbers are evaluated in the standard Bogoliubov basis so that a direct comparison can be made. As we mentioned previously, see also [46, 146, 222, 223], even if one starts with a set of canonical wave functions, at the next time-step the matter distribution will have changed, and these wave functions will no longer be eigenstates of the instantaneous one-body density matrix, and so the canonical basis cannot be directly used for dynamics. Nevertheless, it is straightforward to follow the occupation numbers in

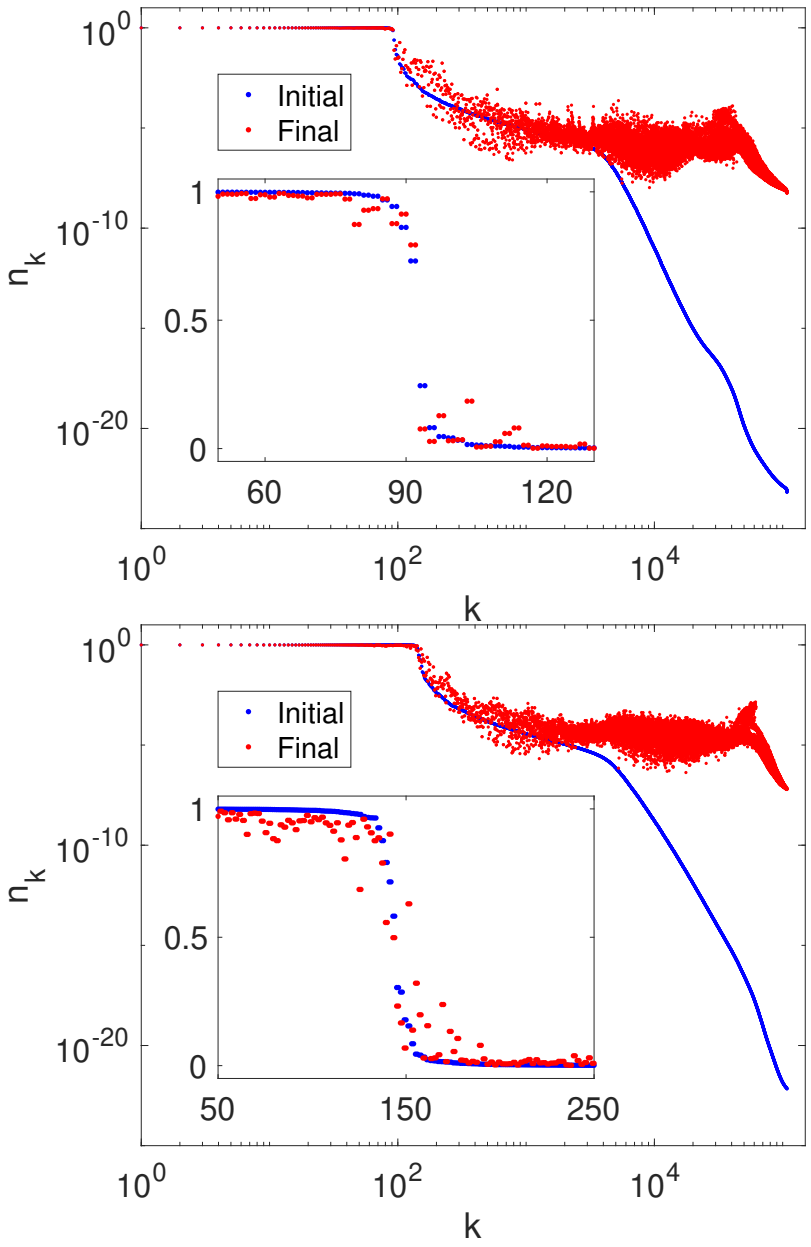

FIG. 29. The redistribution of the proton (top) and neutron (bottom) occupation numbers in the standard Bogoliubov basis as a result of a TDSLDA simulation of the ^{235}U(n,f) reaction from the outer saddle until the full separation of the fission fragments, using the initial conditions in Table V. The initial state is prepared in the canonical basis, but at all subsequent times the occupation probabilities are evaluated in the Bogoliubov basis, and only half the occupation probabilities are shown because they are double degenerate.

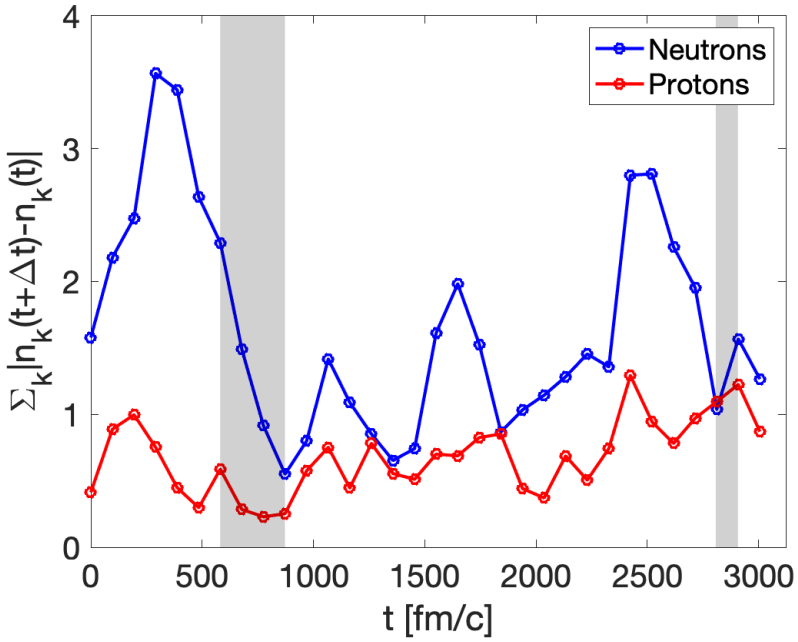

FIG. 30. Total absolute difference of occupation numbers between adjacent time intervals of duration $\Delta t = 97$ fm/c. The left gray band indicates the time during which the neck is formed, and the right gray band indicates the point of scission.

time, which can be calculated using $n_k(t) = \oint d\xi |\mathrm{v}_k(\xi, t)|^2$, obtained from the time evolved v_k-components of the Bogoliubov quasiparticle wave functions.

The total extent to which the single particle occupation probabilities evolve with time can be seen in Figs. 30 and 31. In Fig. 30, the absolute difference between the canonical occupation numbers is evaluated between adjacent times at an interval of $\Delta t = 97$ fm/c, whereas in Fig 31, the total absolute difference is evaluated in time relative to the initial state. Similar results were reported in [46], but with a smaller $\Delta t = 37$ fm/c, and where the initial conditions were not obtained self-consistently on the lattice, an omission which is known to affect the dynamics, see for example Fig. 26. The fact that the occupation probabilities continue to evolve in time, even after the nuclear neck has ruptured and the fragments have fully separated, provides a direct confirmation of the mechanism initially envisioned by Bertsch [15–19, 46] that the nuclear shape evolves during fission via redistribution of the single-particle occupation probabilities mediated by the pairing interaction.

Note however that the mechanism Bertsch proposed implies that the occupation prob-

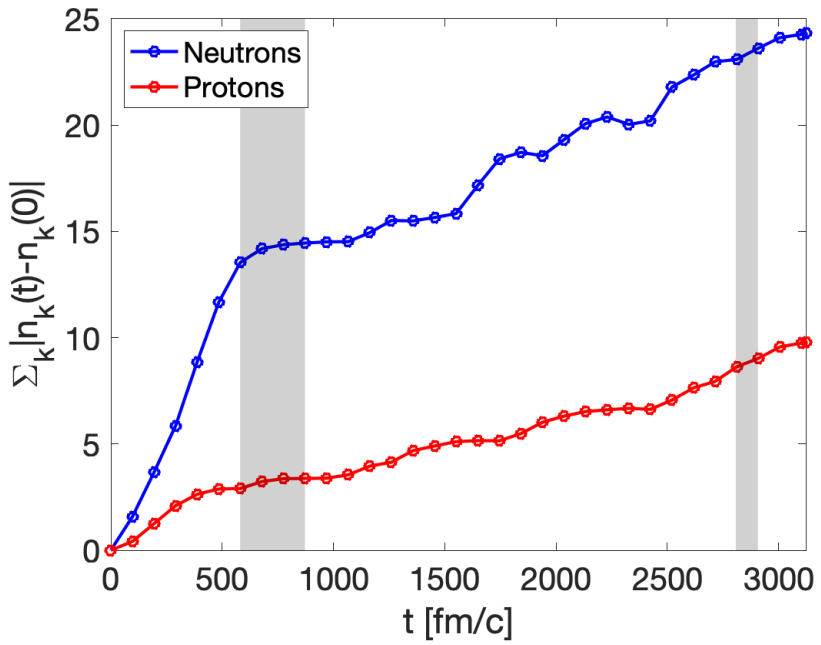

FIG. 31. Total absolute difference of occupation numbers compared to the initial state. The left gray band indicates the time during which the neck is formed, and the right gray band indicates the scission. Two linear regimes are clearly visible, which is in interesting contrast to a $\sqrt{t}$ evolution characteristic of a random process.

abilities change through independent and uncorrelated transitions at single-particle levels crossings [15–19]. However, the situation revealed by Fig. 31 is in fact more complex and interesting. If the redistribution of occupation numbers was in fact a random process (subject of course to total particle number conservation $\sum_k n_k(t) = N$) one might expect, as in the case of Brownian motion, that

$$\sigma_2(t) = \sqrt{\sum_k (n_k(t) - n_k(0))^2} \propto \sqrt{t}, \tag{59}$$

whereas at large times, the closely related quantity $\sigma_1(t)$ illustrated in Fig. 31

$$\sigma_1(t) = \sum_k |n_k(t) - n_k(0)| \propto t, \tag{60}$$

which we might call a "ballistic" evolution of the single particle occupation probabilities, which is a patently non-stochastic and therefore non-Markovian behavior. We thus conclude that the jumps between levels of time-reversed pairs of single-particle states at single-particle level crossings are in fact highly correlated in time, which is a qualitatively new aspect of

fission dynamics which has never been reported in the literature before. This feature of non-equilibrium quantum dynamics is particularly interesting in light of previous results reported on the problem of fission [29–31] which point clearly to the fact that the descent of the nucleus from saddle to scission is also a highly dissipative process, in which case one might have expected the stochasticity of the dynamics to be a crucial aspect. This is the case in classical dynamics, as well as a number of phenomenological fission models, where strong dissipation is modeled using a Langevin force [36, 49, 50, 52, 59, 60, 132, 224–229]. The fact that fission is simultaneously a non-Markovian process, where therefore memory effects are important, and also a highly dissipative process, is a qualitatively new aspect of non-equilibrium quantum dynamics and has never been discussed in the literature prior to the publication of this paper, as far as we can tell.

The evolution of $\sigma_1(t)$ is nearly always linear in t during our simulations, but the slope appears to have two regimes, first a period of fast linear growth, followed by a period of slow linear growth. This behavior seems to be explained by four contributions. Firstly, with time, as the internal excitation energy of the nucleus increases, the strength of the pairing correlations and the absolute magnitude of the pairing field decreases, although it remains nonzero even at late times, when the nuclear temperature significantly exceeds the temperature at which a pairing condensate should be present, see Fig. 32 and [29–31]. Secondly, around the time of the first gray bar is when the neck first begins to form. Prior to this point, an initial state was prepared by calculating the nuclear ground state in an external potential which forces the nucleus to exhibit a given shape. At the start of dynamics, this potential is instantaneously removed, which leads to transient effects, which mostly disappear by the time the neck has formed. Thirdly, as the neck continues to elongate and its thickness decreases, the flow of matter and energy between the fragments is increasingly inhibited, which likely sets the rate of "equilibration" shown between the two gray bands in Fig. 31. Fourthly, after the neck ruptures, the fission fragments emerge deformed, but as they are accelerated apart, that deformation relaxes, converting deformation energy into internal excitation energy and therefore populating higher energy single particle states within the fragments, which explains why the slope remains linear even after scission.

As was mentioned above, applying a cutoff to the initial state, even in the canonical basis, leads to the nucleus failing to fission, which is demonstrated in Fig. 33. Even with nearly half the states in the space, the nucleus does not fission at all, but rather remains deformed

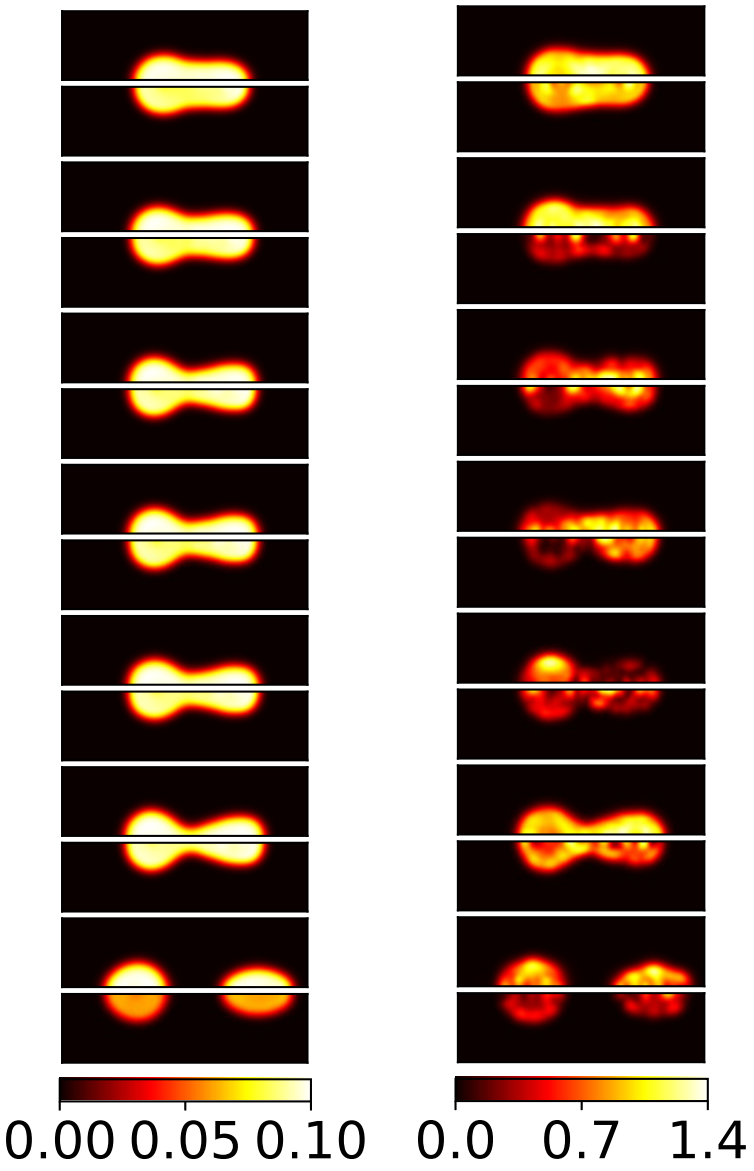

FIG. 32. Time evolution of the number density (left) and magnitude of pairing field (right). Each frame is divided into neutrons (top) and protons (bottom). Left colorbar in units of fm^{-3} and right in units of MeV.

and simply heats up, totally violating energy conservation. Hence, applying any cutoff on the number of single particle states included for dynamics is entirely unacceptable, and the full set must be used. This is likely the reason why, in past TDSLDA simulations, using a spherical cutoff for pairing was sufficient for static calculations, but caused problems in the case of dynamics [22, 23, 29]. The fact that the full set of states must be used for dynamics in TDSLDA necessarily casts some doubt on the reliability of any time dependent approach

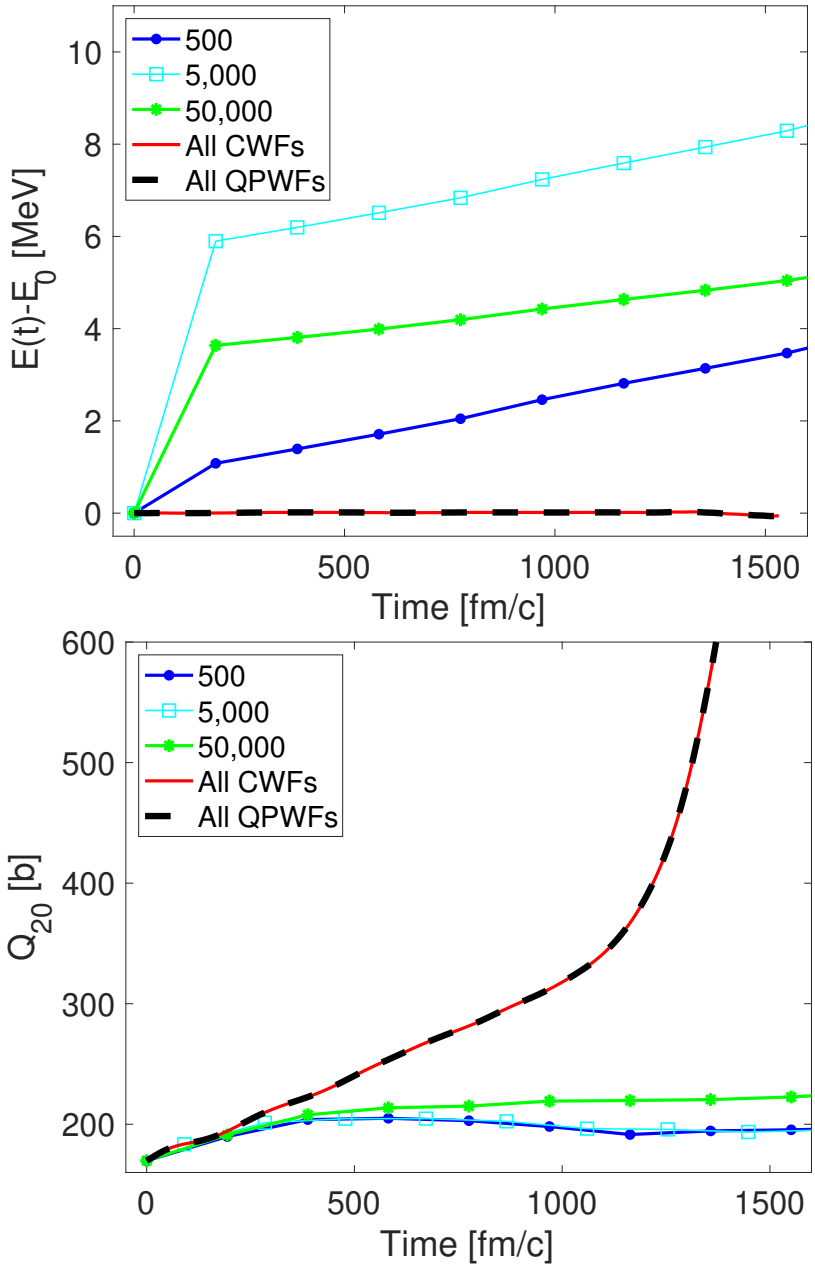

FIG. 33. The time dependence of the energy conservation and the nuclear quadrupole moment when a cutoff is applied to the number of SPWFs included in the dynamical calculation. The initial condition is prepared in the canonical basis, and the cutoffs refer to using only a certain subset of the canonical wave functions with the highest occupation probabilities. Notice that, unless all single particle states are included, energy is not conserved and the nucleus does not fission. Starting dynamics from the standard Bogoliubov basis or the canonical basis, on the other hand, does not make a difference to the evolution.

which incorporates pairing correlations but operates in a reduced space of single-particle states, for example the time-dependent BCS approximation [35, 230–237], which was also demonstrated more than 10 years ago to violate the continuity equation [237] and so cannot be trusted to accurately capture nuclear shape dynamics.

Another aspect of the non-equilibrium dynamics of many-fermion systems which can be illustrated by using the canonical basis is the irreversibility of the dynamical evolution. We investigate the question of irreversibility starting from the outer saddle point until the fragments have fully separated, prior to the emission of neutrons, gammas, or other particles. The simplest tool to characterize the irreversibility of the quantum dynamics is the orbital entanglement entropy [238–240], see Eq. (49), which we also used in Sec. VII to characterize the complexity of the many-body wave function. At all times during the time-dependent fission simulation, we can instantaneously transform to the canonical basis, whereupon the canonical occupation number distribution assumes the universal three-regime form presented in Sec. VII, see Fig. 34. From the canonical occupation numbers, we can evaluate the orbital entanglement entropy as a function of time, which we show in Fig. 35. Evidently, at different stages during the saddle to scission evolution, the nuclear many-body wave function is characterized by significantly different complexities, and the time dependence is not monotonic. Similar behavior of the entanglement entropy is observed in the dynamical evolution of other simpler strongly interacting fermionic systems [241–248].

E. Projection

In this paper [7], a number of new formulas were introduced for projecting the various densities on a fixed value of the particle number, which the reader will remember is necessary in the case of HFB-like calculations, where the many-body wave function is a superposition of states with different particle numbers. We present the results of these projection formulas here.

Ideally, the behavior of number density without particle projection should behave very similarly to the behavior of the density when we have projected on the average particle number of the system, which can be simply characterized as a function of time according to

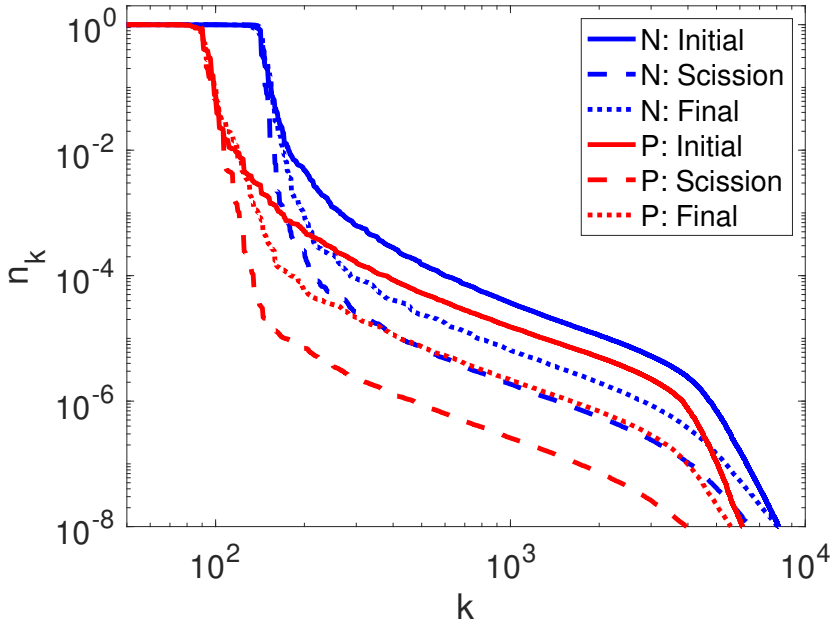

FIG. 34. The canonical occupation numbers at various times during a time-dependent fission simulation. In particular, the spectrum was evaluated in the initial state, at scission, and at the final state where the fission fragments are fully separated. Note that the Fermi surface is sharpest around the point of scission and is most diffuse for the initial state.

the formula

$$\Delta N_{N,Z}(t) = \sqrt{\sum_{\xi}(n(\xi,\xi,t) - \tilde{n}(\xi,\xi,t|N))^2}, \tag{61}$$

which we plot in Fig. 36. We see that these densities on average behave in a similar manner at all stages of the saddle to scission dynamics. We can investigate the differences between the projected and unprojected densities in more detail by plotting various slices through the difference between the unprojected and projected densities in the initial state, see Fig. 37, at scission, see Fig. 38, and in the final state, see Fig. 39.

Finally, it is also straightforward to evaluate the particle number distribution for the many-body wave function, which we show in Fig. 40. In each case, a slight left-right asymmetry about the average is observed. We note that for all the projections we performed in this study, both for the projection of the densities on to fixed particle number, or the calculation of the system particle number distribution itself, a reduced set of 5000 canonical wave functions is sufficient.

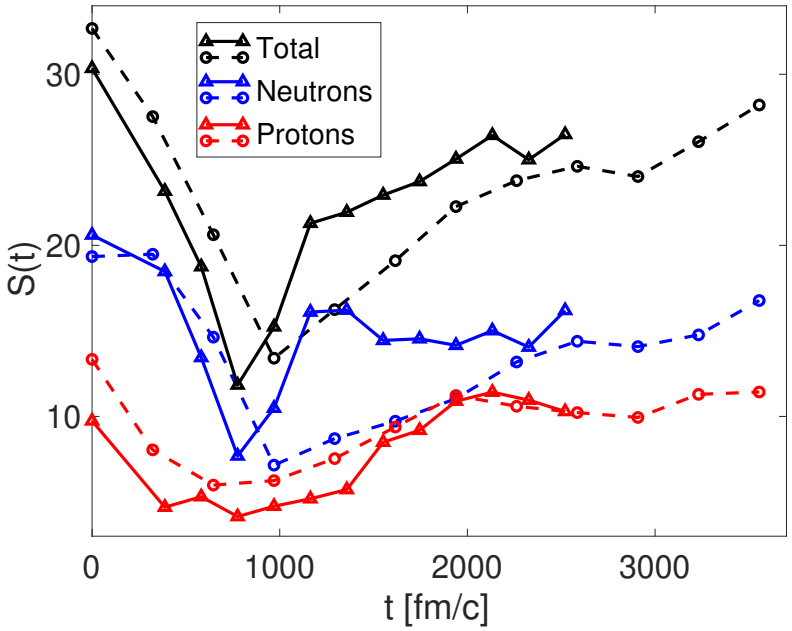

FIG. 35. The orbital entanglement entropy as a function of time for the reaction ^{235}U(n,f) in very large simulation volumes $48^2 \times 120$ fm^3 with lattice constant $l = 1$ fm for two different initial deformations, $Q_{20} = 159.64$ b and $Q_{30} = 17.80$ b$^{3/2}$ for one trajectory (solid lines) and $Q_{20} = 135.25$ b and $Q_{30} = 12.44$ b$^{3/2}$ for the other trajectory (dashed lines), prepared on the outer saddle of the potential energy surface. These simulation data were also used in the study in Ref. [6], see Sec. IV, where one can also find a description of the immense numerical calculations required to perform these simulations. For both trajectories, scission occurs around 1000 fm/c.

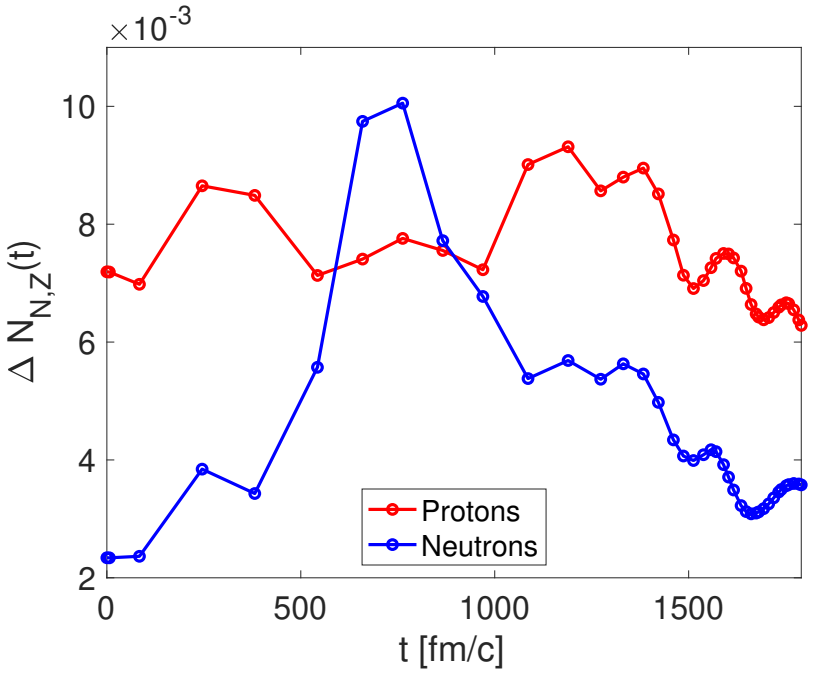

FIG. 36. Difference between projected and unprojected number density as a function of time, averaged over space, see Eq. (61).

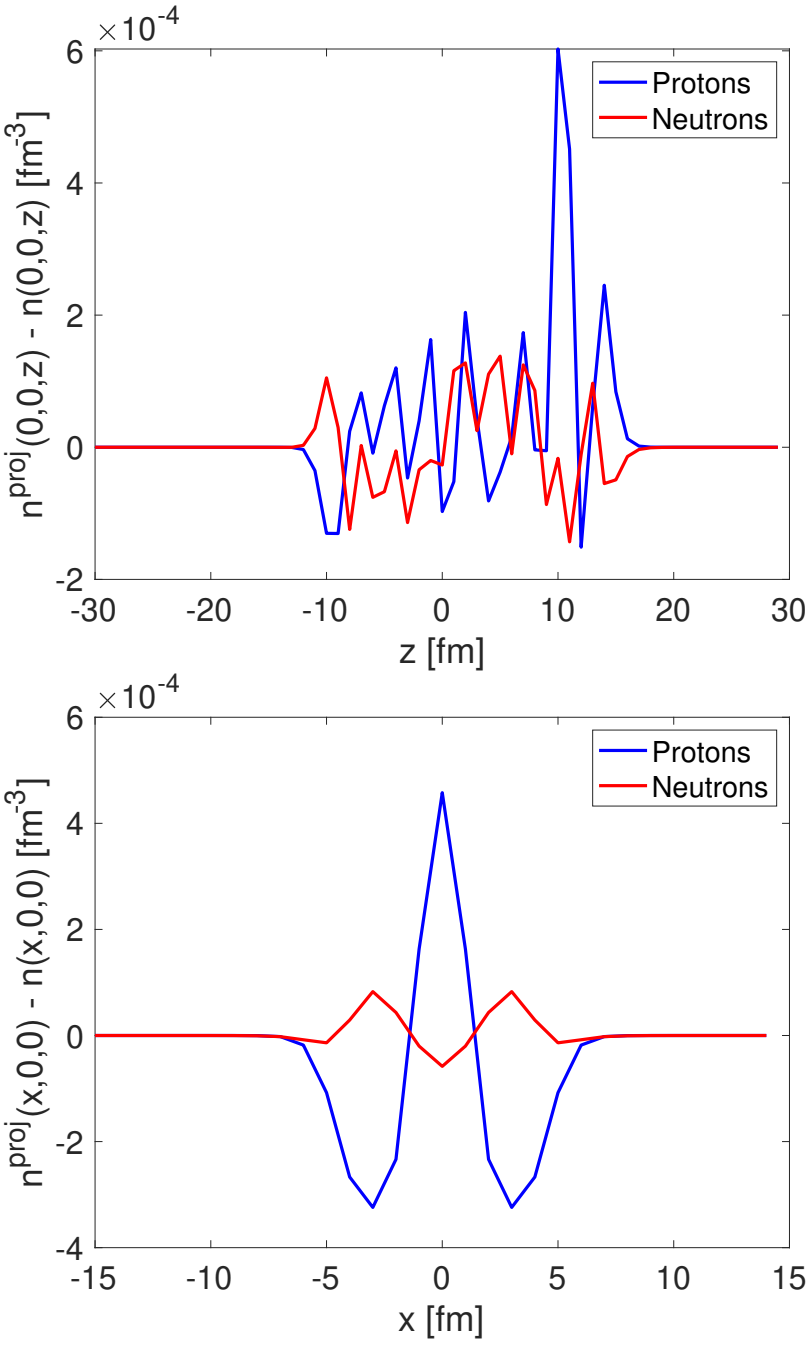

FIG. 37. Differences between unprojected and particle number projected number densities at the top of the outer barrier for ^{236}U for slices along the z and x axes.

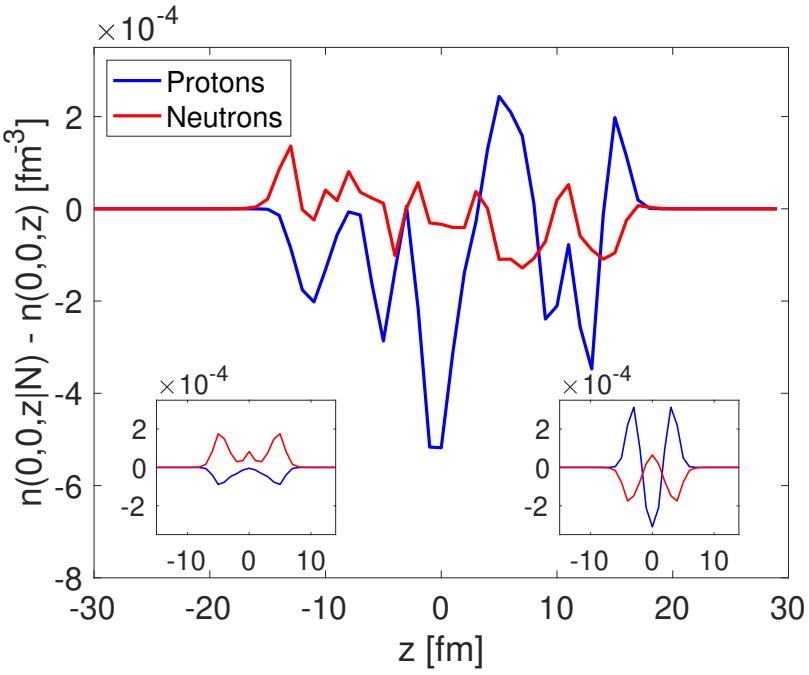

FIG. 38. Differences between unprojected and particle number projected number densities at the scission configuration, for the entire system along the fission direction z-axis and along the x-axis and at $y = 0$ in the insets, centered at the heavy on the left and at the light on the right fission fragments respectively at scission.

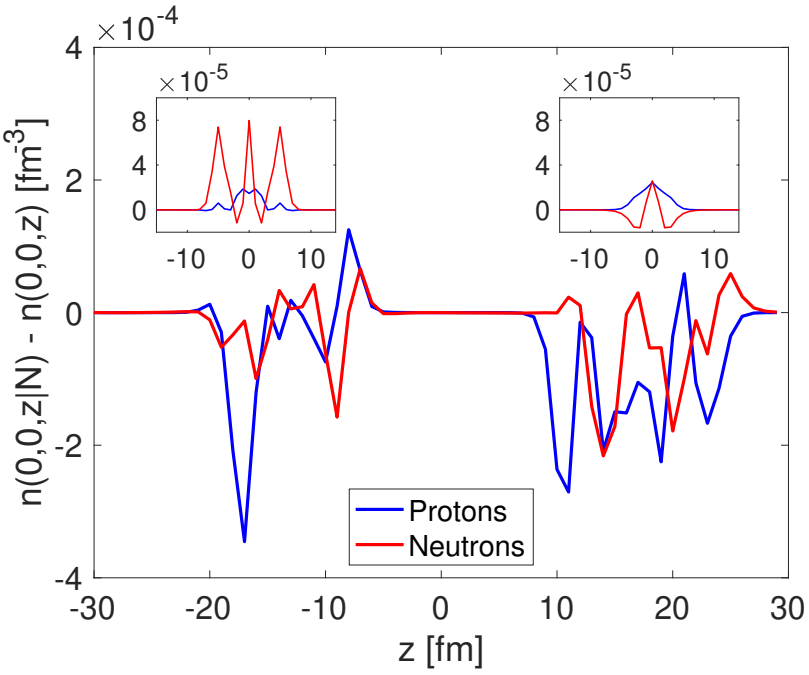

FIG. 39. Same as Fig. 38, except evaluated for the final state, where the fission fragments have fully separated.

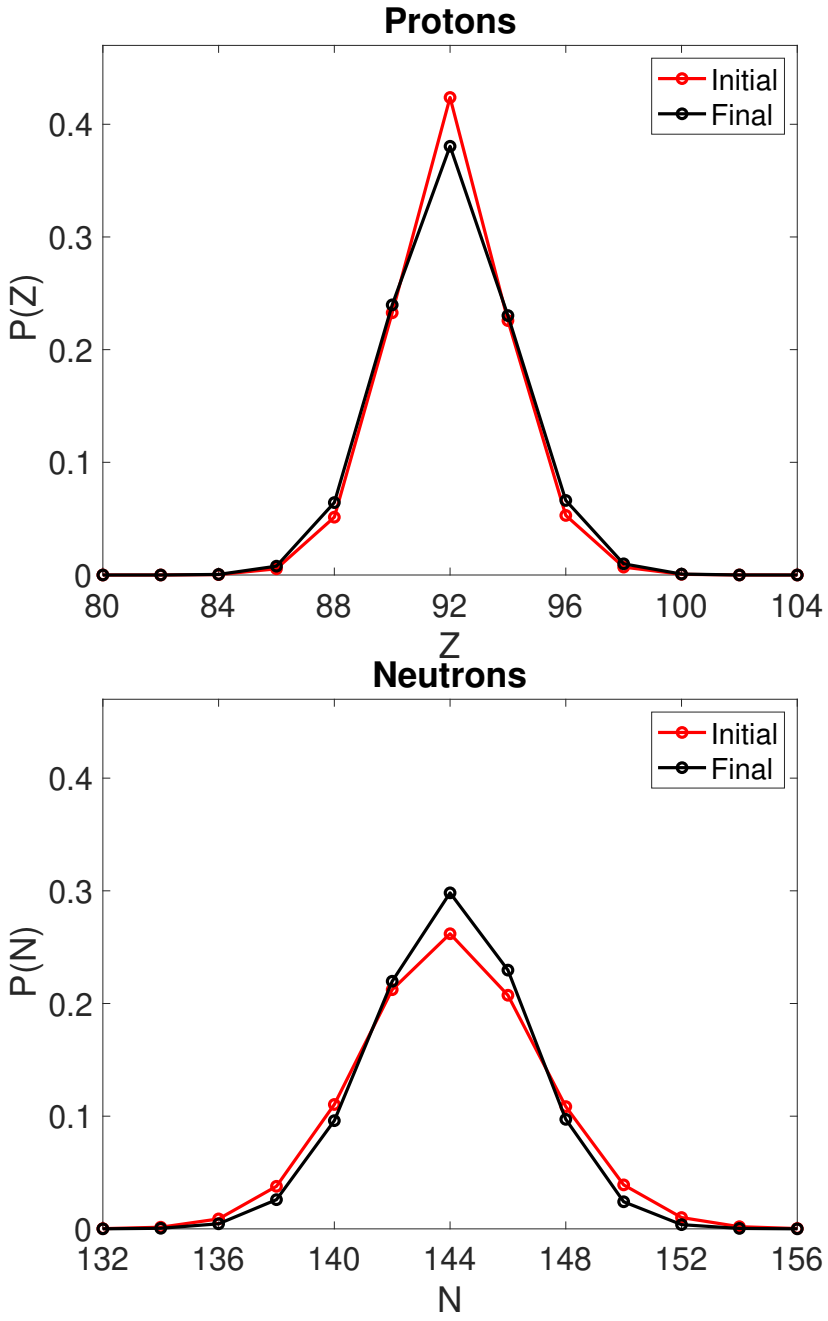

FIG. 40. Total system particle number distribution for protons and neutrons for the initial and final states.

IX. QUANTUM TURBULENCE, SUPERFLUIDITY, NON-MARKOVIAN DYNAMICS, AND WAVE FUNCTION THERMALIZATION

In this section, I review the results presented in the paper "Quantum Turbulence, Superfluidity, Non-Markovian Dynamics, and Wave Function Thermalization" by A. Bulgac, M. Kafker, I. Abdurrahman, and G. Wlazłowski, Phys. Rev. Research **6**, L042003 (2024) [5].

A. Abstract

The question of how thermalization is achieved in a system undergoing quantum turbulence has not yet been addressed in the literature. Quantum turbulence has been investigated in experiments, predominantly on superfluid ^{4}He and ^{3}He, as well as theoretically, but the dynamics of the quantized vortices have so far only been tracked in time until they decay into phonons. In this section, we consider the dynamics of the unitary Fermi gas (UFG), which is a unique strongly interacting quantum many-body system with no classical counterpart, and which is relevant for describing the behavior of the crust of neutron stars, cold atom systems, condensed matter systems, and nuclear many-body systems. In this section, we simulate the dynamics of a UFG prepared in an initial state consisting of a lattice of quantum vortices and antivortices, which subsequently evolves through several vortex tangles and the excitation of Kelvin waves, until very slowly it starts to thermalize. Following the study presented in Sec. VIII, we demonstrate that the dynamics of the UFG are non-Markovian, and we characterize the non-equilibrium dynamics of this crucial quantum system.

B. Introduction

It was conjectured by Feynman [249] in 1955 that superfluids, which are characterized by vanishing viscosity at zero temperature, can support a kind of turbulence through the effectively random crossing and reconnection of quantized vortices. This observation marked the beginning of the field of quantum turbulence (QT) [250, 251], a field which has been significantly influenced by the older field of classical turbulence (CT), in particular the idea of energy cascading from large scale spatial eddies to smaller scales due to Kolmogorov [252]. Of course, in any fluid system, a minimum size exists at which the energy cascade must terminate, which is determined either by the size of the constituent particles or thermal

effects, see Ref. [253] and references therein, and this is the case regardless of whether the fluid is classical or quantum in nature.

In this study, we will use the time-dependent superfluid local density approximation (TD-SLDA) to investigate the evolution of a UFG from an initial state composed of quantized vortices and antivortices, through the quantum turbulent evolution where the vortices cross and recombine, and well beyond, far into the regime where no vortices are present, where as we will show, the dynamics surprisingly remain interesting. In the regime under consideration, the non-equilibrium dynamics and thermalization of a many-fermion system [254–261] and the production of entropy [190, 191, 262] are typically treated as Markovian processes [263–267]. However, the results presented in Sec. VIII call that into question, and indeed we will show that the evolution of the UFG in the setup we just described is indeed non-Markovian, just as it was in the case of nuclear fission dynamics from saddle to scission. The dynamics of quantized vortices in the UFG is a system which is well understood from both a theoretical and experimental perspective [179], and it is relevant to a very large number of interesting physical systems, including neutron stars, nuclei, condensed matter systems, and cold Fermi gases. This is in contrast to the situation with superfluid ^{4}He and ^{3}He, which are both microscopically modeled primarily using the Gross-Pitaevskii equation [268, 269] and its kinetic extension [267], or from a phenomenological perspective. One choice which is common in the literature is to investigate the thermalization of a system which stirred or perturbed in some manner by an external influence. We instead simulate an isolated system here (with periodic boundary conditions) because the dynamics in the other case depend on the manner in which the system is coupled to the external influence, and so the case of the isolated system is clearer.

Dissipation is a critical ingredient for turbulence in classical fluids, which is usually studied using the incompressible Navier-Stokes equations

$$\frac{\partial \boldsymbol{u}}{\partial t} + (\boldsymbol{u}\cdot\nabla)\boldsymbol{u} = \nu\nabla^2\boldsymbol{u} - \frac{\nabla p}{\rho}, \quad \nabla\cdot\boldsymbol{u} = 0, \tag{62}$$

where ν, p, and ρ stand for the shear kinematic viscosity, pressure, and the matter density respectively. In the case were $\nu = 0$, we obtain the equation of motion for an ideal fluid, first derived in 1775 by L. Euler [270, 271]. The regime in which classical turbulence occurs is that of large Reynolds number $Re = uL/\nu$, or in the limit of small dissipation $\nu \to 0$, where L is the characteristic length of the flow. This is a strange situation, where the ideal

fluid, which has $\nu = 0$ and which does not support turbulence, should be obtained from the Navier-Stokes equations continuously in the limit $\nu \to 0$, but this obviously cannot be so, as this limit takes us further into the turbulent regime of the fluid. We are therefore led to conclude that the limit $\nu \to 0$ is undefined, and that one cannot obtain perfect fluid by taking a continuous limit of a turbulent fluid. Of course, we can see this another way, by observing that the shear kinematic viscosity ν appears next to the only second derivative in the Navier-Stokes equation, and we know that solutions of partial differential equations undergo qualitative changes when the highest order of the spatial derivatives changes from second to first (or vice versa) [272].

One can derive the Navier-Stokes equations from the Boltzmann equation [190, 191, 262, 264], which consists of a free transport part, which describes the independent particle motion, and the collision integral, which is responsible for local equilibration. The Boltzmann equation is only valid when describing dilute systems, in the case of instantaneous and localized collisions. One typically also invokes the assumption of "molecular chaos," which means that the collisions will be uncorrelated in both time and space, and hence the solutions of the Boltzmann equation will typically describe a system with Markovian behavior, with the collisions acting like Langevin noise in Brownian motion.

The UFG [179, 180, 273, 274] is a very interesting strongly interacting many-fermion system which does not have a classical limit. The interparticle interaction is characterized by a vanishing interaction range and an infinite scattering length [275], and it is known that the UFG exhibits a very large pairing gap and a large critical temperature [276, 277]. For this interaction, particles interact in the s-wave only, and the phase shift due to scattering is $\delta_0(k) \equiv \pi/2$, and the two-fermion scattering cross section reaches the maximum value allowed by unitarity $\sigma(k) = 4\pi/k^2$, where k is their relative wave vector. By dimensional analysis, we can determine that the only parameter with dimensions which determines the properties of the UFG is the average separation between particles [179]. Due to the short range pairing interaction in this system, and just like we saw in the case of nuclei, the single-particle occupation numbers behave as $n(\boldsymbol{k}) \to C/k^4$, in the limit $k \to \infty$ [187–189] for single-particle states with momentum $\mathbf{k}$. It follows that the total particle number $\int d^3k\, n(\boldsymbol{k})$ converges very slowly, and we see that the single-particle momentum distribution differs significantly from a Maxwellian distribution.

By substituting a different functional than the SeaLL1 functional we used to describe

nuclear systems, we may describe the dynamics of the unitary Fermi gas within the extension of time-dependent density functional theory to superfluid systems, the time-dependent superfluid local density approximation (TDSLDA) [67, 110, 215, 278], which one can show is fully equivalent to the theoretical description of the nonequilibrium evolution of a fermionic superfluid with the Gorkov equations [263, 279, 280], and which is also equivalent to a fully quantum mechanical extension of the Boltzmann equation [46], with the pairing field playing the role of the collision integral. Unlike in the (semi)classical Boltzmann equation [190, 191, 262, 264], TDSLDA can incorporate the effects of quantum interference and entanglement [66, 222, 281]. It has been demonstrated that after adjusting the fitting the parameters in the functional for describing the UFG, SLDA gives good agreement with quantum Monte Carlo calculations for this system [215, 273].

C. Results

We simulated the dynamics of the UFG using the code W-SLDA Toolkit [282], which has been used to describe a variety of complex behaviors of systems involving quantized vortices [66, 273, 283–290]. For this project, we used W-SLDA Toolkit to solve the TDSLDA equations on a 3D lattice of size $N^3 = 32^3$ with periodic boundary conditions and finite lattice constant l. This amounts to solving $2N^3 = 65,536$ coupled nonlinear complex-valued partial differential equations in 3D for 3.75×10^6 time steps, which is accomplished with a relative numerical error of 10^{-6} for the energy conservation and 10^{-8} for the particle number.

TDSLDA has previously been used to study vortex dynamics in the UFG [283–286], which revealed qualitative similarities with the behavior initially conjectured by Feynman [249]. In this study, we consider an initial constrained state of an unpolarized UFG at zero temperature [66] composed of 12 linear vortices and antivortices with zero total circulation. The underlying system consists of 1000 fermions, with equal numbers of spin up and spin down particles, with an average density of $n_0 = N/V \approx 0.03$ for the lattice constant $l = 1$. The system is then evolved in time, and the vortices bend, then cross and reconnect, while emitting phonons. As a result of these recombinations, the total linear extent of the vortex lines decreases with time, until finally no vortices remain, and the system appears to reach a "thermal" state.

In Fig. 41, we show the time evolution of the single-particle occupation probabilities

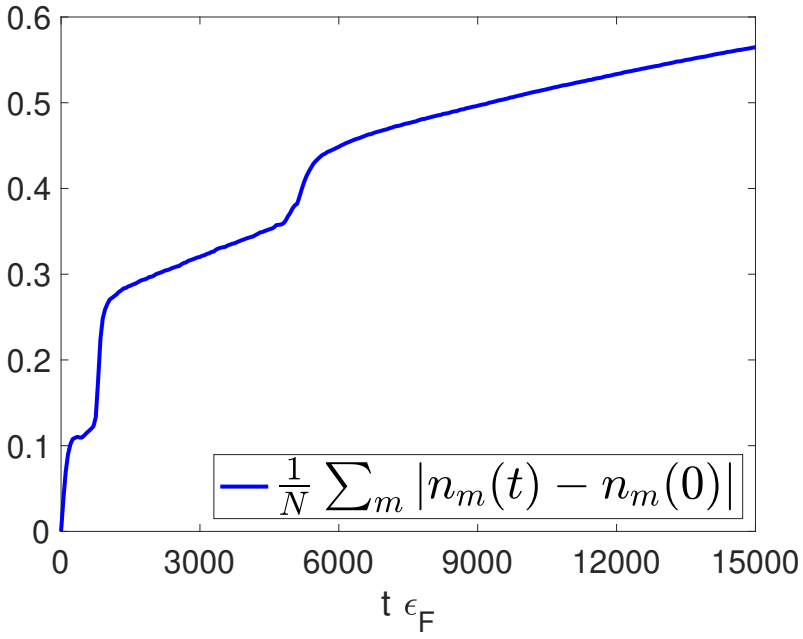

FIG. 41. The sum $0 \leq \sigma_1(t) \leq 2$, which describes the total absolute change in the single-particle occupation numbers over time, compared with the initial state. Linear regimes are clearly visible, separated by periods of rapid increase, in which the vortices are crossing and recombining, and the evolution of the system is turbulent.

$n_m(t)$, which are the fully quantum counterparts to the (semi)classical phase-space probability distribution typically used in kinetic equations. Specifically, we display the quantity [5, 46, 222]

$$\sigma_1(t) = \frac{\sum_m |n_m(t) - n_m(0)|}{N}, \quad 0 \leq \sigma_1(t) \leq 2, \tag{63}$$

which is a measure of the fractional change in all the single-particle occupation probabilities. In the case of a time-dependent Hartree-Fock calculation, the single-particle occupation numbers are either 0 or 1, and remain so for all times, so we will have $\sigma_1(t) = 0$. The presence of the pairing interaction leads to redistribution of the single-particle occupation numbers, and so we see a non-zero value of $\sigma_1(t)$. The occupation probabilities are plotted for the system at various times in Fig. 42. As was mentioned in the introduction, the collision integral in the Boltzmann equation acts like Langevin noise in the case of Brownian motion, which is to say the that the redistribution of the single particle occupation numbers in that case should be a Markovian process, and hence we expect the deviation of the occupation numbers from their initial values would obey $\sigma_1(t) \propto \sqrt{t}$ in that case. However,

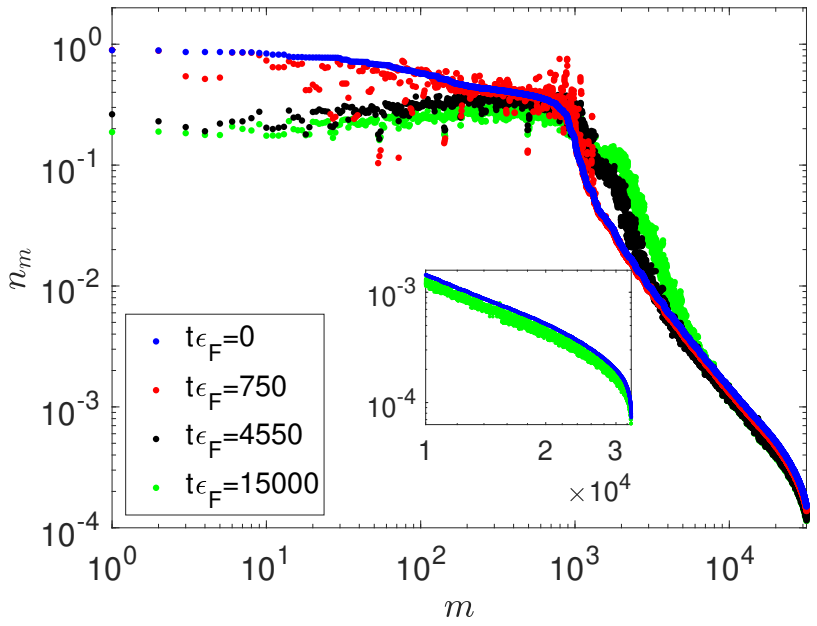

FIG. 42. The single particle occupation numbers $n_m(t) = v_m^2(t)$ evaluated at various times during the time-evolution of the UFG. Pairing interactions dramatically redistribute the occupation probabilities during dynamics, leading to significant differences between the initial occupation number distribution for the case of the 12 vortices and antivortices compared to the final apparently thermalized state. At all times, the occupation numbers are ordered in decreasing order of the initial occupation numbers $n_m(0)$, and due to particle number conservation, depopulation of low energy single-particle states is balanced by increased population at higher energy states.

Fig. 41 instead clearly shows piecewise linear behavior, which is a clear indication of non-Markovian dynamics, see also Sec. VIII, where the deviations from linear evolution occur during the crossing and reconnection of the vortices, which is to say the turbulent stages of the dynamics. We note that unlike the case of the (semi)classical Boltzmann equation, the UFG system considered here is not dilute, and so the "collisions" are not isolated in either space or time, which at least partially explains the behavior observed in Fig. 41. For times $t\epsilon_F < 700$, the vortices have begun to deform, but no crossings have yet occurred. During the interval $700 < t\epsilon_F < 1200$, the vortices begin to tangle, cross, and reconnect, with the overall effect being that the total linear extent of the vortices in the system shrinks. Following this interval, a configuration of four aligned vortices persists for a longer period, lasting until $t\epsilon_F \approx 4300$, at which point they too reconnect and finally annihilate. For all

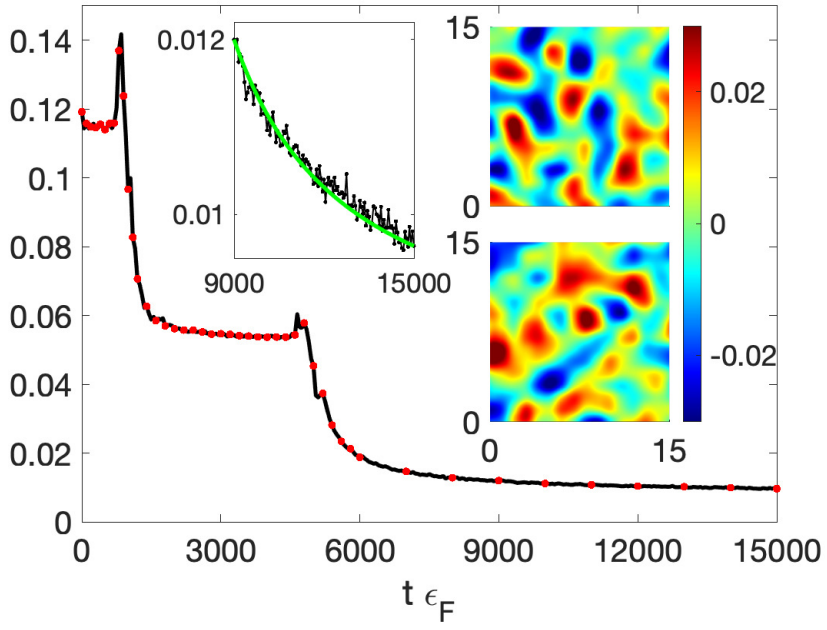

FIG. 43. The average magnitude of the density fluctuations, $\int_V d^3r|n(\boldsymbol{r},t)/n_0 - 1|/V$ (black line), evaluated as a function of time. Superimposed over this curve in red points are the fluctuations of the density which has been projected on the system's average particle number [291], showing nearly perfect agreement, as one expects for time-dependent density functional theory with [292] or without pairing correlations [293]. The insets on the right show the number density fluctuations in space, given by $n(x,0,z,t)/n_0 - 1$ at times $t\epsilon_F = 10000$ and 10050. The inset in the upper left shows the black curve, zoomed in at the quasihomogeneous stage where no more vortices are present, $t\epsilon_F > 9000$, together with a superimposed fit in green, see Eq. (64).

times $t\epsilon_F > 5000$ only local fluctuations of the number densities are present in the system in the system, see Fig. 43. We note, however, that even when the system appears rather spatially homogeneous, the evolution of the system is still decidedly non-Markovian, lasting until times at least exceeding $t\epsilon_F > 15000$, significantly beyond the point when the last vortices have disappeared.

We also show the time-dependence of the canonical occupation numbers, see Fig. 44, which are obtained by diagonalizing the system's number density matrix, see Secs. VII and VIII. Just as in the case of nuclear fission, this system has a zero-range interaction, and so we know the canonical occupation probabilities for single-particle states with momentum $\mathbf{k}$

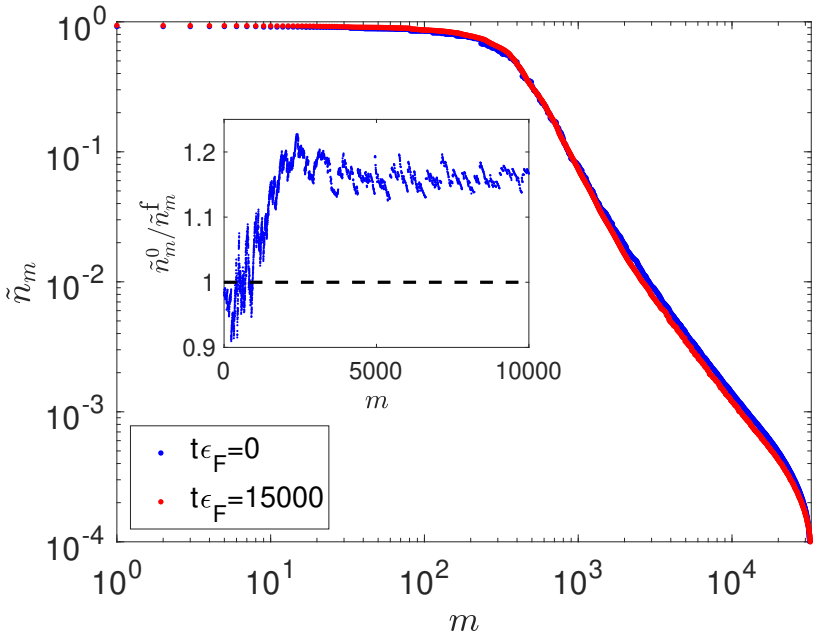

FIG. 44. The initial and final canonical occupation numbers, which are the eigenvalues of the number density matrix, arranged in decreasing order, see Secs. VII and VIII and the references therein. In the inset, their ratio, initial over final, is shown. Note, however, that since these canonical occupation numbers must be obtained by diagonalizing the one-body density matrix, there is no one-to-one relationship between the values m for the initial and final states.

will obey $\tilde{n}(k,t) \approx C/k^4$ [179, 180, 187–189, 274], and a power law trend is indeed clearly visible in Fig. 44 for states with $k \gg k_F$. Note however that for these large k values, $m \approx 4\pi k^3/3$ (as in the case of non-interacting fermions) and so the power law we see in the figure is $\tilde{n}_m(t) \approx \tilde{C}/m^{4/3}$. However, the situation for the UFG presented in Fig. 44 nevertheless differs significantly from the case of nuclear fission. Whereas in nuclear fission, we saw significant changes in the Fermi surface in the canonical basis, see for example Fig. 34, which corresponded to changes in the complexity of the many-body wave function during the saddle to scission evolution, these large changes in wave function complexity are not observed for the case of quantum turbulence considered here, and the initial state with vortices appears to have nearly identical many-body wave function complexity to the final quasi-uniform state.

Unlike the canonical occupation numbers, the Bogoliubov basis occupation numbers are dramatically redistributed by the dynamical evolution of the UFG, and if one looks at the

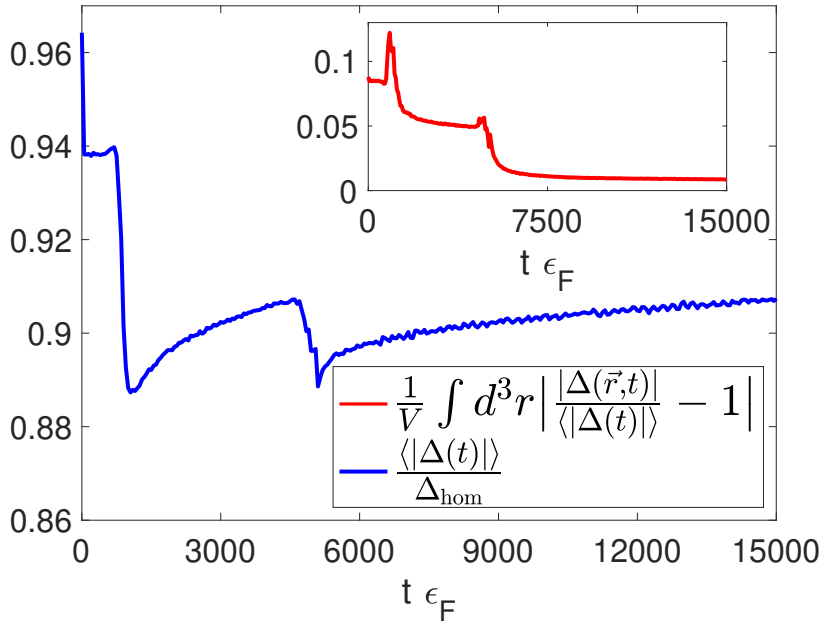

FIG. 45. Time dependence of the magnitude of the pairing gap, expressed as a fraction of its value for a homogeneous UFG prepared at the same density. The inset displays the spatially averaged fluctuation of this quantity as a function of time.

final state in Fig. 42, shown with green dots, one might suspect that the final state of the system is characterized by a very high temperature. However, if we look at the behavior of the average pairing gap of the system, shown in Fig. 45, we see that in the final state the magnitude of the gap has only decreased by about 5% relative to the initial state, and so the system has acquired an "effective" temperature, T, which nevertheless clearly obeys $T < T_c \approx 0.16\epsilon_F$ [294], and the UFG remains a superfluid in this final state.

An interesting question we can ask about our results is how the time evolution of the density fluctuations shown in Fig. 43 compares to what we would expect from the Eigenstate Thermalization Hypothesis [257], which predicts that "a generic initial state will approach thermal equilibrium at least as fast as $t_{therm} \approx \mathcal{O}(\hbar/\Delta E)$, where ΔE is the uncertainty in the total energy of the gas." It is straightforward to construct a fit to our density fluctuations

$$\delta[n(\vec{r},t)] = \frac{1}{V}\int d^3r \left| \frac{n(\vec{r},t)}{n_0} - 1 \right| \approx \delta n_\infty + \frac{t_{UFG}}{t - t_0}, \tag{64}$$

where δn_∞ is the asymptotic magnitude of the density fluctuations in the limit $t \to \infty$, when the system is fully thermalized. This average fluctuation quantity $\delta[n(\vec{r},t)]$ is an observable which can in principle be measured in cold atomic cloud experiments [295]. We show the

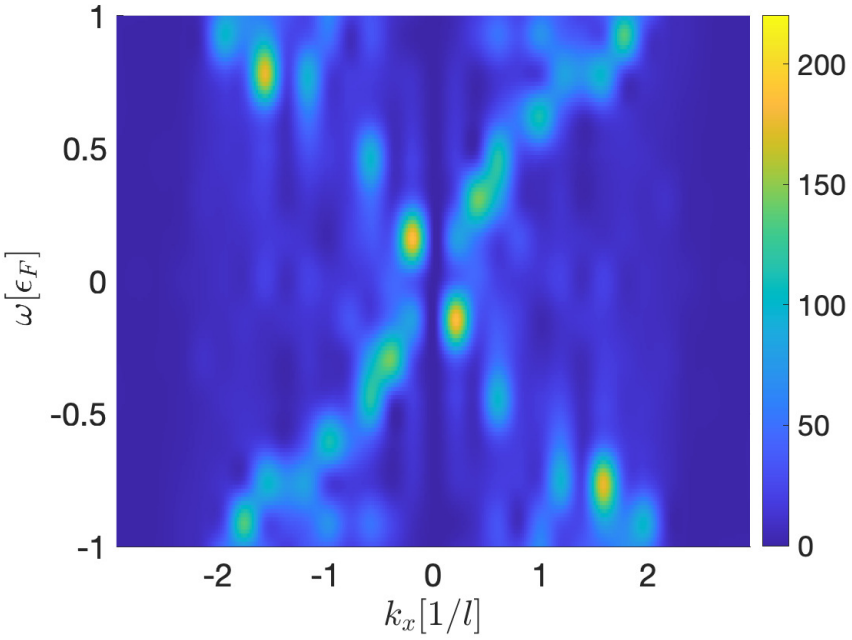

FIG. 46. Fourier transform in space and time of the density fluctuations of the system at late times. The Fourier transform was computed according to $S(\omega, k_{x,y,z}) = \int_V d^3r \int_T^{T+50} dt[n(\boldsymbol{r},t)/n_0 - 1]\exp(i\boldsymbol{k}\cdot\boldsymbol{r} - i\omega t)$, where V is the simulation box volume, $T = 15,000\epsilon_F$, and $\boldsymbol{k}$ was chosen parallel to the axis Ox. Choosing another axis for $\mathbf{k}$ leads to very similar results.

quality of this fit in the left inset of Fig. 43 for the period when the vortices have disappeared and the matter distribution in the UFG is quasiuniform. We can estimate the relaxation time according to the Eigenstate Thermalization Hypothesis to be

$$t_{ETH}\,\epsilon_F \approx \frac{1}{\Delta E} = \mathcal{O}(0.1) \ll t_{UFG}\,\epsilon_F = \mathcal{O}(10), \tag{65}$$

where we have estimated that the energy uncertainty in the UFG follows from the distribution of particle number for the many-body wave function, $\Delta E \approx \mu\Delta N(t)$. The thermalization time for the isolated UFG is orders of magnitude longer than the predicted rate from the Eigenstate Thermalization Hypothesis [257]. Evidently, the wave function thermalization process for this isolated quantum system proceeds much slower than expected based on existing discussions in the literature. Within the quasi-uniform regime of the UFG, one expects only to observe phonons, which should obey the dispersion relation $\omega^2 = k^2c_0^2$, where $c_0 = k_F\sqrt{\xi/3}$ is the sound velocity and ξ is the Bertsch parameter [179], see Fig. 46. This figure shows that this dispersion relation is only observed to hold on average, however, as

the system has not yet fully thermalized.

X. IMPACT OF THE CENTER OF MASS FLUCTUATIONS ON THE GROUND STATE PROPERTIES OF NUCLEI

In this section, we review the results presented in the manuscript "Impact of the Center of Mass Fluctuations on the Ground State Properties of Nuclei" by M. Kafker and A. Bulgac [3].

A. Abstract

Density functional theory (DFT) enables one to calculate nuclear ground state properties, including binding energies, across the nuclear chart, with fairly good accuracy. However, DFT is a mean field theory, and as such, it breaks many symmetries which the underlying nuclear Hamiltonian respects, the most important such symmetries being translational, rotation, and gauge symmetries, and in general these symmetries must be restored. Translational invariance is unique amongst the list of symmetries as it must be restored for all nuclei in DFT calculations, whereas for example rotational invariance only needs to be restored for deformed nuclei. The most common approach for restoring translational invariance, and hence for the implementation the center of mass (CoM) energy correction to the nuclear binding energy, see for example [14, 101], leads to a increase in the magnitude of the binding energy by 15-19 MeV, which varies rather weakly for medium- and large-mass nuclei. An improved CoM correction was suggested by Butler *et al.* [296], and this leads to an increase of 5-10 MeV. Both these corrections are significantly larger than the root-mean-square (RMS) error in the energy according to the Bethe-Weizsäcker mass formula, initially proposed by Gamow [297], which is about 3.5 MeV, which for heavy nuclei is about 0.2% of their mass. The correction due to Butler *et al.* [296] is also significantly larger than the RMS for the binding energy calculated within DFT, without restoring any broken symmetries or including zero-point energy fluctuations, which is about 2-3 MeV. In this section, we analyze yet another method for calculating the CoM correction, namely the method for restoring translational invariance of the many-body wave function (MBWF) suggested by Peierls and Yoccoz [298] (PY). The PY approach is equivalent from a methodological perspective to the techniques for restoring other broken symmetries in DFT. Furthermore, as we will demonstrate, it is the only approach to calculating the CoM correction to the mean field binding

energy which is not contaminated by contributions from excited states.

B. Motivation

To contextualize the problem of center of mass fluctuations, we briefly recall the textbook treatment of the two-body problem in quantum mechanics in the presence of a central potential. We start with the Hamiltonian

$$\hat{H} = -\frac{\hbar^2}{2m_1}\Delta_1 - \frac{\hbar^2}{2m_2}\Delta_2 + V(|\mathbf{r}_1 - \mathbf{r}_2|). \tag{66}$$

We then introduce the center of mass and relative coordinates $\mathbf{R} = (m_1\mathbf{r}_1 + m_2\mathbf{r}_2)/(m_1 + m_2)$ and $\mathbf{r} = \mathbf{r}_1 - \mathbf{r}_2$ and the total and reduced masses $M \equiv m_1 + m_2$, $\mu = m_1 m_2/(m_1 + m_2)$, in which case the Hamiltonian can be rewritten as

$$\hat{H} = -\frac{\hbar^2}{2M}\Delta_R - \frac{\hbar^2}{2\mu}\Delta_r + V(r). \tag{67}$$

The eigenstates of this Hamiltonian will thus be separable in the form

$$\psi(\mathbf{R}, \mathbf{r}) = \Phi_{\mathrm{CoM}}(\mathbf{R})\Psi_{\mathrm{rel}}(\mathbf{r}), \tag{68}$$

where the CoM motion is that of a free particle of mass M, and the relative motion is that of a particle of mass μ moving in a potential $V(r)$ centered on the origin. Note that the relative motion now depends on one fewer coordinate.

In mean field theory, one typically treats the problem differently. Rather than starting by separating the CoM and relative coordinates, one typically starts by saying that the cumulative effect of the forces acting between the particles in the system is to create a mean field potential centered on the origin, say a Woods-Saxon in the case of nuclear physics, and then one places A independent fermions in that potential. While this approach can generally give adequate solutions to the quantum many-body problem, the CoM motion has not been properly accounted for, and this formulation allows for unphysical behaviors such as the collective oscillation of the CoM about the potential minimum, and these oscillations carry additional energy which should obviously not contribute to the binding energy of the system, which should only depend on relative coordinates.

To see clearly that these spurious solutions are present, we consider the special case of the harmonic oscillator, where the CoM motion is separable. We place A equal mass particles in a harmonic well centered on the origin, in which case the Hamiltonian is given by

$$\hat{H} = \sum_{i=1}^{A} \left(\frac{\mathbf{p}_i^2}{2m} + \frac{1}{2} m\omega^2 \mathbf{r}_i^2 \right). \tag{69}$$

If we introduce the center of mass momentum $\mathbf{P} = \sum_i \mathbf{p}_i$, a simple algebraic manipulation shows that

$$\hat{H} = \sum_{i=1}^{A} \left(\frac{(\mathbf{p}_i - \frac{\mathbf{P}}{A})^2}{2m} + \frac{1}{2} m\omega^2 (\mathbf{r}_i - \mathbf{R})^2 \right) + \frac{\mathbf{P}^2}{2mA} + \frac{1}{2} mA\omega^2 \mathbf{R}^2 \equiv \hat{H}_{\text{intr}} + \hat{H}_{\text{CoM}}. \tag{70}$$

Evidently, the Hamiltonian can be split into independent intrinsic and CoM components, and so the many-body wave function can be expressed as a product of a wave function which depends only on the intrinsic coordinates and a wave function which depends only on the CoM coordinates. As the CoM Hamiltonian is itself a harmonic oscillator, we see that the CoM motion in the lowest energy state is not a plane wave as in the two-body example, but rather a Gaussian with a nonzero zero-point energy. This is the quantum mechanical manifestation of the collective oscillations of the matter distribution about the potential minimum, as we have $\langle \mathbf{R} \rangle = 0$, but $\langle \mathbf{R}^2 \rangle \neq 0$, and the latter fluctuations of the CoM position carry a minimum nonzero amount of energy. If the effects of this motion are not removed, we will mistakenly attribute the energy of CoM fluctuations to the nuclear binding energy, and thereby underestimate the magnitude of the binding energy. Said another way, the removal of the center of mass energy will lead to a more deeply bound nuclear ground state.

C. Introduction

The typical way in which one removes the center of mass energy is by subtracting the COM kinetic energy from the Hamiltonian, which gives a correction

$$E_{\text{CoM}} = -\langle \Phi | T_{\text{CoM}} | \Phi \rangle = -\left\langle \Phi \left| \frac{\mathbf{P}^2}{2mA} \right| \Phi \right\rangle = -\left\langle \Phi \left| \sum_i \frac{\mathbf{p}_i^2}{2mA} + \sum_{i<j} \frac{\mathbf{p}_i \cdot \mathbf{p}_j}{Am} \right| \Phi \right\rangle, \tag{71}$$

where here we use $m \approx (m_N + m_P)/2$ for the nucleon mass. The most common approach used in the literature [11, 14, 101] is simply to neglect the two body term in Eq. (71), which leads to a simple rescaling of the kinetic energy

$$\sum_i \frac{\mathbf{p}_i^2}{2m} \rightarrow \sum_i \frac{\mathbf{p}_i^2}{2m}\left(1 - \frac{1}{A}\right). \tag{72}$$

This was the approach for example used in the seminal paper by Vautherin and Brink [14] in which it was first demonstrated that density functional theory could be used to accurately reproduce nuclear binding energies, in that case for closed shell nuclei. In the case of a Fermi gas, with total energy $E = \frac{3}{5}A\varepsilon_F$, the center of mass energy is approximately

$$E_{\text{CoM}} \approx -\frac{1}{A}\left\langle \Phi \left| \sum_i \frac{\mathbf{p}_i^2}{2m} \right| \Phi \right\rangle \approx -\frac{3}{5}\varepsilon_F \approx -26 \text{ MeV}, \tag{73}$$

where we have used the Fermi energy for symmetric nuclear matter in the ground state. We might thus expect the actual magnitude of the CoM energy to depend only weakly on the particle number of the nucleus, and to be rather large in magnitude, when compared with the magnitude of the corrections due to restoring rotational or other symmetries. Using the SeaLL1 NEDF [12] for the seven spherical nuclei ^{16}O, ^{40}Ca, ^{48}Ca, ^{90}Zr, ^{100}Sn, ^{132}Sn, ^{208}Pb, we find that the magnitude of the CoM correction according to Eq. (72) can be approximately fit by

$$E_{\text{CoM}}^{\text{HF}} = -17.46 - \frac{15.17}{A^{1/6}} + \frac{28.01}{A^{1/3}} \pm 0.42 \text{ [MeV]}. \tag{74}$$

Of course, simply neglecting the second term in Eq. (71) is clearly an unsatisfactory and uncontrolled approximation, but there is a deeper issue with this approach, namely that the many-body wave function used in Eqs. (71) and (73) is not translationally invariant. We will demonstrate below that the use of a MBWF which is not translationally invariant leads to contributions to the CoM energy from excited states. Recall that it is necessary to restore translational invariance for all nuclei in the context of mean field theory, whereas the restoration of other symmetries such as rotational invariance is only required for a fraction of nuclei [101, 299]. The CoM energy also leads to an important correction in the case of fission barriers, as was shown by Berger *et al.* [300] using the Gogny interaction DS1, and

was also suggested by [301], where the impact of the CoM correction on the nuclear surface energy is also discussed. Below, we shall also return to the CoM energy results presented in [301], Fig. 9, for seven magic nuclei obtained using Eq. (71), including the two-body term.

It is important to note that restoring broken symmetries can significantly improve the root-mean-squared (RMS) error in the calculation of nuclear binding energies. In density function theory without the restoration of broken symmetries (including translational invariance, except possibly by using the approximation in Eq. (72)) [12, 14, 101], typical RMS errors are $\mathcal{O}(3)$ MeV across the nuclear chart. By contrast, the group of Goriely [118, 301] (see also earlier papers) includes the contributions from the restoration of a variety of broken symmetries and other effects while fitting their EDF parameters, thereby obtaining a significantly smaller RMS value of approximately 0.5-0.7 MeV. However, these authors have not separately published the magnitude of each symmetry-restoration correction in their several dozen studies published in the last few decades, so in particular the mass and charge dependence of each correction cannot be assessed from these works, and neither can their relative importance.

An improved prescription for approximating the CoM energy compared to Eq. (72), which however still does not include the evaluation of the two-body term in Eq. (71), was put forward by Butler *et al.* [296], see also [101], and is given by

$$\sum_i \frac{\hat{\mathbf{p}}_i^2}{2m} \to \sum_i \frac{\hat{\mathbf{p}}_i^2}{2m}\left(1 - \frac{2}{(N+2)A}\right), \tag{75}$$

$$A = \frac{2}{3}[(N+2)^3 - (N+2)]. \tag{76}$$

In this case N refers to the number of fully occupied harmonic oscillator shells in a closed-shell nucleus with $N = Z$. We can again estimate the mass dependence of this correction for the case of a Fermi gas, in which case we obtain

$$E_{CoM} \approx -\frac{2}{A(N+2)}\left\langle \Phi \left| \sum_i \frac{\hat{\mathbf{p}}_i^2}{2m} \right| \Phi \right\rangle \approx -\frac{6}{5(N+2)}\varepsilon_F. \tag{77}$$

Butler *et al.* [296] quote values for the CoM energy of 12.20 MeV for ^{16}O to 5.19 MeV for ^{208}Pb. By contrast, if we use Eq. (72) in a Hartree-Fock calculation for ^{208}Pb, we obtain a CoM energy of about 19 MeV. This difference is unexpectedly large, especially if we compare to the RMS error for the binding energy in the Bethe-Weizsäcker mass formula, which is at most 3.5 MeV. This large discrepancy between the results of different approximations is

the first of several inconsistencies we shall discuss here which point to the need to resolve the question of the precise magnitude of the CoM energy correction. When we included the Butler *et al.* [296] correction into the SeaLL1 NEDF [12], the RMS for the binding energy of spherical nuclei alone dropped significantly from 1.54 to 0.97 MeV.

We now turn to the question of the various estimates of the CoM energy correction and its mass dependence previously reported in the literature. As previously stated, there are a variety of conflicting claims in the literature, which are as follows.

- There is a very weak dependence and with $E_{CoM} \to$ const when A increases, see Ref. [301] Fig. 9, and Eqs. (73, 74)
- $E_{CoM} \approx 12.6A^{-0.131}$, see Fig. (4) in Ref. [302]
- $E_{CoM} \approx 30.71A^{-1/3}$ MeV [296], see Eq. (77). Recalling the discussion of the simple harmonic oscillator in the Motivation section, we see that this is very similar to approximating the CoM energy as the simply kinetic energy of the harmonic oscillator ground state, $E_{CoM} \approx 3\hbar\omega/4$, using the standard parameterization of the oscillator frequency as a function of the mass number, $\hbar\omega \approx 41A^{-1/3}$ MeV.
- $E_{CoM} \propto A^{-1}$ according to the qualitative arguments presented by Sheikh *et al.* [299], see sections 3.2.2 and 4.

In addition to these substantial disagreements, it has not been clearly reported in the literature how the magnitude of the CoM energy correction compares to those of the restoration of other broken symmetries. Just including the one-body term in Eq. (71) leads to a finite asymptotic correction $E_{CoM} \approx 18$ MeV, whereas including also the two-body term Da Costa *et al.* [301] report a different behavior, namely $E_{CoM} \approx 6 \ldots 8$ MeV for all magic nuclei. The mass dependence reported in [302] and [296] each lead to different results as well. In Fig. 47, we present these current best estimates from the literature, along with our own results from this study, which we explain in detail below.

Why is determining the correct magnitude of the CoM energy so important? For astrophysical applications, such predicting nuclear abundances and reactions in stars, the current accuracy of mean field approaches such as DFT is not sufficient, see Refs. [118, 301] and earlier references. An RMS error of the order $\mathcal{O}(100)$ keV in the binding energy is

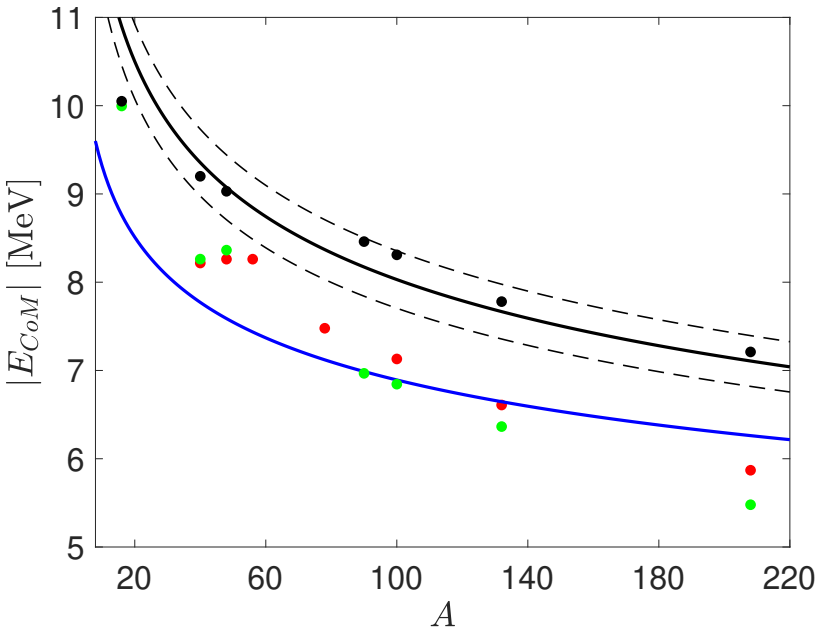

FIG. 47. A comparison of the various existing estimates in the literature for the mass dependence of the CoM energy correction, including our results from this manuscript prepared in black. Also plotted in black are the fit (solid line) and error bars (dashed lines) of the fit. Plotted in red are the results from Da Costa *et al.* [301], Fig. 9. In blue is the relationship from Dobaczewski [302], Fig. 4. We used SeaLL1 estimates for the nuclear kinetic energy to produce the datapoints for Butler *et al.* [303] approach, shown in green. Note that the magnitude of the CoM energy due to the PY approach exceeds in all cases that of all other results found in the literature.

needed [304–307], and clearly discrepancies of several MeV must be addressed before such levels of accuracy can be obtained.

We next address another claim previously made in the literature on restoring Galilean invariance. In discussing this topic, Peierls and Yoccoz [298] and Peierls and Thouless [308] made the claim that the nuclear mass should be $M_A = Am$, see also more recent works [11, 299, 302], a statement which is obviously inconsistent with the universally known fact among nuclear physicists that the nuclear binding energy lowers the mass of the nucleus compared to the mass of its constituent nucleons considered separately. The correct formula should therefore be

$$\hat{\mathrm{T}}_{CoM} = \frac{\hat{\mathbf{P}}^2_{CoM}}{2M_A}, \quad \text{where} \quad M_A c^2 = Amc^2 - \mathrm{BE}, \tag{78}$$

and where the binding energy BE is a relativistic correction of $\mathcal{O}(0.01\,Amc^2) \approx 7\ldots8\times$

A MeV. We also note that the PY nuclear masses reported in [299, 302] are in severe disagreement with experiment, considering Eq. (78), as in the case of ^{208}Pb, these authors report a correction to the evaluated mass of about 10-15 GeV, almost an order of magnitude larger than the known binding energy of 1.635 GeV.

D. Results

In this study, we implement the technique for restoration of translational invariance suggested in the 1950's by Peierls and Yoccoz [298] (PY), which has not been extensively used in the literature since, only for nuclei with $A \leq 40$ in Refs. [309–314], with the exception of Ref. [302]. Ref. [313] is the latest and most complete study of restoring translational invariance and projecting the CoM motion using the PY procedure. However, there are several significant differences with this work, namely that the authors perform a mean field calculation where the CoM kinetic energy is subtracted according to Eq. (71), and compare with the results from a variation-after-projection (VAP) implementation of the PY procedure, whereas our results are instead projection-after-variation (PAV), as we shall elaborate below, so we cannot directly compare the magnitude of the CoM correction obtained by these authors with our own. Nevertheless, as comparison with the results from these authors shows, the difference between VAP and PAV in this case is about 1.5 MeV or less, noticeably smaller than the results of the CoM energy reported here, but still important to account for in light of the stringent astrophysics requirements mentioned above.

PY suggested a straightforward method for projecting an arbitrary many-body wave function $\Phi(\mathbf{r}_1, \ldots, \mathbf{r}_A)$ for A nucleons onto a specific value of the center of mass momentum,

$$C_{\boldsymbol{n}} \Psi_{\boldsymbol{n}}(\mathbf{r}_1, \ldots, \mathbf{r}_A) = \int \frac{d^3\mathbf{a}}{V} \Phi(\mathbf{r}_1 - \mathbf{a}, \ldots, \mathbf{r}_A - \mathbf{a}) e^{-i\mathbf{P}_{\boldsymbol{n}} \cdot (\mathbf{R} - \mathbf{a})/\hbar}, \tag{79}$$

where $|C_{\mathbf{n}}|^2$ is the probability for finding the component of the original many-body wave function with CoM momentum $\mathbf{P}_{\boldsymbol{n}}$ in $\Phi(\mathbf{r}_1, \ldots, \mathbf{r}_A)$,

$$\Phi(\mathbf{r}_1, \ldots, \mathbf{r}_A) = \sum\!\!\!\!\!\!\int_{\boldsymbol{n}} C_{\boldsymbol{n}} \Psi_{\boldsymbol{n}}(\mathbf{r}_1, \ldots, \mathbf{r}_A) e^{i\mathbf{P}_{\boldsymbol{n}} \cdot \mathbf{R}/\hbar}. \tag{80}$$

Here, V is the volume of the simulation box, and $\langle \Phi | \Phi \rangle = \langle \Psi_{\boldsymbol{n}} | \Psi_{\boldsymbol{n}} \rangle = 1$. From Eq. (79) and (80), it is clear that if we do not restore translational invariance, our MBWF is a superposition of states with different values of CoM momentum $\mathbf{P}_{\boldsymbol{n}}$. Recalling our discussion

of the two-body problem in the Motivation section, it is important to remember that the new functions $\Psi_{\boldsymbol{n}}(\mathbf{r}_1,\ldots,\mathbf{r}_A)$ are really only a function of $A-1$ coordinates, whereas our original MBWF $\Phi(\mathbf{r}_1,\ldots,\mathbf{r}_A)$ is a function of A coordinates. We must include the factor of $1/V$ in Eq. (79) to ensure that this operation is a projector. Note that we are not displaying spin or isospin coordinates as their presence does not affect the argument. In a finite simulation box of size $L = V^{1/3}$, the intrinsic dynamics are characterized by a well-defined CoM momentum $\mathbf{P}_{\boldsymbol{n}} = \frac{2\pi \boldsymbol{n}\hbar}{L}$, where $\boldsymbol{n} = (n_x, n_y, n_z)$ is an integer vector. Clearly, when we project on a specific value of the CoM momentum, the ground state will be given by $\mathbf{P} \equiv \mathbf{0} = (0,0,0)$. Making use of this decomposition in Eqs. (79) and (80), one can show several useful results. Firstly, concerning the new wave functions $\Psi_{\boldsymbol{n}}$, we have

$$E_{\mathbf{n}} = \langle \Psi_{\mathbf{n}} | \hat{\mathrm{H}} - \hat{\mathrm{T}}_{CoM} | \Psi_{\mathbf{n}} \rangle \equiv \langle \Psi_{\mathbf{n}} | \hat{\mathrm{H}} | \Psi_{\mathbf{n}} \rangle, \tag{81}$$

$$\Psi_{\boldsymbol{n}}(\mathbf{r}_1,\ldots,\mathbf{r}_A) \neq \Psi_{\mathbf{0}}(\mathbf{r}_1,\ldots,\mathbf{r}_A), \text{ if } \mathbf{n} \neq \mathbf{0}, \tag{82}$$

$$E_{\boldsymbol{n}} \neq E_{\boldsymbol{m}}, \quad \text{if} \quad \boldsymbol{n} \neq \boldsymbol{m}, \text{ and } E_{\mathbf{0}} < E_{\boldsymbol{n}}, \quad \text{if} \quad \boldsymbol{n} \neq \mathbf{0}. \tag{83}$$

Furthermore, concerning the most common approach in the literature, which is to calculate the CoM energy using a wave function which is not translationally invariant, we see with these new formulas that

$$\langle \Phi | \hat{\mathrm{H}} - \hat{\mathrm{T}}_{CoM} | \Phi \rangle = \sum\!\!\!\!\!\!\int_{\boldsymbol{n}} |C_{\boldsymbol{n}}|^2 E_{\boldsymbol{n}} > E_{\mathbf{0}}, \; \sum\!\!\!\!\!\!\int_{\boldsymbol{n}} |C_{\boldsymbol{n}}|^2 = 1, \tag{84}$$

and, Eq. (71), can be seen to take on the form

$$E_{CoM} \text{ “}=\text{”} \; -\langle \Phi | \hat{\mathrm{T}}_{CoM} | \Phi \rangle = -\sum\!\!\!\!\!\!\int_{\boldsymbol{n}} |C_{\boldsymbol{n}}|^2 \frac{|\mathbf{P}_{\boldsymbol{n}}|^2}{2Am}, \tag{85}$$

where we have used “=” to emphasize that, in light of this new formulation, the claim that this expression is actually the CoM energy is dubious. Indeed, we see that this expression is actually a sum over all excited states of the CoM momentum, whereas we obviously only want the ground state value. As we are performing a projection on zero CoM momentum, we transparently now have

$$\langle \Psi_{\mathbf{0}} | \hat{\mathrm{T}}_{CoM} | \Psi_{\mathbf{0}} \rangle \equiv 0, \langle \Psi_{\mathbf{0}} | \hat{\mathbf{P}}_{CoM} | \Psi_{\mathbf{0}} \rangle \equiv \mathbf{0}. \tag{86}$$

And perhaps most significantly, we have

$$E_{gs} = E_{\mathbf{0}} = \langle \Psi_{\mathbf{0}} | \hat{\mathrm{H}} | \Psi_{\mathbf{0}} \rangle < \langle \Phi | \hat{\mathrm{H}} - \hat{\mathrm{T}}_{CoM} | \Phi \rangle. \tag{87}$$

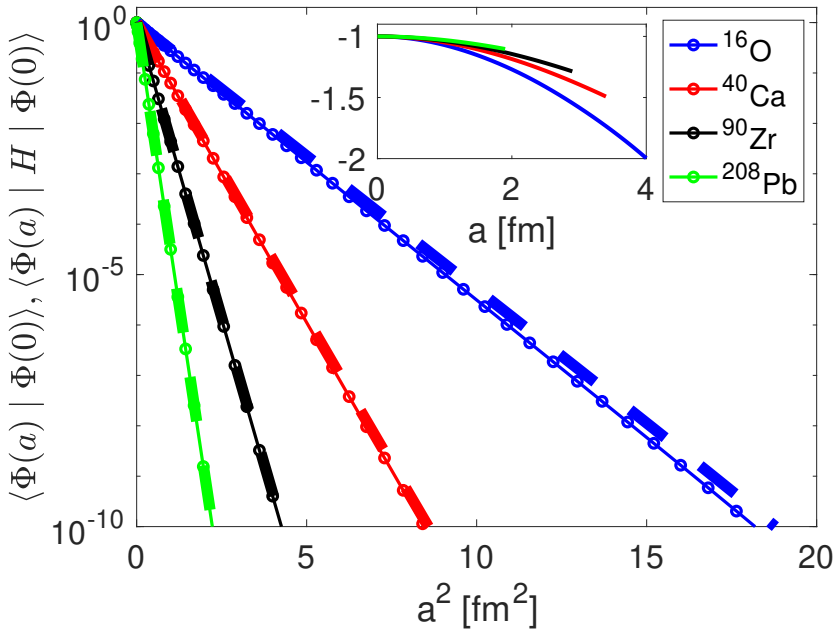

FIG. 48. The solid lines show the many-body wave function overlap $\langle\Phi(a)|\Phi(0)\rangle$ as a function of a^2, which exhibits a clear Gaussian profile, $\langle\Phi(\mathbf{a})|\Phi(\mathbf{0})\rangle \approx \exp[-\mathbf{a}^2/(2\sigma_{\mathcal{O}}^2)]$, for the DFT ground states of four spherical nuclei. The dashed lines show the Hamiltonian overlap $\langle\Phi(\mathbf{a})|H|\Phi(\mathbf{0})\rangle$ normalized to $\langle\Phi(\mathbf{0})|H|\Phi(\mathbf{0})\rangle$. In the inset we plot the quantity $\mathcal{H}(\mathbf{a},\mathbf{0})$, see Eq. (94), normalized to the absolute value $|\mathcal{H}(\mathbf{0},\mathbf{0})|$.

Although this last result is straightforward to obtain, we do not believe it has ever been presented in the literature before. These new formulas reveal that the usual prescriptions used to calculate the CoM energy within DFT and other mean field theories, Eqs. (71),(84),(85), and *a fortiori* (72) are necessarily inaccurate. It is clear from Eq. (85) that this expression for the CoM kinetic energy contains contributions from all excited states with nonzero CoM momentum,

$$|C_{\boldsymbol{n}}|^2 = \int \frac{d^3\mathbf{a}}{V} \exp\left(i\frac{\mathbf{P}_{\boldsymbol{n}}\cdot\mathbf{a}}{\hbar}\right)\langle\Phi(\mathbf{a})|\Phi(\mathbf{0})\rangle \tag{88}$$

$$\approx \frac{(\sqrt{2\pi}\sigma_{\mathcal{O}})^3}{V}\exp\left(-\frac{|\mathbf{P}_{\boldsymbol{n}}|^2\sigma_{\mathcal{O}}^2}{2\hbar^2}\right) \ll 1, \tag{89}$$

see Fig. 48 for more details.

We offer an explanation as to why the expression $\langle\Phi|\hat{\mathrm{H}} - \hat{\mathrm{T}}_{CoM}|\Phi\rangle$ does not produce an accurate estimate of the ground state energy. The Hamiltonian for the intrinsic motion is given by $\hat{\mathrm{H}} - \hat{\mathrm{T}}_{CoM}$, and the intrinsic ground state energy is determined by the intrinsic

translationally invariant MBWF $|\Psi_{\mathbf{0}}\rangle \neq |\Phi\rangle$. In order to evaluate the ground state Slater determinant $|\Phi\rangle$, one perturbs the intrinsic Hamiltonian by adding back $\hat{\mathrm{T}}_{CoM}$, which can be thought of as a small "perturbation." However, going to first order in perturbation theory is insufficient to obtain a physically accurate estimate of the ground state energy E_{gs}, and one must go to at least second order, where it is known that the correction to the ground state energy is negative, hence the inequality in Eq. (87).

The PY approach to CoM correction avoids many of the issues with Eq. (71). Specifically, this equation does not actually restore the translational invariance of the MBWF but instead merely tries to correct the energy, which is methodologically inconsistent with the other symmetry restoration approaches, in which the functional form of the MBWF is actually modified to restore the broken symmetry, see discussion below. Furthermore, Eq. (71) neglects the role of nuclear interactions, and includes contributions from excited states, see Eqs. (84), (87). The PY translational symmetry restoration approach operates in an identical manner to the complete delocalization of electron states into Bloch waves in conductors conductors [315]. While the COM motion in our initial Slater determinant wave function $\Phi(\mathbf{r}_1, \ldots, \mathbf{r}_A)$ is strongly localized–recall the harmonic oscillator case in the Motivations section–the wave functions $\Psi_{\boldsymbol{n}}(\mathbf{r}_1, \ldots, \mathbf{r}_A)e^{i\mathbf{P}_{\boldsymbol{n}}\cdot\mathbf{R}/\hbar}$ are fully delocalized. From Eq. (89), we obtain the volume of the region in which the CoM fluctuates, which is $(\sqrt{2\pi}\sigma_{\mathcal{O}})^3$ = 3.86 fm^3 and 0.17 fm^3 for ^{16}O and ^{208}Pb, corresponding to cubes of side 1.57 fm and 0.55 fm for ^{16}O and ^{208}Pb respectively, see Table VI. We can use Eq. (89) to estimate the CoM energy from Eq.(85), and the values are in good agreement with those reported in Table VI, as they should be. Using our results, Eqs. (84, 85), or those of [118], who use Eq.(71), we obtain that $|C_{\boldsymbol{n}}|^2$ exhibits a maximum at CoM momentum $|\mathbf{P}_{\boldsymbol{n}}|$ = 315 MeV/c for ^{16}O and 895 MeV/c for ^{208}Pb, which points to a sizable width of the CoM momentum distribution in the mean field theory ground state Slater determinant in the absence translational symmetry restoration.

As was mentioned above, the PY symmetry restoration approach operates on the same principles as other symmetry restoration approaches, namely that the symmetry is reinstated at the level of the mathematical functional form of the many-body wave function, see for example the case of the projection to zero total angular momentum in the case of an even-even deformed nucleus [11],

$$\hat{P}^0_{00}|\Phi\rangle = \int \frac{d\Omega}{8\pi^2} D^0_{00}(\Omega)\hat{R}(\Omega)|\Phi\rangle, \tag{90}$$

Nucl.	$E_{\rm CoM}$	$T_{\rm CoM}$	$r_{\rm mat}$	$\Delta r_{\rm mat}$	$r_{\rm ch}$	$\Delta r_{\rm ch}$	$\sigma_{\mathcal{O}}$	$\Delta\sigma$
^{16}O	-10.05	-11.20	2.66	0.058	2.67	0.058	0.626	0.010
^{40}Ca	-9.20	-9.62	3.38	0.020	3.40	0.021	0.429	0.003
^{48}Ca	-9.03	-9.68	3.53	0.015	3.44	0.014	0.392	0.002
^{90}Zr	-8.46	-8.43	4.26	0.008	4.22	0.007	0.305	0.0009
^{100}Sn	-8.31	-8.31	4.39	0.006	4.43	0.006	0.290	0.0008
^{132}Sn	-7.78	-8.00	4.82	0.005	4.69	0.004	0.263	0.0005
^{208}Pb	-7.21	-7.26	5.57	0.003	5.49	0.003	0.220	0.0003

TABLE VI. Center of mass energy E_{CoM} is defined in Eq. (91). The CoM kinetic energy $T_{\rm CoM}$ is defined in Eq. (106), see below. $r_{\rm mat}, \Delta r_{\rm mat}, r_{\rm ch}, \Delta r_{\rm ch}$ are the matter and charge radii, as well as the amount by which they change upon performing the PY CoM projection. All data reported here are for self-consistent Hartree-Fock calculations implemented using the SeaLL1 nuclear energy density functional [12]. The mass dependence of the CoM energy is approximately captured by $E_{CoM} \approx (-17.3 \pm 0.7)A^{-1/6}$ MeV and $T_{CoM} \approx (-17.93 \pm 0.26)A^{-1/6}$. Note that we did not include the nucleon charge form factors in these calculations. These form factors are used when evaluating charge densities as corrections using the F_2^A convolution approximation [172, 316, 317]. The last two columns list the fitted standard deviations of the obviously gaussian norm and Hamiltonian overlaps shown in Fig. 48. The standard deviation of the Hamiltonian overlap is reported as $\Delta\sigma$, the increase relative to the standard deviation of the norm overlap $\sigma_{\mathcal{O}}$.

and also the projection onto a state of definite particle number in the case of a system with pairing correlations, where before projection the MBWF is a superposition over states with different particle numbers. Restoring broken symmetries in this manner, by constructing MBWFs which are explicitly invariant under the relevant mathematical transformation, is therefore accomplished using precisely the same principles for all broken symmetries in mean field theory, including translational, rotational, and gauge symmetries. This is one strong argument in favor of the PY approach to restoring translational invariance, and against the technique exemplified in Eq. (71), which only offers an estimate of the CoM kinetic energy, but does not restore the broken symmetry.

In the PY framework, the correct CoM energy correction to the binding energy is given

by

$$E_{CoM} = \langle \Psi_{\mathbf{0}} | \hat{\mathrm{H}} | \Psi_{\mathbf{0}} \rangle - \langle \Phi | \hat{\mathrm{H}} | \Phi \rangle = E_{gs} - E_{MF} \leq 0. \tag{91}$$

A simple change of variables gives a slightly nicer expression for the ground state energy,

$$E_{gs} = \frac{\langle \Psi_{\mathbf{0}} | \hat{\mathrm{H}} | \Phi \rangle}{\langle \Psi_{\mathbf{0}} | \Phi \rangle} = \frac{\int d^3\mathbf{a} \langle \Phi(\mathbf{a}) | \hat{\mathrm{H}} | \Phi(\mathbf{0}) \rangle}{\int d^3\mathbf{a} \langle \Phi(\mathbf{a}) | \Phi(\mathbf{0}) \rangle}. \tag{92}$$

We note that this expression for the ground state energy is precisely a generator coordinate method (GCM) expression [11, 43], a topic to which we shall return in the next chapter of this thesis on the Enhanced Generate Coordinate Method, which we apply to the problem of heavy ion collisions. Indeed, the PY MBWF in Eq. (79), $\Psi_{\mathbf{0}}(\mathbf{r}_1, \ldots, \mathbf{r}_A)$, for the projection on zero CoM momentum is precisely of the GCM form advocated a few months later in the same year, 1957, by Griffin and Wheeler [43]. Standard formulas already exist in the literature for GCM expressions of this type, see Ring and Schuck [11],

$$\langle \Phi(\mathbf{a}) | \hat{\mathrm{H}} | \Phi(\mathbf{0}) \rangle = \langle \Phi(\mathbf{a}) | \Phi(\mathbf{0}) \rangle \mathcal{H}(\mathbf{a}, \mathbf{0}), \tag{93}$$

$$\mathcal{H}(\mathbf{a}, \mathbf{0}) = \left[Tr(\hat{\mathrm{T}} n^{\mathbf{a},\mathbf{0}}) + \frac{1}{2} Tr_1 Tr_2 (n^{\mathbf{a},\mathbf{0}} \hat{V}_2 n^{\mathbf{a},\mathbf{0}}) + \ldots \right], \tag{94}$$

$$n^{\mathbf{a}\mathbf{0}}(\mathbf{r}, \sigma | \mathbf{r}', \sigma') = \frac{\langle \Phi(\mathbf{a}) | \psi^\dagger(\mathbf{r}', \sigma') \psi(\mathbf{r}, \sigma) | \Phi(\mathbf{0}) \rangle}{\langle \Phi(\mathbf{a}) | \Phi(\mathbf{0}) \rangle}, \tag{95}$$

where $\hat{T}$ is the one body part of the Hamiltonian (typically the kinetic energy and possibly an applied external potential), $\hat{V}_2$ is the two-body interaction, ψ and $\psi^\dagger$ are the field operators, and the ellipses are for terms arising from anomalous densities when present, three-particle interactions, etc. The PY CoM energy Eq. (91) and Eq. (92) thus clearly reveal that the effects of nuclear interactions must be accounted for when calculating the CoM energy, a contribution which is clearly absent from the commonly used correction Eq. (71), although in practice the magnitude of the contribution from the interactions appears to be small, see Table VI, particularly for heavier nuclei.

In the case of single Slater determinants, the norm overlap $\langle \Phi(\mathbf{a}) | \Phi(\mathbf{0}) \rangle$ is particularly simple, just being given by the determinant of the single particle overlap matrix, M,

$$M_{kl}(\mathbf{a}) = \langle \phi_k(\mathbf{a}) | \phi_l(\mathbf{0}) \rangle, \ \langle \Phi(\mathbf{a}) | \Phi(\mathbf{0}) \rangle = \mathrm{Det} M(\mathbf{a}). \tag{96}$$

To evaluate the nuclear binding energy using Eq. (92), we require the new one-body "tran-

sition" density matrix,

$$n^{\mathbf{a0}}(\mathbf{r},\sigma|\mathbf{r}',\sigma') = \frac{\langle\Phi(\mathbf{a})|\psi^\dagger(\mathbf{r}',\sigma')\psi(\mathbf{r},\sigma)|\Phi(\mathbf{0})\rangle}{\langle\Phi(\mathbf{a})|\Phi(\mathbf{0})\rangle}$$
$$= \sum_{kl}\phi_k(\mathbf{0}|\mathbf{r},\sigma)\rho^{\mathbf{a0}}_{kl}\phi^*_l(\mathbf{a}|\mathbf{r}',\sigma'), \tag{97}$$

$$\rho^{\mathbf{a0}}_{kl} = \frac{\langle\Phi(\mathbf{a})|c^\dagger_l c_k|\Phi(\mathbf{0})\rangle}{\langle\Phi(\mathbf{a})|\Phi(\mathbf{0})\rangle} = M^{-1}_{kl}(\mathbf{a}), \tag{98}$$

These new transition density matrices obey the following relations

$$\sum\!\!\!\!\!\!\int_{\mathbf{r}',\sigma'} n^{\mathbf{a0}}(\mathbf{r},\sigma|\mathbf{r}',\sigma')n^{\mathbf{a0}}(\mathbf{r}',\sigma'|\mathbf{r}'',\sigma'') = n^{\mathbf{a0}}(\mathbf{r},\sigma|\mathbf{r}'',\sigma''), \tag{99}$$

$$\sum\!\!\!\!\!\!\int_{\mathbf{r}} n^{\mathbf{a0}}(\mathbf{r},\sigma,\mathbf{r},\sigma) = A \quad \text{(total particle number)}, \tag{100}$$

$$\phi_k(\mathbf{0}|\mathbf{r},\sigma) = \langle 0|\psi(\mathbf{r},\sigma)c^\dagger_k|0\rangle,\ |\phi_k(\mathbf{0})\rangle = c^\dagger_k|0\rangle, \tag{101}$$

$$\psi^\dagger(\mathbf{r}',\sigma') = \sum_l \phi^*_l(\mathbf{r}',\sigma')c^\dagger_l,\ \psi(\mathbf{r},\sigma) = \sum_k \phi_k(\mathbf{r},\sigma)c_k, \tag{102}$$

$$|\Phi(\mathbf{0})\rangle = \prod_m c^\dagger_m|0\rangle. \tag{103}$$

Eq. (99) clearly demonstrates that, like the standard density matrix, the new transition density matrix is also a projector. This object was first introduced by Löwdin [318], and it can be used to evaluate the Hamiltonian overlap $\langle\Phi(\mathbf{a})|\hat{\mathrm{H}}|\Phi(\mathbf{0})\rangle$ for any type of interactions between fermions, including the case of density functional theory, where this number density and the related kinetic, current, and spin-orbit transition densities enter into the density functional exactly as in the case of the familiar Skryme-like Hartree-Fock expression. In other words, this approach is identical to that of Kohn and Sham [319], in which a Hartree-like EDF is defined in terms of the various densities listed above, and which is ubiquitous in the literature nowadays for the treatment of electronic systems [320, 321], and which is also in alignment with current approaches for symmetry restoration in finite systems [299]. One can also make a strong argument that one can use this approach of using transition densities with an energy density functional for the case of the Unitary Fermi Gas [67, 110, 215, 273], where a simple argument by dimensional analysis reveals that fractional powers of number densities must appear in the functional. This approach is consistent with the Hohenberg-Kohn theorem [13], which states that the exact many-body wave function is determined in terms of the number density alone, although it does not describe how to construct such a functional.

In cases where symmetry is present, for example closed-shell spherical nuclei, with zero total angular momentum, one can use the symmetry to speed up the calculation of the matrix elements $\langle\Phi(\mathbf{a})|H|\Phi(\mathbf{0})\rangle$ and $\langle\Phi(\mathbf{a})|\Phi(\mathbf{0})\rangle$ using

$$\int d^3\mathbf{a}\langle\Phi(\mathbf{a})|\hat{\mathrm{H}}|\Phi(\mathbf{0})\rangle \equiv 4\pi\int_0^\infty da\, a^2\langle\Phi(a)|\hat{\mathrm{H}}|\Phi(0)\rangle, \tag{104}$$

$$\int d^3\mathbf{a}\langle\Phi(\mathbf{a})|\Phi(\mathbf{0})\rangle \equiv 4\pi\int_0^\infty da\, a^2\langle\Phi(a)|\Phi(0)\rangle, \tag{105}$$

where the shift $\mathbf{a}$ can be evaluated only along one axis, for example $\mathbf{a} = (0, 0, a)$. When we calculate the norm and Hamiltonian overlaps, we find them to be essentially Gaussian over a wide range of displacements $\mathbf{a}$, see Fig. 48. Similar formulas can be derived for the case of azimuthal symmetry, and furthermore, once the Gaussian character of the overlap is established, say using a few values of $\mathbf{a}$, one can simply use the standard expressions for Gaussian integrals rather than numerically evaluating the formulas above.

In addition to calculating the center of mass energy, we also calculated the center of mass kinetic energy, as well as the matter and charge RMS radii after performing the projection onto zero CoM momentum. We find rather small changes in the density distribution after performing the projection, which can be evaluated using

$$T_{CoM} = \langle\Psi_\mathbf{0}|\hat{\mathrm{T}}|\Psi_\mathbf{0}\rangle - \langle\Phi|\hat{\mathrm{T}}|\Phi\rangle, \tag{106}$$

$$\hat{n}(\mathbf{r}) = \sum_\sigma \psi^\dagger(\mathbf{r},\sigma)\psi(\mathbf{r},\sigma), \tag{107}$$

$$\Delta n(\mathbf{r}) = \langle\Psi_\mathbf{0}|\hat{n}(\mathbf{r})|\Psi_\mathbf{0}\rangle - \langle\Phi|\hat{n}(\mathbf{r})|\Phi\rangle, \tag{108}$$

$$(\Delta r_{ch,mat})^2 = \int d^3\mathbf{r}\,\mathbf{r}^2\Delta n(\mathbf{r}),\ \int d^3\mathbf{r}\Delta n(\mathbf{r}) \equiv 0. \tag{109}$$

In Table VI, we summarize our findings for magic nuclei ^{16}O, ^{40}Ca, ^{48}Ca, ^{90}Zr, ^{100}Sn, ^{132}Sn, and ^{208}Pb, where we display E_{CoM} (91), T_{CoM} (106), and the matter and charge distribution radii and their change before and after CoM projection as defined in Eq. (109). We also list the standard deviations for the norm and Hamiltonian overlaps, which are clearly Gaussian as a function of the offset $\mathbf{a}$, as we mentioned above. All calculations were performed using the SeaLL1 nuclear energy density functional [12], which provides one of the best descriptions of a rather wide range of nuclear properties across the nuclear chart, within density functional theory extended to include superfluid effects, while utilizing only seven parameters, each related to a well-known quantity in nuclear physics: equilibrium energy and density of homogenous nuclear matter, symmetry energy and its density dependence,

surface tension, and pairing and spin-orbit couplings, albeit without any symmetry and zero-point fluctuations corrections. These calculations were performed self-consistently within a cubic box large enough to fit each nucleus, and with a lattice constant $l = 1$ fm.

Using a different functional, Schmid and Grümmer [310] and Schmid and Reinhard [311] observed differences in the number densities for ^{16}O before and after the projection procedure for radii $r < 1.5$ fm approximately, which are comparable to what we obtain with our lattice constant $l = 1$ fm. These authors considered the charge form factor at momentum transfer $q > 2$ fm^{-1}, where the charge form factors change at the level 10^{-4} with respect to the maximum, which is consistent with what we present here.

Another approach which addresses similar problems as DFT is the nuclear many-body Schrödinger equation, in which the parameters of interparticle interactions are extracted from phenomenological investigations, which are in turn based on partial knowledge of the energy-dependence and partial wave decomposition of the cross sections, and which also incorporate some inferences from QCD extrapolated to low momenta below $\Lambda_{QCD} = 600 \ldots 1000$ MeV. There are a variety of drawbacks to this approach, often called "*ab initio*." (There are, of course, drawbacks to DFT as well.) In addition to the considerations just mentioned, one must often use a large number of parameters to describe the interparticle potentials, for example the two-nucleon interaction alone requires more than 20 parameters [322, 323]. And even with this large number of parameters, the binding energy calculated for ^{208}Pb deviates by about 200 MeV(!) [324] from the experimentally determined value, which is worse by about two orders of magnitude than the accuracy of phenomenological DFT models [12, 101, 118, 301] or the RMS of the liquid drop mass formula. Low energy microscopic approaches such as these *ab initio* methods cannot yet access interparticle separations less than the sum of the nucleon radii, thus less than roughly $\pi\hbar c/\Lambda_{QCD} = \mathcal{O}(1)$ fm. Significant efforts are being made to extend these methods to large momentum transfer, but these approaches are limited to very light nuclei so far [325, 326], but see also Refs [172, 316, 317]. One limitation of *ab initio* methods is that nucleon number densities, which are one-body operators, see Eq. (107), require the addition of complicated 2- and 3-body operators [326] derived from nuclear MBWFs, sometimes requiring multi-dimensional integrations over $3A$ coordinates, which can be extremely expensive and thus limits the applicability of these methods to rather light nuclei [327].

E. Conclusions

The first significant result we demonstrated in this paper is that the CoM energy constitutes a significant correction to the nuclear binding energy for all nuclei. We have furthermore demonstrated the dependence of the CoM energy on the nuclear mass. Due to other authors using different NEDFs, it is difficult to directly compare our results to those of others; however, it is notable that our estimate for E_{CoM} is consistently about 1 MeV larger in magnitude than all other results reported in the literature for medium- and large-mass nuclei. The translationally invariant many-body wave function leads to a more deeply bound nucleus than the mean field result, as demonstrated using Eq. (87) and the surrounding arguments. Another rather surprising result we presented here is that, although interparticle interactions must be accounted for when calculating the CoM energy, see Eq. (91), their contribution is in practice small in comparison to the contribution from the kinetic energy, with the exception of the lighter nuclei. This makes sense, as the nuclear surface plays a more significant role for light nuclei, and thus in these systems we expect the effects of finite range nucleon interactions to be enhanced.

We have thus argued that the Peierls and Yoccoz [298] prescription is the appropriate way to restore translational invariance and calculate the CoM energy correction to the nuclear binding energy. This approach is methodologically consistent with other approaches for symmetry restoration. It also also evaluates E_{CoM} using a translationally invariant MBWF, and so the energy is not contaminated with contributions from the excited states of the nucleus, in contrast to the widely used correction $-\left\langle \Phi \left| \frac{\hat{\mathbf{P}}^2_{CoM}}{2Am} \right| \Phi \right\rangle$. The PY approach also consistently leads to a more deeply bound nucleus when compared with this other commonly used approach for calculating the CoM energy.

XI. MULTINUCLEON TRANSFER REACTIONS IN LOW ENERGY HEAVY ION COLLISIONS USING THE ENHANCED GENERATOR COORDINATE METHOD

In this section, we very briefly present preliminary results concerning the application of the "enhanced" generator coordinate method (eGCM) [328] to the problem of multi-nucleon transfer reactions in low energy heavy ion collisions.

A. Introduction

Although time-dependent density functional theory (TDDFT) is a fully quantum mechanical many-body framework, when one investigates collective motion such as nuclear fission or heavy ion collisions within TDDFT, at the level of densities, the motion still appears semiclassical. This is a problem because it is known that quantum interference and entanglement can be crucial for the proper treatment of quantum dynamics, and so steps must be taken to incorporate the missing physics. It is expected that properly accounting for these effects will be crucial for the accurate description of, for example, the synthesis of superheavy elements in multinucleon transfer reactions [328].

It was recently demonstrated by A. Bulgac [328] that there exists an extension or enhancement of the generator coordinate method (GCM), which is a generic procedure for constructing a many-body wave function with certain desired properties by taking a suitable linear combination of other MBWFs, and which is used, for example, in the restoration of broken symmetries in many-body wave functions, see Sec. X. In the original GCM in nuclear physics due to Griffin and Wheeler [329], a set of (typically ground state) many-body wave functions is parameterized by some generator coordinate Q as $\Phi(\xi_1,\ldots,\xi_A|Q)$, and then the GCM many-body wave function is constructed according to

$$\Psi(\xi_1,\ldots,\xi_A) = \sum\!\!\!\!\!\!\int_Q f(Q)\Phi(\xi_1,\ldots,\xi_A|Q), \tag{110}$$

where $f(Q)$ is the weight function. The time-dependent extension of GCM, TDGCM, due to Reinhard *et al.* [330], introduced in 1983, replaces the ground state MBWFs $\Phi(\xi_1,\ldots,\xi_A|Q)$ with time dependent mean field wave functions $\Phi(\xi_1,\ldots,\xi_A|Q,t)$, which are now parameterized by both a generator coordinate and by time, with the hope that one might describe

large amplitude collective motion such as nuclear fission in this manner. The TDGCM many-body wave function then takes the form

$$\Psi(\xi_1, \ldots, \xi_A, t) = \sum\!\!\!\!\!\!\int_Q f(Q,t)\Phi(\xi_1, \ldots, \xi_A|Q,t), \tag{111}$$

and where now the weight function $f(Q,t)$ depends on time. Although this wave function has a more complex structure than the original GCM, the assumption on which this approach relies, and which Bulgac [328] argues is unjustifiable, is that these various trajectories are started simultaneously, and that no mixing between different times is allowed. The eGCM ansatz [328] for the many-body wave function starts again from a set of time-dependent mean field many-body wave functions $\Phi(\xi_1, \ldots, \xi_A|Q,t)$ as in TDGCM, but one then promotes the time coordinate to the status of another generator coordinate, in which case the many-body wave function takes on the form

$$\Psi_{\text{eGCM}}(\xi_1, \ldots, \xi_A) = \sum\!\!\!\!\!\!\int_{Q,\tau} f(Q,\tau)\Phi(\xi_1, \ldots, \xi_A|Q,\tau). \tag{112}$$

Mixing is therefore allowed between states at different times, and as we show in the preliminary results in the next section, this mixing does indeed occur for the problem of low energy heavy ion collisions. To determine the weight function, we solve the eGCM equations, which are given by

$$\sum\!\!\!\!\!\!\int_{Q',\tau'} \langle\Phi(Q,\tau)|\hat{H}|\Phi(Q',\tau')\rangle f(Q',\tau') = E \sum\!\!\!\!\!\!\int_{Q',\tau'} \langle\Phi(Q,\tau)|\Phi(Q',\tau')\rangle f(Q',\tau'). \tag{113}$$

The eGCM equations therefore constitute a generalized eigenvalue problem, for which the norm overlap matrix

$$\langle\Phi(Q,\tau)|\Phi(Q',\tau')\rangle \tag{114}$$

and the Hamiltonian overlap matrix

$$\langle\Phi(Q,\tau)|\hat{H}|\Phi(Q',\tau')\rangle \tag{115}$$

must both be computed.

B. Results

To test the eGCM formalism, we ran time-dependent Hartree-Fock (TDHF) simulations of the collision of ^{48}Ca and ^{208}Pb at the energy 235 MeV, which is above the Coulomb

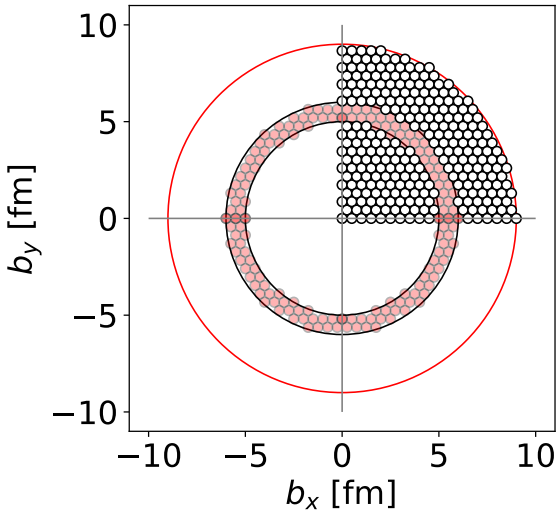

FIG. 49. The initial impact parameters for the low energy TDHF heavy ion collisions to which we are applying the eGCM technique. Red circles indicate runs included in the current dataset under consideration. White circles indicate a more general study to be undertaken in the future. Dark red circles indicate points where redundancy could have occurred under reflections, and which we therefore took care to only include once.

barrier, in the COM frame at a variety of impact parameters, which are arranged as shown in Fig. 49. These initial impact parameters serve the role of the Q generator coordinates for this problem, with $Q = (b_x, b_y)$. The Slater determinant wave functions are saved every 32 fm/c during the TDHF time evolution, and from these wave functions we have so far calculated the eGCM norm overlap matrix, see Eq. (114). The matrix elements for the proton norm overlap matrix are shown in Fig. 50, where there is clearly considerable mixing between states evaluated at different times, as indicated by the many nonzero matrix elements located in blocks off the block diagonal of the matrix, see also the caption of Fig. 50.

We diagonalized the eGCM overlap matrix, and also the TDGCM overlap matrix for comparison, which one obtains by only including nonzero matrix elements in Eq. (114) when $\tau = \tau'$. The eigenvalue spectra look essentially indistinguishable, see Fig. 51. Nevertheless, although the eigenvalues of the norm overlap matrix are visually indistinguishable, the eigenvectors tell a very different story. The degree of localization of a single-particle wave

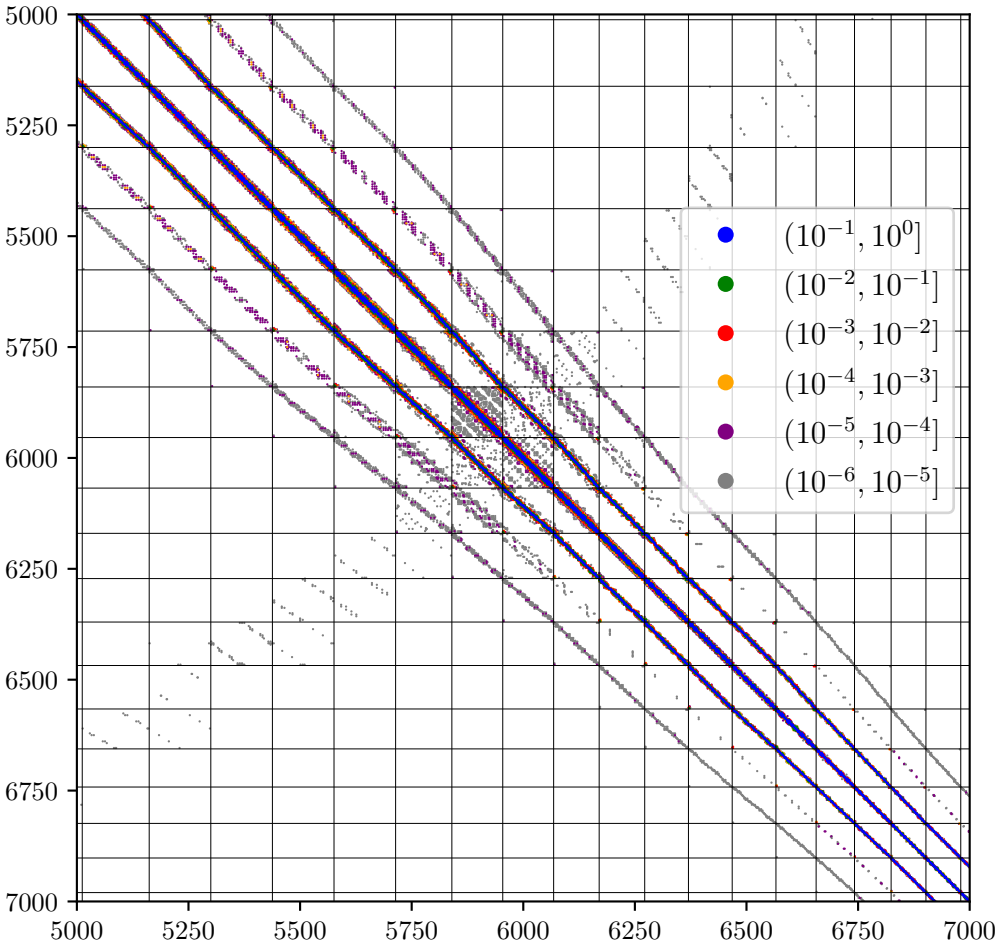

FIG. 50. The proton norm overlap matrix, zoomed in on the region where many of the colliding nuclei are in "orbiting" configurations and nearing separation. Each block, bordered by thin lines, represents a set of overlaps $\{\langle\Phi(Q,\tau)|\Phi(Q',\tau')\rangle\}_{Q,Q'}$, where $\tau \neq \tau'$, except for the blocks on the diagonal. Note that in the case of TDGCM as it is usually presented, only the diagonal blocks would be contain non-zero elements, but considerable off-diagonal matrix elements are clearly present.

function can be assessed by way of the inverse participation ratio (IPR), which is given by

$$\mathrm{IPR}(\psi) = \sum_i |\psi_i|^4. \tag{116}$$

For a fully delocalized state on a lattice containing N points, it will be the case that IPR = $1/N$, where for a fully localized state, we will have IPR = 1. In the case of TDGCM, the IPR is generally an order of magnitude larger because by construction TDGCM never allows for the superposition of states at different times. Given that the initial conditions

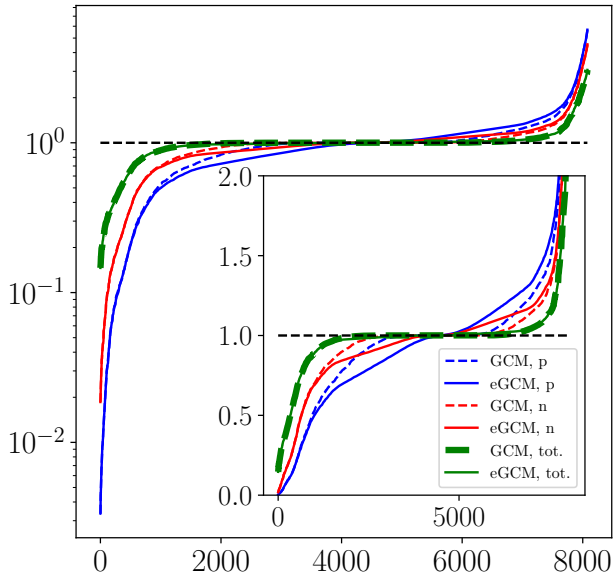

FIG. 51. Eigenvalue spectra of the eGCM norm overlap matrix and TDGCM norm overlap matrix for comparison, for protons, neutrons, and the total.

for this dataset consist of 152 impact parameters arranged in a ring, at most the TDGCM eigenfunctions can be a superposition of 152 states, corresponding to a minimum IPR of 1/152. For eGCM by contrast, the eigenstates are considerably more delocalized, involving superpositions over a much larger set of states at different times. The minimum possible value of the IPR for eGCM would be a uniform superposition of all MBWFs in our dataset, corresponding to IPR = 1/8078. In Fig. 52, we see that the eGCM IPR is generally much lower than it is for the case of TDGCM, indicating that eGCM eigenstates will be much more delocalized than the standard TDGCM case.

Although these results have only been obtained so far for the norm overlap matrix, they provide a convincing argument that the full weight functions, $f(Q, \tau)$, obtained by solving the eGCM equations, will also display a great deal of mixing between states at different times, which indicates that this mixing must be allowed for a proper treatment of the problem of low energy heavy ion collisions, and very probably also for the case of nuclear fission dynamics as well.

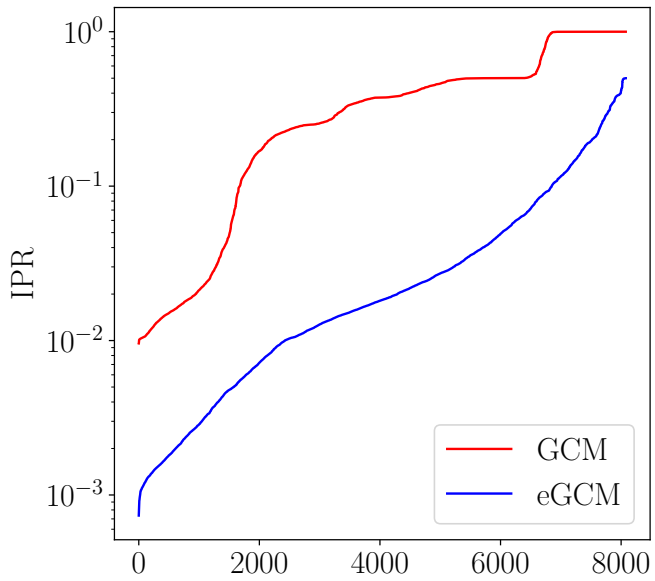

FIG. 52. The inverse participation ratio (IPR) for the eigenvectors of the norm overlap matrix calculated within eGCM and within TDGCM for comparison, showing a dramatically larger degree of delocalization for the case of eGCM.

---

[1] Matthew Kafker and Xerxes D. Arsiwalla, "Nonequilibrium dynamics of hard spheres in the fluid, crystalline, and glassy regimes," Phys. Rev. E **112**, 034103 (2025).

[2] Aurel Bulgac, Ibrahim Abdurrahman, Matthew Kafker, and Ionel Stetcu, "Time-dependent density functional theory description of ^{238}U(n, f), ^{240,242}Pu(n, f), and ^{237}Np(n, f) reactions," Phys. Rev. Lett. **135**, 062501 (2025).

[3] Matthew Kafker and Aurel Bulgac, "Impact of the center of mass fluctuations on the ground state properties of nuclei," (2025), arXiv:2503.09470 [nucl-th].

[4] Bulgac, Aurel, Kafker, Matthew, Abdurrahman, Ibrahim, and Stetcu, Ionel, "Non-equilibrium aspects of fission dynamics within the time dependent density functional theory," EPJ Web Conf. **322**, 07002 (2025).

[5] Aurel Bulgac, Matthew Kafker, Ibrahim Abdurrahman, and Gabriel Wlazłowski, "Quantum turbulence, superfluidity, non-markovian dynamics, and wave function thermalization," Phys. Rev. Res. **6**, L042003 (2024).

[6] Ibrahim Abdurrahman, Matthew Kafker, Aurel Bulgac, and Ionel Stetcu, "Neck rupture and scission neutrons in nuclear fission," Physical review letters **132**, 242501 (2024).

[7] A. Bulgac, M. Kafker, I. Abdurrahman, and I. Stetcu, "Non-Markovian character and irreversibility of real-time quantum many-body dynamics," Phys. Rev. C **109**, 064617 (2024).

[8] Abdurrahman, Ibrahim, Kafker, Matthew, Bulgac, Aurel, and Stetcu, Ionel, "Microscopic evidence for scission neutrons," EPJ Web Conf. **292**, 08008 (2024).

[9] Guillaume Scamps, Ibrahim Abdurrahman, Matthew Kafker, Aurel Bulgac, and Ionel Stetcu, "Spatial orientation of the fission fragment intrinsic spins and their correlations," Phys. Rev. C **108**, L061602 (2023).

[10] Aurel Bulgac, Matthew Kafker, and Ibrahim Abdurrahman, "Measures of complexity and entanglement in many-fermion systems," Phys. Rev. C **107**, 044318 (2023).

[11] P. Ring and P. Schuck, *The Nuclear Many-Body Problem*, 1st ed. (Springer-Verlag, Berlin Heidelberg New York, 2004).

[12] A. Bulgac, M. M. Forbes, S. Jin, R. Navarro Perez, and N. Schunck, "Minimal nuclear energy density functional," Phys. Rev. C **97**, 044313 (2018).

[13] P. Hohenberg and W. Kohn, "Inhomogeneous Electron Gas," Phys. Rev. **136**, B864 (1964).

[14] D. Vautherin and D. M. Brink, "Hartree-Fock Calculations with Skyrme's Interaction. I. Spherical Nuclei," Phys. Rev. C **5**, 626 (1972).

[15] G. Bertsch, "The nuclear density of states in the space of nuclear shapes," Phys. Lett. B **95**, 157 (1980).

[16] G. F. Bertsch, F. Barranco, and R. A. Broglia, "Windsurfing the Fermi sea: Proceedings of the international conference and symposium on unified concepts of many-body problems held at the state university of new york, stony brook, september 4-6, 1986 in honor of gerry brown's 60th birthday," in *Windsurfing the Fermi Sea: Proceedings of the International Conference and Symposium on Unified Concepts of Many-Body Problems held at the State University of New York, Stony Brook, September 4-6, 1986 in honor of Gerry Brown's 60th birthday*, edited by T. T. S. Kuo and J. Speth (North-Holland, Amsterdam, 1987) p. 33.

[17] F. Barranco, G.F. Bertsch, R.A. Broglia, and E. Vigezzi, "Large-amplitude motion in superfluid Fermi droplets," Nucl. Data Sheets Phys. A **512**, 253 (1990).

[18] F. Barranco, R. A. Broglia, and G. F. Bertsch, "Exotic radioactivity as a superfluid tunneling phenomenon," Phys. Rev. Lett. **60**, 50 (1988).

[19] G. F. Bertsch and A. Bulgac, "Comment on "spontaneous fission: A kinetic approach"," Phys. Rev. Lett. **79**, 3539 (1997).

[20] J. Bardeen, L. N. Cooper, and J. R. Schrieffer, "Theory of superconductivity," Phys. Rev. **108**, 1175 (1957).

[21] S. Jin, K. J. Roche, I. Stetcu, I. Abdurrahman, and A. Bulgac, "The LISE package: solvers for static and time-dependent superfluid local density approximation equations in three dimentions," Comp. Phys. Comm. **269**, 108130 (202).

[22] A. Bulgac and Y. Yu, "Renormalization of the Hartree-Fock-Bogoliubov Equations in the Case of a Zero Range Pairing Interaction," Phys. Rev. Lett. **88**, 042504 (2002).

[23] A. Bulgac, "Local density approximation for systems with pairing correlations," Phys. Rev. C **65**, 051305 (2002).

[24] O. Hahn and F. Strassmann, "Über den Nachweis und das Verhalten der bei der Bestrahlung des Urans mittels Neutronen entstehenden Erdalkalimetalle," Naturwissenschaften **27**, 11 (1939).

[25] L. Meitner, L. and O. R. Frisch, "Disintegration of Uranium by Neutrons: a New Type of Nuclear Reaction," Nature **143**, 239 (1939).

[26] F. Gönnenwein, "Neutron and Gamma Emission in Fission, https://t2.lanl.gov/fiesta2014/school.shtml,".

[27] N. Bohr, "Neutron Capture and Nuclear Constitution," Nature **137**, 344 and 351 (1936).

[28] W. Ryssens, P.-H. Heenen, and M. Bender, "Numerical accuracy of mean-field calculations in coordinate space," Phys. Rev. C **92**, 064318 (2015).

[29] A. Bulgac, P. Magierski, K. J. Roche, and I. Stetcu, "Induced Fission of ^{240}Pu within a Real-Time Microscopic Framework," Phys. Rev. Lett. **116**, 122504 (2016).

[30] A. Bulgac, S. Jin, K. J. Roche, N. Schunck, and I. Stetcu, "Fission dynamics of ^{240}Pu from saddle to scission and beyond," Phys. Rev. C **100**, 034615 (2019).

[31] A. Bulgac, S. Jin, and I. Stetcu, "Nuclear Fission Dynamics: Past, Present, Needs, and Future," Frontiers in Physics **8**, 63 (2020).

[32] A. Bulgac, I. Abdurrahman, S. Jin, K. Godbey, N. Schunck, and I. Stetcu, "Fission fragment intrinsic spins and their correlations," Phys. Rev. Lett. **126**, 142502 (2021).

[33] J. K. Krappe and K. Pomorski, *Theory of Nuclear Fission* (Springer Heidelberg, 2012).

[34] N. Schunck and L. M. Robledo, "Microscopic theory of nuclear fission: a review," Rep. Prog.

Phys. **79**, 116301 (2016).

[35] M. Bender and *et al.*, "Future of nuclear fission theory," J. Phys. G: Nucl. Part. Phys. **47**, 113002 (2020).

[36] A. J. Sierk, "Langevin model of low-energy fission," Phys. Rev. C **96**, 034603 (2017).

[37] M. Verriere, N. Schunck, and D. Regnier, "Microscopic calculation of fission product yields with particle-number projection," Phys. Rev. C **103**, 054602 (2021).

[38] M. R. Mumpower, P. Jaffke, M. Verriere, and J. Randrup, "Primary fission fragment mass yields across the chart of nuclides," Phys. Rev. C **101**, 054607 (2020).

[39] F. A. Ivanyuk, C. Ishizuka, and S. Chiba, "Five-dimensional Langevin approach to fission of atomic nuclei," Phys. Rev. C **109**, 034602 (2024).

[40] J. Sadhukhan, W. Nazarewicz, and N. Schunck, "Microscopic modeling of mass and charge distributions in the spontaneous fission of ^{240}pu," Phys. Rev. C **93**, 011304 (2016).

[41] J. Sadhukhan, C. Zhang, W. Nazarewicz, and N. Schunck, "Formation and distribution of fragments in the spontaneous fission of ^{240}Pu," Phys. Rev. C **96**, 061301 (2017).

[42] D. L. Hill and J. A. Wheeler, "Nuclear Constitution and the Interpretation of Fission Phenomena," Phys. Rev. **89**, 1102 (1953).

[43] J. J. Griffin and J. A. Wheeler, "Collective Motions in Nuclei by the Method of Generator Coordinates," Phys. Rev. **108**, 311 (1957).

[44] P.-G. Reinhard, R.Y. Cusson, and K. Goeke, "Time evolution of coherent ground-state correlations and the TDHF approach," Nucl. Phys. A **398**, 141 (1983).

[45] A. Bulgac, S. Jin, and I. Stetcu, "Unitary evolution with fluctuations and dissipation," Phys. Rev. C **100**, 014615 (2019).

[46] A. Bulgac, "Pure quantum extension of the semiclassical Boltzmann-Uehling-Uhlenbeck equation," Phys. Rev. C **105**, L021601 (2022).

[47] U. Brosa, S. Grossmann, and A. Müller, "Nuclear scission," Physics Reports **197**, 167 (1990).

[48] S. Oberstedt, F.-J. Hambsch, and F. Vivès, "Fission-mode calculations for 239U, a revision of the multi-modal random neck-rupture model," Nuclear Physics A **644**, 289–305 (1998).

[49] R. Vogt, J. Randrup, J. Pruet, and W. Younes, "Event-by-event study of prompt neutrons from ^{239}Pu(n, f)," Phys. Rev. C **80**, 044611 (2009).

[50] B. Becker, P. Talou, T. Kawano, Y. Danon, and I. Stetcu, "Monte Carlo Hauser-Feshbach predictions of prompt fission γ rays: Application to $n_{\rm th} + ^{235}$U, $n_{\rm th} + ^{239}$Pu, and ^{252}Cf (sf),"

Phys. Rev. C **87**, 014617 (2013).

[51] P. Talou, I. Stetcu, P. Jaffke, M. E. Rising, A. E. Lovell, and T. Kawano, "Fission fragment decay simulations with the CGMF code," Comput. Phys. Commun. **269**, 108087 (2021).

[52] Olivier Litaize, Olivier Serot, David Regnier, StŽphane Theveny, and SŽbastien Onde, "New Features of the FIFRELIN Code for the Investigation of Fission Fragments Characteristics," Physics Procedia **31**, 51 (2012), gAMMA-1 Emission of Prompt Gamma-Rays in Fission and Related Topics.

[53] A. E. Lovell, T. Kawano, S. Okumura, I. Stetcu, M. R. Mumpower, and P. Talou, "Extension of the hauser-feshbach fission fragment decay model to multichance fission," Phys. Rev. C **103**, 014615 (2021).

[54] K. Fujio, A. Al-Adili, F. Nordström, J.-F. Lemaître, S. Okumura, S. Chiba, and A. Koning, "TALYS calculations of prompt fission observables and independent fission product yields for the neutron-induced fission of ^{235}U," The European Physical Journal A **59**, 178 (2023).

[55] T. Najumunnisa, M. M. Musthafa, C. V. Midhun, Muhammed Aslam, K. K. Rajesh, P. Surendran, J. P. Nair, A. Shanbhag, and S. Ghugre, "^{105}Rh yield from the proton induced fission of uranium," Nuclear Physics A **1032**, 122611 (2023).

[56] B. D. Wilkins, E. P. Steinberg, and R. R. Chasman, "Scission-point model of nuclear fission based on deformed-shell effects," Phys. Rev. C **14**, 1832 (1976).

[57] J.-F. Lemaître, S. Panebianco, J.-L. Sida, S. Hilaire, and S. Heinrich, "New statistical scission-point model to predict fission fragment observables," Phys. Rev. C **92**, 034617 (2015).

[58] J.-F. Lemaître, S. Goriely, A. Bauswein, and H.-T. Janka, "Fission fragment distributions and their impact on the r-process nucleosynthesis in neutron star mergers," Phys. Rev. C **103**, 025806 (2021).

[59] J. Randrup and P. Möller, "Brownian Shape Motion on Five-Dimensional Potential-Energy Surfaces:Nuclear Fission-Fragment Mass Distributions," Phys. Rev. Lett. **106**, 132503 (2011).

[60] M. Albertsson, B.G. Carlsson, T. Døssing, P. Möller, J. Randrup, and S. Åberg, "Excitation energy partition in fission," Phys. Lett. B **803**, 135276 (2020).

[61] M. Verriere and M. R. Mumpower, "Improvements to the macroscopic-microscopic approach of nuclear fission," Phys. Rev. C **103**, 034617 (2021).

[62] N. Bohr and J. A. Wheeler, "The Mechanism of Nuclear Fission," Phys. Rev. **56**, 426–450 (1939).

[63] R. Vandenbosch and J. R. Huizenga, "Nuclear Fission," Academic Press, New York (1973).

[64] H. J. Rose and G. A. Jones, "A new kind of natural radioactivity," Nature **307**, 245 (1984).

[65] C. Wagemans, ed., *The Nuclear Fission Process* (CRC Press, Boca Raton, 1991).

[66] A. Bulgac, I. Abdurrahman, and G. Wlazłowski, "Sensitivity of time-dependent density functional theory to initial conditions," Phys. Rev. C **105**, 044601 (2022).

[67] A. Bulgac, "Time-Dependent Density Functional Theory for Fermionic Superfluids: from Cold Atomic gases, to Nuclei and Neutron Star Crust," Physica Status Solidi B **256**, 1800592 (2019).

[68] P. Mädler, "Catapult mechanism for fast particle emission in fission and heavy ion reactions," Z. Physik A **321**, 343 (1985).

[69] R. Capote, "Private communication," (2023).

[70] M. Schulc, M. Kostal, R. Capote, J. Simon, T. Czakoj, and E. Novak, "Spectral averaged cross sections as a probe to a high energy tail of 235u pfns," EPJ Web of Conf. **284**, 04021 (2023).

[71] D. A. Brown, M. B. Chadwick, R. Capote, A. C. Kahler, A. Trkov, M. W. Herman, A. A. Sonzogni, Y. Danon, A. D. Carlson, M. Dunn, *et al.*, "ENDF/B-VIII. 0: the 8th major release of the nuclear reaction data library with CIELO-project cross sections, new standards and thermal scattering data," Nuclear Data Sheets **148**, 1–142 (2018).

[72] M. Rizea, V. Ledoux, M. V. Daele, G. V. Berghe, and N. Carjan, "Finite difference approach for the two-dimensional Schrödinger equation with application to scission-neutron emission," Comp. Phys. Comm. **179**, 466 (2008).

[73] N. Carjan and M. Rizea, "Scission neutrons and other scission properties as function of mass asymmetry in U 235 (n_{th}, f)," Phys. Rev. C. **82**, 014617 (2010).

[74] N. Carjan and M. Rizea, "Similarities between calculated scission-neutron properties and experimental data on prompt fission neutrons," Phys. Lett. B. **747**, 178 (2015).

[75] R. Capote, Y.-J. Chen, F.-J. Hambsch, N.V. Kornilov, J.P. Lestone, O. Litaize, B. Morillon, D. Neudecker, S. Oberstedt, T. Ohsawa, N. Otuka, V.G. Pronyaev, A. Saxena, O. Serot, O.A. Shcherbakov, N.-C. Shu, D.L. Smith, P. Talou, A. Trkov, A.C. Tudora, R. Vogt, and A.S. Vorobyev, "Prompt Fission Neutron Spectra of Actinides," Nuclear Data Sheets **131**, 1 (2016), special Issue on Nuclear Reaction Data.

[76] N. Carjan and M. Rizea, "Structures in the energy distribution of the scission neutrons: Finite

neutron-number effect," Phys. Rev. C **99**, 034613 (2019).

[77] R. R. Wilson, "Directional Properties of Fission Neutrons," Phys. Rev. **72**, 189 (1947).

[78] S. Debenedetti, J. E. Francis, W. M. Preston, and T. W. Bonner, "Angular Dependence of Coincidences between Fission Neutrons," Phys. Rev. **74**, 1645 (1948).

[79] V. S. Stavinsky, "On the emission mechanism of prompt fission neutrons," JETP (Soviet Physics) **9**, 437 (1959).

[80] R. W. Fuller, "Dependence of neutron production in fission on rate of change of nuclear potential," Phys. Rev. **126**, 684 (1962).

[81] H. R. Bowman, S. G. Thompson, J. C. D. Milton, and W. J. Swiatecki, "Velocity and angular distributions of prompt neutrons from spontaneous fission of Cf 252," Phys. Rev. **126**, 2120 (1962).

[82] S. S. Kapoor, R. Ramanna, and P. N. Rama Rao, "Emission of prompt neutrons in the thermal neutron fission of U 235," Phys. Rev. **131**, 283 (1963).

[83] K. Skarsvåg and K. Bergheim, "Energy and angular distributions of prompt neutrons from slow neutron fission of U235," Nuclear Physics **45**, 72 (1963).

[84] A. Gavron and Z. Fraenkel, "Neutron correlations in spontaneous fission of ^{252}Cf," Phys. Rev. C **9**, 632–645 (1974).

[85] Y. Boneh and Z. Fraenkel, "Dynamic single-particle effects in fission," Phys. Rev. C **10**, 893 (1974).

[86] J. S. Pringle and F. D. Brooks, "Angular Correlation of Neutrons from Spontaneous Fission of Cf 252," Phys. Rev. Lett. **35**, 1563 (1975).

[87] C. B. Franklyn, C. Hofmeyer, and D. W. Mingay, "Angular correlation of neutrons from thermal-neutron fission of 235U," Phys. Lett. B **78**, 564 (1978).

[88] C. B. Franklyn, "Neutron-fragment angular correlations in 235U (n_{th}, f)," Radiation Effects **92**, 323 (1986).

[89] C. Budtz-Jørgensen and H.-H. Knitter, "Simultaneous investigation of fission fragments and neutrons in 252Cf (SF)," Nuclear Physics A **490**, 307 (1988).

[90] B. Milek, R. Reif, and J. Revai, "Model for particle emission from a fissioning system," Phys. Rev. C **37**, 1077 (1988).

[91] M. S. Samant, R. P. Anand, R. K. Choudhury, S. S. Kapoor, and D. M. Nadkarni, "Prescission neutron emission in ^{235}U(n_{th},f) through fragment-neutron angular correlation studies," Phys.

Rev. C **51**, 3127 (1995).

[92] J. K. Hwang *et al.*, "Search for scission neutrons in the spontaneous fission of ^{252}Cf," Phys. Rev. C **60**, 044616 (1999).

[93] N. Carjan, P. Talou, and O. Serot, "Emission of scission neutrons in the sudden approximation," Nuclear Physics A **792**, 102 (2007).

[94] R. Capote, N. Carjan, and S. Chiba, "Scission neutrons for U, Pu, Cm, and Cf isotopes: Relative multiplicities calculated in the sudden limit," Phys. Rev. C **93**, 024609 (2016).

[95] I. S. Guseva, A. M. Gagarski, V. E. Sokolov, G. A. Petrov, A. S. Vorobyev, G. V. Val'sky, and T. A. Zavarukhina, "Detailed investigations of neutron–neutron angular correlations in slow-neutron-induced fission of 233 U, 235 U, and 239 Pu," Phys. Atom. Nuclei **81**, 447 (2018).

[96] A. S. Vorobyev, O. A. Shcherbakov, A. M. Gagarski, G. A. Petrov, G. V. Val'ski, and T. E. Kuz'mina, "Estimation of the Yield of "Scission" Neutrons from Thermal Neutron-Induced Fission of 239 Pu," J. Exp. Theor. Phys. **127**, 659 (2018).

[97] M. Born and R. Oppenheimer, "Zur Quantentheorie der Molekeln," Annalen der Physik **389**, 457 (1927).

[98] J. C. Tully, "Molecular dynamics with electronic transitions," J. Chem. Phys. **93**, 1061 (1990).

[99] H. A. Bethe, "An Attempt to Calculate the Number of Energy Levels of a Heavy Nucleus," Phys. Rev. **50**, 332–341 (1936).

[100] A. Bohr and B. R. Mottelson, *Nuclear Structure*, Vol. I (Benjamin Inc., New York, 1969).

[101] M. Bender, P.-H. Heenen, and P.-G. Reinhard, "Self-consistent mean-field models for nuclear structure," Rev. Mod. Phys. **75**, 121 (2003).

[102] Shi Jin, Kenneth J. Roche, Ionel Stetcu, Ibrahim Abdurrahman, and Aurel Bulgac, "The lise package: Solvers for static and time-dependent superfluid local density approximation equations in three dimensions," Computer Physics Communications **269**, 108130 (2021).

[103] A.O Caldeira and A.J Leggett, "Quantum tunnelling in a dissipative system," Ann. Phys. **149**, 374 (1983).

[104] D. E. Lyubashevsky, J. D. Shcherbina, and S. G. Kadmensky, "Quantum nature of p-even t-odd asymmetries in differential cross sections of fission reactions of unpolarized target nuclei by cold polarized neutrons with escape of prescission and evaporation of light particles," Phys. Rev. C **111**, 024609 (2025).

[105] G. Bertsch and H. Flocard, "Pairing effects in nuclear collective motion: Generator coordinate

method," Phys. Rev. C **43**, 2200 (1991).

[106] G.F. Bertsch, "Large amplitude collective motion," Nuclear Physics A **574**, 169 – 183 (1994).

[107] S. Perez-Martin and L. M. Robledo, "Microscopic justification of the equal filling approximation," Phys. Rev. C **78**, 014304 (2008).

[108] N. Schunck, M. Verriere, G. Potel Aguilar, R. C. Malone, J. A. Silano, A. P. D. Ramirez, and A. P. Tonchev, "Microscopic calculation of fission product yields for odd-mass nuclei," Phys. Rev. C **107**, 044312 (2023).

[109] J. L. Pore, W. Younes, J. M. Gates, L. M. Robledo, F. H. Garcia, R. Orford, H. L. Crawford, P. Fallon, J. A. Gooding, M. Kireeff Covo, M. McCarthy, and M. A. Stoyer, "Spontaneous fission of the odd-Z isotope ^{255}Db," Phys. Rev. C **110**, L041301 (2024).

[110] A. Bulgac, "Time-Dependent Density Functional Theory and the Real-Time Dynamics of Fermi Superfluids," Ann. Rev. Nucl. and Part. Sci. **63**, 97 (2013).

[111] George Bertsch, Jacek Dobaczewski, Witold Nazarewicz, and Junchen Pei, "Hartree-fock-bogoliubov theory of polarized fermi systems," Phys. Rev. A **79**, 043602 (2009).

[112] A. Bulgac, I. Abdurrahman, K. Godbey, and I. Stetcu, "Fragment Intrinsic Spins and Fragments' Relative Orbital Angular Momentum in Nuclear Fission," Phys. Rev. Lett. **128**, 022501 (2022).

[113] G. Scamps, I. Abdurrahman, M. Kafker, A. Bulgac, and I. Stetcu, "Spatial orientation of the fission fragment intrinsic spins and their correlations," Phys. Rev. C **108**, L061602 (2023).

[114] D.G. Madland, "Total prompt energy release in the neutron-induced fission of 235U, 238U, and 239Pu," Nucl. Phys. A **772**, 113 (2006).

[115] P. Talou, I. Stetcu, P. Jaffke, M.E. Rising, A.E. Lovell, and T. Kawano, "Fission fragment decay simulations with the CGMF code," Computer Physics Communications **269**, 108087 (2021).

[116] Aurel Bulgac, "Pre-equilibrium neutron emission in fission or fragmentation," Phys. Rev. C **102**, 034612 (2020).

[117] L. Zurek, S. K. Bogner, R. J. Furnstahl, R. Navarro Pérez, N. Schunck, and A. Schwenk, "Optimized nuclear energy density functionals including long-range pion contributions," Phys. Rev. C **109**, 014319 (2024).

[118] G. Grams, W. Ryssens, G. Scamps, S. Goriely, and N. Chamel, "Skyrme-Hartree-Fock-Bogoliubov mass models on a 3D mesh: III. From atomic nuclei to neutron stars," The

European Physical Journal A **59**, 270 (2023).

[119] J. N. Wilson, D. Thisse, M. Lebois, N. Jovancevic, D. Gjestvang, R. Canavan, M. Rudigier, D. Etasse, R-B. Gerst, L. Gaudefroy, E. Adamska, P. Adsley, A. Algora, M. Babo, K. Belvedere, J. Benito, G. Benzoni, A. Blazhev, A. Boso, S. Bottoni, M. Bunce, R. Chakma, N. Cieplicka-Orynczak, S. Courtin, M. L. Cortes, P. Davies, C. Delafosse, M. Fallot, B. Fornal, L. Fraile, A. Gottardo, V. Guadilla, G. Hafner, K. Hauschild, M. Heine, C. Henrich, I. Homm, F. Ibrahim, Ł. W. Iskra, P. Ivanov, S. Jazrawi, A. Korgul, P. Koseoglou, T. Kroll, T. Kurtukian-Nieto, L. Le Meur, S. Leoni, J. Ljungvall, A. Lopez-Martens, R. Lozeva, I. Matea, K. Miernik, J. Nemer, S. Oberstedt, W. Paulsen, M. Piersa, Y. Popovitch, C. Porzio, L. Qi, D. Ralet, P. H. Regan, K. Rezynkina, V. Sanchez-Tembleque, S. Siem, C. Schmitt, P. A. Soderstrom, C. Surder, G. Tocabens, V. Vedia, D. Verney, N. Warr, B. Wasilewska, J. Wiederhold, M. Yavahchova, F. Zeiser, and S. Ziliani, "Angular momentum generation in nuclear fission," Nature **590**, 566 (2021).

[120] J. B. Wilhelmy, E. Cheifetz, R. C. Jared, S. G. Thompson, H. R. Bowman, and J. O. Rasmussen, "Angular Momentum of Primary Products Formed in the Spontaneous Fission of ^{252}Cf," Phys. Rev. C **5**, 2041 (1972).

[121] A. Wolf and E. Cheifetz, "Angular distributions of specific gamma rays emitted in the deexcitation of prompt fission products of ^{252}Cf," Phys. Rev. C **13**, 1952 (1976).

[122] R. Vogt and J. Randrup, "Angular momentum effects in fission," Phys. Rev. C **103**, 014610 (2021).

[123] P. Marević, N. Schunck, J. Randrup, and R. Vogt, "Angular momentum of fission fragments from microscopic theory," Phys. Rev. C **104**, L021601 (2021).

[124] J. Randrup and R. Vogt, "Generation of Fragment Angular Momentum in Fission," Phys. Rev. Lett. **127**, 062502 (2021).

[125] I. Stetcu, A. E. Lovell, P. Talou, T. Kawano, S. Marin, S. A. Pozzi, and A. Bulgac, "Angular Momentum Removal by Neutron and γ-Ray Emissions during Fission Fragment Decays," Phys. Rev. Lett. **127**, 222502 (2021).

[126] A. Bulgac, "Angular correlation between the fission fragment intrinsic spins," Phys. Rev. C **106**, 014624 (2022).

[127] J. Randrup, "Coupled fission fragment angular momenta," Phys. Rev. C **106**, L051601 (2022).

[128] J. Randrup, T. Døssing, and R. Vogt, "Probing fission fragment angular momenta by photon

measurements," Phys. Rev. C **106**, 014609 (2022).

[129] G. Scamps, "Microscopic description of the torque acting on fission fragments," Phys. Rev. C **106**, 054614 (2022).

[130] G. Scamps and G. Bertsch, "Generation, dynamics, and correlations of the fission fragments' angular momenta," arXiv:2302.07792.

[131] Workshop on Fission Fragment Angular Momenta, Seattle, USA, June 21-24, (2022) (2022).

[132] R. Vogt and J. Randrup, "Event-by-event Modeling of Prompt Neutrons and Photons from Neutron-induced and Spontaneous Fission with FREYA," Physics Procedia **47**, 82 (2013), scientific Workshop on Nuclear Fission Dynamics and the Emission of Prompt Neutrons and Gamma Rays, Biarritz, France, 28-30 November 2012.

[133] J. Randrup and R. Vogt, "Calculation of fission observables through event-by-event simulation," Phys. Rev. C **80**, 024601 (2009).

[134] L. Sobotka, "Fragment spin generation in Fission: What we know, can't know, and should know. Gordon Research Conference, Colby Sawyer College, NH, June 11-16, 2023, *//cyclotron.tamu.edu/wp – content/uploads/sites/6/Fission_GRC_2023.pptx*," (2023).

[135] J. R. Nix and W. J. Swiatecki, "Studies in the liquid-drop theory of nuclear fission," Nucl. Phys. **71**, 1 (1965).

[136] L. G. Moretto and R. P. Schmitt, "Equilibrium statistical treatment of angular momenta associated with collective modes in fission and heavy-ion reactions," Phys. Rev. C **21**, 204 (1980).

[137] L. G. Moretto, G. F. Peaslee, and G. J. Wozniak, "Angular-Momentum-Bearing Modes in Fission," Nucl. Phys. A **502**, 453c (1989).

[138] D. A. Varshalovich, A. N. Moskalev, and V. K. Khersonskii, *Quantum Theory of Angular Momentum* (World Scientific, Singapore, 1989).

[139] L. M. Robledo, "Sign of the overlap of Hartree-Fock-Bogoliubov wave functions," Phys. Rev. C **79**, 021302 (2009).

[140] G. F. Bertsch and L. M. Robledo, "Symmetry Restoration in Hartree-Fock-Bogoliubov Based Theories," Phys. Rev. Lett. **108**, 042505 (2012).

[141] B. Bally and M. Bender, "Projection on particle number and angular momentum: Example of triaxial Bogoliubov quasiparticle states," Phys. Rev. C **103**, 024315 (2021).

[142] M. Wimmer, "Efficient Numerical Computation of the Pfaffian for Dense and Banded Skew-Symmetric Matrices," ACM Transactions on Mathematical Software **38**, 1 (2021).

[143] J. Randrup, "Theory of transfer-induced transport in nuclear collisions," Nuclear Physics A **327**, 490–516 (1979).

[144] J. Randrup, "Transport of angular momentum in damped nuclear reactions," Nuclear Physics A **383**, 468–508 (1982).

[145] P. Magierski, A. Makowski, M. C.. Barton, K. Sekizawa, and G. Wlazłowski, "Pairing dynamics and solitonic excitations in collisions of medium-mass, identical nuclei," Phys. Rev. C **105**, 064602 (2022).

[146] A. Bulgac, "Entropy, single-particle occupation probabilities, and short-range correlations," (2022), arXiv:2203.12079.

[147] C. W. Johnson, "Current Status of Very-Large-Basis Hamiltonian Diagonalizations for Nuclear Physics," (2018), arXiv:1809.07869.

[148] P.-O. Löwdin, "Quantum theory of cohesive properties of solids," Adv. Phys. **5**, 1 (1956).

[149] P.-O. Löwdin and H. Shull, "Natural orbitals in the quantum theory of two-electron systems," Phys. Rev. **101**, 1730–1739 (1956).

[150] N. N. Bogoliubov, "On a new method in the theory of superconductivity," Il Nuovo Cimento **7**, 794 (1958).

[151] J. G. Valatin, "Comments on the theory of superconductivity," Il Nuovo Cimento **7**, 843 (1958).

[152] P. G. De Gennes, *Superconductivity of Metals and Alloys* (CRC Press, Boca Raton, 1999).

[153] E. Schrödinger, "An Undulatory Theory of the Mechanics of Atoms and Molecules," Phys. Rev. **28**, 1049 (1926).

[154] D. R. Hartree, "The wave mechanics of an atom with a non-coulomb central field. part ii. some results and discussion," Mathematical Proceedings of the Cambridge Philosophical Society **24**, 111 (1928).

[155] J. C. Slater, "The self consistent field and the structure of atoms," Phys. Rev. **32**, 339 (1928).

[156] J. C. Slater, "Note on Hartree's Method," Phys. Rev. **35**, 210 (1930).

[157] V. Fock, "Näherungsmethode zur Lösung des quantenmechanischen Mehrkörperproblems," Zeitschrift für Physik **61**, 126 (1930).

[158] P. A. Anderson, *Basic Notions of Condensed Matter Physics* (Benjamin/Cummins Publishing

Company Inc. London, 1984).

[159] A. J. Coleman, "Structure of fermion density matrices," Rev. Mod. Phys. **35**, 668 (1963).

[160] A. J. Coleman, "Discussion on "structure of fermion density matrices"," Rev. Mod. Phys. **35**, 687 (1963).

[161] E. R. Davidson, "Properties and Uses of Natural Orbitals," Rev. Mod. Phys. **44**, 451 (1972).

[162] J. S. Levinger, "The High Energy Nuclear Photoeffect," Phys. Rev. **84**, 43 (1951).

[163] O. Benhar, V. R. Pandharipande, and S. C. Pieper, "Electron-scattering studies of correlations in nuclei," Rev. Mod. Phys. **65**, 817 (1993).

[164] V. R. Pandharipande, I. Sick, and P. K. A. deWitt Huberts, "Independent particle motion and correlations in fermion systems," Rev. Mod. Phys. **69**, 981 (1997).

[165] E. N. M. Quint, J. F. J. van den Brand, J. W. A. den Herder, E. Jans, P. H. M. Keizer, L. Lapikás, G. van der Steenhoven, P. K. A. de Witt Huberts, S. Klein, P. Grabmayr, G. J. Wagner, H. Nann, B. Frois, and D. Goutte, "Relative $3s$ Spectroscopic Strength in ^{206}Pb and ^{208}Pb Studied with the $(e, e^{'}p)$ Knockout Reaction," Phys. Rev. Lett. **57**, 186 (1986).

[166] E. N. M. Quint, B. M. Barnett, A. M. van den Berg, J. F. J. van den Brand, H. Clement, R. Ent, B. Frois, D. Goutte, P. Grabmayr, J. W. A. den Herder, E. Jans, G. J. Kramer, J. B. J. M. Lanen, L. Lapikás, H. Nann, G. van der Steenhoven, G. J. Wagner, and P. K. A. de Witt Huberts, "Evidence for partial occupancy of the $3s_{1/2}$ proton orbit in ^{208}Pb," Phys. Rev. Lett. **58**, 1088 (1987).

[167] T. Aumann, C. Barbieri, D. Bazin, C.A. Bertulani, A. Bonaccorso, W.H. Dickhoff, A. Gade, M. Gómez-Ramos, B.P. Kay, A.M. Moro, T. Nakamura, A. Obertelli, K. Ogata, S. Paschalis, and T. Uesaka, "Quenching of single-particle strength from direct reactions with stable and rare-isotope beams," Progress in Particle and Nuclear Physics **118**, 103847 (2021).

[168] B. D. Day, "Elements of the Brueckner-Goldstone Theory of Nuclear Matter," Rev. Mod. Phys. **39**, 719 (1967).

[169] J. W. Negele, "The mean-field theory of nuclear structure and dynamics," Rev. Mod. Phys. **54**, 913 (1982).

[170] R. Sartor and C. Mahaux, "Self-energy, momentum distribution, and effective masses of a dilute Fermi gas," Phys. Rev. C **21**, 1546 (1980).

[171] L.L. Frankfurt and M.I. Strikman, "High-energy phenomena, short-range nuclear structure and QCD," Phys. Rep. **76**, 215 (1981).

[172] L. Frankfurt and M. Strikman, "Hard nuclear processes and microscopic nuclear structure," Physics Reports **160**, 235 (1988).

[173] C. Ciofi degli Atti and S. Simula, "Realistic model of the nucleon spectral function in few- and many-nucleon systems," Phys. Rev. C **53**, 1689 (1996).

[174] E. Piasetzky, M. Sargsian, L. Frankfurt, M. Strikman, and J. W. Watson, "Evidence for Strong Dominance of Proton-Neutron Correlations in Nuclei," Phys. Rev. Lett. **97**, 162504 (2006).

[175] M. M. Sargsian, T. V. Abrahamyan, M. I. Strikman, and L. L. Frankfurt, "Exclusive electrodisintegration of ^{3}He at high Q^2. ii. decay function formalism," Phys. Rev. C **71**, 044615 (2005).

[176] R. Schiavilla, R. B. Wiringa, S. C. Pieper, and J. Carlson, "Tensor forces and the ground-state structure of nuclei," Phys. Rev. Lett. **98**, 132501 (2007).

[177] M. M. Sargsian, "New properties of the high-momentum distribution of nucleons in asymmetric nuclei," Phys. Rev. C **89**, 034305 (2014).

[178] O. Hen, G. A. Miller, E. Piasetzky, and L. B. Weinstein, "Nucleon-nucleon correlations, short-lived excitations, and the quarks within," Rev. Mod. Phys. **89**, 045002 (2017).

[179] W. Zwerger, ed., *The BCS–BEC Crossover and the Unitary Fermi Gas*, Lecture Notes in Physics, Vol. 836 (Springer-Verlag, Berlin Heidelberg, 2012).

[180] E. Braaten, "Universal Relations for Fermions with Large Scattering Length," (Springer, Berlin Heidelberg, 2012) Chap. 6, pp. 193–231.

[181] Y. Castin and F. Werner, "The Unitary Gas and its Symmetry Properties," (Springer, Berlin Heodelberg, 2012) Chap. 5.

[182] E. R. Anderson and J. E. Drut, "Pressure, compressibility, and contact of the two-dimensional attractive fermi gas," Phys. Rev. Lett. **115**, 115301 (2015).

[183] W. J. Porter and J. E. Drut, "Tan's contact and the phase distribution of repulsive Fermi gases: Insights from quantum chromodynamics noise analyses," Phys. Rev. A **95**, 053619 (2017).

[184] J. T. Stewart, J. P. Gaebler, T. E. Drake, and D. S. Jin, "Verification of Universal Relations in a Strongly Interacting Fermi Gas," Phys. Rev. Lett. **104**, 235301 (2010).

[185] O. Hen et al., "Momentum sharing in imbalanced Fermi systems," Science **346**, 614 (2014).

[186] R. Cruz-Torres, D. Lonardoni, R. Weiss, M. Piarulli, N. Barnea, D. W. Higinbotham, E. Pi-

asetzky, A. Schmidt, L. B. Weinstein, R. B. Wiringa, and O. Hen, "Many-body factorization and position–momentum equivalence of nuclear short-range correlations," Nature Physics **17**, 306 (2021).

[187] S. Tan, "Energetics of a strongly correlated Fermi gas," Ann. Phys. **323**, 2952 (2008).

[188] S. Tan, "Large momentum part of a strongly correlated Fermi gas," Ann. Phys. **323**, 2971 (2008).

[189] S. Tan, "Generalized virial theorem and pressure relation for a strongly correlated Fermi gas," Ann. Phys. **323**, 2987 (2008).

[190] L. W. Nordheim, "On the Kinetic Method in the New Statistics and its Application in the Electron Theory of Conductivity," Proc. Roy. Soc. (London) **A119**, 689 (1928).

[191] E. A. Uehling and G. E. Uhlenbeck, "Transport Phenomena in Einstein-Bose and Fermi-Dirac Gases. I," Phys. Rev. **43**, 552 (1933).

[192] I. Klich, "Lower entropy bounds and particle number fluctuations in a Fermi sea," Journal of Physics A: Mathematical and General **39**, L85 (2006).

[193] L. Amico, R. Fazio, A. Osterloh, and V. Vedral, "Entanglement in many-body systems," Rev. Mod. Phys. **80**, 517 (2008).

[194] R. Horodecki, P. Horodecki, M. Horodecki, and K. Horodecki, "Quantum entanglement," Rev. Mod. Phys. **81**, 865–942 (2009).

[195] M. Haque, O. S. Zozulya, and K. Schouten, "Entanglement between particle partitions in itinerant many-particle states," J. Phys. A Math. Theor. **42**, 504012 (2009).

[196] J. Eisert, M. Cramer, and M. B. Plenio, "Colloquium: Area laws for the entanglement entropy," Rev. Mod. Phys. **82**, 277–306 (2010).

[197] K. Boguslawski and P. Tecmer, "Orbital entanglement in quantum chemistry," Int. J. Quant. Chem. **115**, 1289 (2014).

[198] N. Gigena and R. Rossignoli, "Entanglement in fermion systems," Phys. Rev. A **92**, 042326 (2015).

[199] C. Robin, M. J. Savage, and N. Pillet, "Entanglement rearrangement in self-consistent nuclear structure calculations," Phys. Rev. C **103**, 034325 (2021).

[200] B. Zumino, "Normal Forms of Complex Matrices," J. Math. Phys. **3**, 1055 (1962).

[201] C. Bloch and A. Messiah, "The canonical form of an antisymmetric tensor and its application to the theory of superconductivity," Nucl. Phys. **39**, 95 (1962).

[202] V. R. Pandharipande, C. N. Papanicolas, and J. Wambach, "Occupation Probabilities of Shell-Model Orbits in the Lead Region," Phys. Rev. Lett. **53**, 1133 (1984).

[203] M. V. Stoitsov, A. N. Antonov, and S. S. Dimitrova, "Natural orbital representation and short-range correlations in nuclei," Phys. Rev. C **48**, 74 (1993).

[204] P.-G. Reinhard, M. Bender, K. Rutz, and J.A. Maruhn, "An HFB scheme in natural orbitals," Z. Phys. A **358**, 277 (1999).

[205] J. Dobaczewski, W. Nazarewicz, T. R. Werner, J. F. Berger, C. R. Chinn, and J. Dechargé, "Mean-field description of ground-state properties of drip-line nuclei: Pairing and continuum effects," Phys. Rev. C **53**, 2809–2840 (1996).

[206] N. Tajima, "Canonical-basis solution of the Hartree-Fock-Bogoliubov equation on a three-dimensional Cartesian mesh," Phys. Rev. C **69**, 034305 (2004).

[207] A. Tichai, J. Müller, K. Vobig, and R. Roth, "Natural orbitals for ab initio no-core shell model calculations," Phys. Rev. C **99**, 034321 (2019).

[208] J. Hoppe, A. Tichai, M. Heinz, K. Hebeler, and A. Schwenk, "Natural orbitals for many-body expansion methods," Phys. Rev. C **103**, 014321 (2021).

[209] P. J. Fasano, C. Constantinou, M. A. Caprio, P. Maris, and J. P. Vary, "Natural orbitals for the ab initio no-core configuration interaction approach," Phys. Rev. C **105**, 054301 (2022).

[210] M. Chen, T. Li, B. Schuetrumpf, P.-G. Reinhard, and W. Nazarewicz, "Three-dimensional Skyrme Hartree-Fock-Bogoliubov solver in coordinate-space representation," Comp. Phys. Comm. **276**, 108344 (2022).

[211] B. S. Hu, J. Padua-Argüelles, S. Leutheusser, T. Miyagi, S. R. Stroberg, and J. D. Holt, "Ab Initio Structure Factors for Spin-Dependent Dark Matter Direct Detection," Phys. Rev. Lett. **128**, 072502 (2022).

[212] G. Hagen, S. J. Novario, Z. H. Sun, T. Papenbrock, G. R. Jansen, J. G. Lietz, T. Duguet, and A. Tichai, "Angular-momentum projection in coupled-cluster theory: Structure of ^{34}Mg," Phys. Rev. C **105**, 064311 (2022).

[213] M. Kortelainen, Z. Sun, G. Hagen, W. Nazarewicz, T. Papenbrock, and P.-G. Reinhard, "Universal trend of charge radii of even-even Ca–Zn nuclei," Phys. Rev. C **105**, L021303 (2022).

[214] A. Tichai, S. Knecht, A. T. Kruppa, Ö. Legeza, C. P. Moca, A. Schwenk, M. A. Werner, and G. Zarand, "Combining the in-medium similarity renormalization group with the density

matrix renormalization group: Shell structure and information entropy," arXiv:2207.01438.

[215] A. Bulgac, "Local-density-functional theory for superfluid fermionic systems: The unitary Fermi gas," Phys. Rev. A **76**, 040502 (2007).

[216] A. Bulgac and M. M. Forbes, "Use of the discrete variable representation basis in nuclear physics," Phys. Rev. C **87**, 051301(R) (2013).

[217] A. Bulgac, "Hartree-Fock-Bogoliubov approximation for finite systems," (1980), arXiv:nucl-th/9907088.

[218] H. Li and F. D. M. Haldane, "Entanglement Spectrum as a Generalization of Entanglement Entropy: Identification of Topological Order in Non-Abelian Fractional Quantum Hall Effect States," Phys. Rev. Lett. **101**, 010504 (2008).

[219] R. Navarro Perez, N. Schunck, R.-D. Lasseri, C. Zhang, and J. Sarich, "Axially deformed solution of the Skyrme–Hartree–Fock–Bogolyubov equations using the transformed harmonic oscillator basis (III) HFBHTO (v3.00): A new version of the program," Comp. Phys. Comm. **220**, 363 (2017).

[220] P. Marević, N. Schunck, E.M. Ney, R. Navarro Pérez, M. Verriere, and J. O'Neal, "Axially-deformed solution of the Skyrme-Hartree-Fock-Bogoliubov equations using the transformed harmonic oscillator basis (IV) HFBTHO (v4.0): A new version of the program," Comp. Phys. Comm. **276**, 108367 (2022).

[221] I. Stetcu, A. Bulgac, P. Magierski, and K. J. Roche, "Isovector giant dipole resonance from the 3D time-dependent density functional theory for superfluid nuclei," Phys. Rev. C **84**, 051309 (2011).

[222] A. Bulgac, M. Kafker, and I. Abdurrahman, "Measures of complexity and entanglement in many-fermion systems," Phys. Rev. C **107**, 044318 (2023).

[223] A. Bulgac, "New developments in fission studies within the time-dependent density functional theory framework," EPJ Web of Conferences **284**, 04001 (2023).

[224] J. M. Verbeke, J. Randrup, and R. Vogt, "Fission Reaction Event Yield Algorithm FREYA 2.0.2," Comp. Phys. Com. **222**, 263 (2018).

[225] C. Ishizuka, M. D. Usang, F. A. Ivanyuk, J. A. Maruhn, K. Nishio, and S. Chiba, "Four-dimensional Langevin approach to low-energy nuclear fission of ^{236}**U**," Phys. Rev. C **96**, 064616 (2017).

[226] J. Randrup, P. Möller, and A. J. Sierk, "Fission-fragment mass distributions from strongly

damped shape evolution," Phys. Rev. C **84**, 034613 (2011).

[227] J. Randrup and P. Möller, "Energy dependence of fission-fragment mass distributions from strongly damped shape evolution," Phys. Rev. C **88**, 064606 (2013).

[228] P. Möller, D. G. Madland, A. J. Sierk, and A. Iwamoto, "Nuclear fission modes and fragment mass asymmetries in a five-dimensional deformation space," Nature **409**, 785 (2001).

[229] Peter Möller, Arnold J. Sierk, and Akira Iwamoto, "Five-dimensional fission-barrier calculations from ^{70}Se to ^{252}Cf," Phys. Rev. Lett. **92**, 072501 (2004).

[230] D. D. Zhang, B. Li, D. Vretenar, T. Nikšić, Z. X. Ren, P. W. Zhao, and J. Meng, "Ternary quasifission in collisions of actinide nuclei," (2023), arXiv:2310.02657 [nucl-th].

[231] B. Li, D. Vretenar, T. Nikšić, J. Zhao, P. W. Zhao, and J. Meng, "Generalized time-dependent generator coordinate method for induced fission dynamics," Frontiers of Physics **19**, 44201 (2024).

[232] B. Li, D. Vretenar, Z. X. Ren, T. Nikšić, J. Zhao, P. W. Zhao, and J. Meng, "Fission dynamics, dissipation, and clustering at finite temperature," Phys. Rev. C **107**, 014303 (2023).

[233] Z. X. Ren, J. Zhao, D. Vretenar, T. Nikšić, P. W. Zhao, and J. Meng, "Microscopic analysis of induced nuclear fission dynamics," Phys. Rev. C **105**, 044313 (2022).

[234] Z. X. Ren, D. Vretenar, T. Nikšić, P. W. Zhao, J. Zhao, and J. Meng, "Dynamical Synthesis of ^{4}He in the Scission Phase of Nuclear Fission," Phys. Rev. Lett. **128**, 172501 (2022).

[235] G. Scamps, C. Simenel, and D. Lacroix, "Superfluid dynamics of ^{258}Fm fission," Phys. Rev. C **92**, 011602 (2015).

[236] Guillaume Scamps and Cédric Simenel, "Impact of pear-shaped fission fragments on mass-asymmetric fission in actinides," Nature **564**, 382–385 (2018).

[237] G. Scamps, D. Lacroix, G. F. Bertsch, and K. Washiyama, "Pairing dynamics in particle transport," Phys. Rev. C **85**, 034328 (2012).

[238] P. Calabrese and J. Cardy, "Evolution of entanglement entropy in one-dimensional systems," J. Stat. Mech **2005**, P04010 (2005).

[239] P. Calabrese and J. Cardy, "Time Dependence of Correlation Functions Following a Quantum Quench," Phys. Rev. Lett. **96**, 136801 (2006).

[240] V. Alba and P. Calabrese, "Entanglement and thermodynamics after a quantum quench in integrable systems," Proc. Natl. Acad. Sci. USA **114**, 7947 (2017).

[241] G. J. Milburn, J. Corney, E. M. Wright, and D. F. Walls, "Quantum dynamics of an atomic

Bose-Einstein condensate in a double-well potential," Phys. Rev. A **55**, 4318–4324 (1997).

[242] M. Chuchem, K. Smith-Mannschott, M. Hiller, T. Kottos, A. Vardi, and D. Cohen, "Quantum dynamics in the bosonic Josephson junction," Phys. Rev. A **82**, 053617 (2010).

[243] D. Cohen, V. I. Yukalov, and K. Ziegler, "Hilbert-space localization in closed quantum systems," Phys. Rev. A **93**, 042101 (2016).

[244] D. A. Abanin, E. Altman, I. Bloch, and M. Serbyn, "Colloquium: Many-body localization, thermalization, and entanglement," Rev. Mod. Phys. **91**, 021001 (2019).

[245] S. Sinha and S. Sinha, "Chaos and Quantum Scars in Bose-Josephson Junction Coupled to a Bosonic Mode," Phys. Rev. Lett. **125**, 134101 (2020).

[246] A. Del Maestro, H. Barghathi, and B. Rosenow, "Equivalence of spatial and particle entanglement growth after a quantum quench," Phys. Rev. B **104**, 195101 (2021).

[247] A. Del Maestro, H. Barghathi, and B. Rosenow, "Measuring postquench entanglement entropy through density correlations," Phys. Rev. Research **4**, L022023 (2022).

[248] M. Thamm, H. Radhakrishnan, H. Barghathi, B. Rosenow, and A. Del Maestro, "One-particle entanglement for one-dimensional spinless fermions after an interaction quantum quench," Phys. Rev. B **106**, 165116 (2022).

[249] R. P. Feynman, "Application of quantum mechanics to liquid helium II," Prog. Low Temp. Phys. **1**, 17 (1955).

[250] WF Vinen and JJ Niemela, "Quantum turbulence," Journal of low temperature physics **128**, 167–231 (2002).

[251] C. F. Barenghi, L. Skrebek, and K. R. Sreenivasa, "Introduction to quantum turbulence," Proc. Nat. Acad. Sci **111, No. suppl. 1**, 4647 (2014).

[252] Andrei Nikolaevich Kolmogorov, "Local structure of turbulence in an incompressible viscous fluid at very high reynolds numbers," Soviet Physics Uspekhi **10**, 734 (1968).

[253] D. Bandak, A. A. Mailybaev, G. L. Eyink, and N. Goldenfeld, "Spontaneous Stochasticity Amplifies Even Thermal Noise to the Largest Scales of Turbulence in a Few Eddy Turnover Times," Phys. Rev. Lett. **132**, 104002 (2024).

[254] J. v. Neumann, "Beweis des Ergodensatzes und desH-Theorems in der neuen Mechanik," Zeitschrift für Physik **57**, 30 (1929).

[255] J. von Neumann, "Proof of the ergodic theorem and the H-theorem in quantum mechanics," The European Physical Journal H **35**, 201 (2010).

[256] M. Srednicki, "Entropy and area," Phys. Rev. Lett. **71**, 666 (1993).

[257] M. Srednicki, "Chaos and quantum thermalization," Phys. Rev. E **50**, 888 (1994).

[258] M. Horoi, V. Zelevinsky, and B. A. Brown, "Chaos vs Thermalization in the Nuclear Shell Model," Phys. Rev. Lett. **74**, 5194 (1995).

[259] S. Goldstein, J. L. Lebowitz, R. Tumulka, and N. Zanghì, "Long-time behavior of macroscopic quantum systems," The European Physical Journal H **35**, 173 (2010).

[260] M. Rigol and M. Srednicki, "Alternatives to Eigenstate Thermalization," Phys. Rev. Lett. **108**, 110601 (2012).

[261] C. Murthy, A. Babakhani, F. Iniguez, M. Srednicki, and N. Yunger Halpern, "Non-Abelian Eigenstate Thermalization Hypothesis," Phys. Rev. Lett. **130**, 140402 (2023).

[262] L. Boltzmann, "Weitere Studien über das Wärmegleichgewicht unter Gasmolekülen," Sitzungsberichte Akademie der Wissenschaften **66**, 275 (1872).

[263] A. A. Abrikosov, L. P. Gorkov, and I. E. Dzyaloshinski, *Methods of Quantum Field Theory in Statistical Physics* (Prentice Hall, 1963).

[264] L.D. Landau and E. M. Lifshitz, *Physical Kinetics*, Vol. 10 (Pergamnon Press, Oxford, England, 1981).

[265] G. Lindblad, "On the Generators of Quantum Dynamical Semigroups," Communications in Mathematical Physics **48**, 119–130 (1976).

[266] V. Gorini, A. Kossakowski, and E. C. G. Sudarshan, "Complete positive dynamical semigrouos of N-level systems," Journal of Mathematical Physics **17**, 821–825 (1976).

[267] Allan Griffin, Tetsuro Nikuni, and Eugene Zaremba, *Bose-condensed gases at finite temperatures* (Cambridge University Press, 2009).

[268] Eugene P Gross, "Structure of a quantized vortex in boson systems," Il Nuovo Cimento (1955-1965) **20**, 454–477 (1961).

[269] Lev P Pitaevskii, "Vortex lines in an imperfect bose gas," Sov. Phys. JETP **13**, 451–454 (1961).

[270] Sir H. Lamb, *Hydrodymamics* (Cambridge University Press, 1975).

[271] L. D. Landau and E. M. Lifshitz, *Fluids Mechanics*, Course of Theoretical Physics, Vol. 6 (Pergamon Press, New York, 1959).

[272] G. B. Whitham, *Linear and nonlinear waves* (Willey & Sons, Inc., 1974).

[273] A. Bulgac, M. M. Forbes, and P. Magierski, "The unitary Fermi gas: From Monte Carlo to

density functionals," Chap. 9, pp. 305–374, vol. 836 of [179] (2012).

[274] Y. Castin and F. Werner, "The Unitary Fermi Gas and its Symmetry Properties," Chap. 5, pp. 127 – 191, vol. 836 of [179] (2012).

[275] H. A. Bethe, "Theory of the effective range in nuclear scattering," Phys. Rev. **76**, 38 (1949).

[276] A. Bulgac, J. E. Drut, and P. Magierski, "Spin 1/2 Fermions in the Unitary Regime: A Superfluid of a New Type," Phys. Rev. Lett. **96**, 090404 (2006).

[277] P. Magierski, G. Wlazłowski, and A. Bulgac, "Onset of a Pseudogap Regime in Ultracold Fermi Gases," Phys. Rev. Lett. **107**, 145304 (2011).

[278] A. Bulgac, M. M. Forbes, and W. Wlazłowski, "Towards quantum turbulence in cold atomic fermionic superfluids," J. Phys. B: At. Mol. Opt. Phys. **50**, 014001 (2016).

[279] L. P. Gorkov, "On the Energy Spectrum of Superconductors," Sov. Phys. JETP **7**, 505 (1958).

[280] L. P. Gorkov, "Developing BCS ideas in the former Soviet Union, ," in *BCS: 50 Years, Developing BCS ideas in the former Soviet Union*, edited by L. N. Cooper and D. Feldman (World Scientific, 2011) p. 107.

[281] A. Bulgac, "Entanglement entropy, single-particle occupation probabilities, and short-range correlations," Phys. Rev. C **107**, L061602 (2023).

[282] "W-SLDA Toolkit," (2023).

[283] A. Bulgac, Y.-L. Luo, P. Magierski, K. J. Roche, and Y. Yu, "Real-Time Dynamics of Quantized Vortices in a Unitary Fermi Superfluid," Science **332**, 1288 (2011).

[284] "Online supplement to A. Bulgac *et al.*, Science, 332, 1288 (2011), http://faculty.washington.edu/bulgac//UFG/,".

[285] A. Bulgac, M. M. Forbes, M. M. Kelley, K. J. Roche, and G. Wlazłowski, "Quantized Superfluid Vortex Rings in the Unitary Fermi Gas," Phys. Rev. Lett. **112**, 025301 (2014).

[286] G. Wlazłowski, A. Bulgac, M. M. Forbes, and K. J. Roche, "Life cycle of superfluid vortices and quantum turbulence in the unitary Fermi gas," Phys. Rev. A **91**, 031602 (2015).

[287] G. Wlazłowski, K. Sekizawa, M. Marchwiany, and P. Magierski, "Suppressed solitonic cascade in spin-imbalanced superfluid fermi gas," Phys. Rev. Lett. **120**, 253002 (2018).

[288] K. Hossain, K. Kobuszewski, M. M. Forbes, P. Magierski, K. Sekizawa, and G. Wlazłowski, "Rotating quantum turbulence in the unitary Fermi gas," Phys. Rev. A **105**, 013304 (2022).

[289] A. Barresi, A. Boulet, P. Magierski, and G. Wlazłowski, "Dissipative dynamics of quantum vortices in fermionic superfluid," Phys. Rev. Lett. **130**, 043001 (2023).

[290] G. Wlazłowski, M. M. Forbes, S. R. Sarkar, A. Marek, and M. Szpindler, "Fermionic quantum turbulence: Pushing the limits of high-performance computing," PNAS Nexus **3**, 160 (2024).

[291] A. Bulgac, M. Kafker, I. Abdurrahman, and G. Wlazlowski, "Quantum turbulence, superfluidity, non-markovian dynamics, and wave function thermalization," (2024), arXiv:2406.00926.

[292] L. N. Oliveira, E. K. U. Gross, and W. Kohn, "Density-functional theory for superconductors," Phys. Rev. Lett. **60**, 2430 (1988).

[293] Erich Runge and E. K. U. Gross, "Density-functional theory for time-dependent systems," Phys. Rev. Lett. **52**, 997–1000 (1984).

[294] M. J. H. Ku, A. T. Sommer, L. W. Cheuk, and M. W. Zwierlein, "Revealing the Superfluid Lambda Transition in the Universal Thermodynamics of a Unitary Fermi Gas," Science **335**, 563 (2012).

[295] Waseem S Bakr, Jonathon I Gillen, Amy Peng, Simon Fölling, and Markus Greiner, "A quantum gas microscope for detecting single atoms in a hubbard-regime optical lattice," Nature **462**, 74–77 (2009).

[296] M.N. Butler, D.W.L. Sprung, and J. Martorell, "An improved approximate treatment of c.m. motion in DDHF calculations," Nucl. Phys. A **422**, 157 (1984).

[297] G. Gamow, "Mass Defect Curve and Nuclear Constitution," Proc. Roy. Soc. A **126**, 632 (1930).

[298] R. E. Peierls and J. Yoccoz, "The collective model of nuclear motion," Proc. Phys. Soc. A **70**, 381 (1957).

[299] J. A. Sheikh, J. Dobaczewski, P. Ring, L. M .Robledo, and C. Yannouleas, "Symmetry restoration in mean-field approaches," Journal of Physics G: Nuclear and Particle Physics **48**, 123001 (2021).

[300] JF Berger, M Girod, and D Gogny, "Microscopic analysis of collective dynamics in low energy fission," Nuclear Physics A **428**, 23–36 (1984).

[301] P. Da Costa, K. Bennaceur, J. Meyer, W. Ryssens, and M. Bender, "Impact of choices for center-of-mass correction energy on the surface energy of Skyrme energy density functionals," Phys. Rev. C **109**, 034316 (2024).

[302] Jacek Dobaczewski, "Lipkin translational-symmetry restoration in the mean-field and energy–density-functional methods," J. Phys. G: Nucl. Part. Phys. **36**, 105105 (2009).

[303] MN Butler, DWL Sprung, and J Martorell, "An improved approximate treatment of cm

motion in ddhf calculations," Nuclear Physics A **422**, 157–166 (1984).

[304] Hendrik Schatz, Ani Aprahamian, Joachim Görres, Michael Wiescher, Thomas Rauscher, Jan-Felix Rembges, F-K Thielemann, Bernd Pfeiffer, Peter Möller, K-L Kratz, *et al.*, "rp-process nucleosynthesis at extreme temperature and density conditions," Physics reports **294**, 167–263 (1998).

[305] H. Schatz, A. Aprahamian, V. Barnard, L. Bildsten, A. Cumming, M. Ouellette, T. Rauscher, F.-K. Thielemann, and M. Wiescher, "End point of the *rp* process on accreting neutron stars," Phys. Rev. Lett. **86**, 3471–3474 (2001).

[306] M.R. Mumpower, R. Surman, G.C. McLaughlin, and A. Aprahamian, "The impact of individual nuclear properties on r-process nucleosynthesis," Prog. Part. Nucl. Phys. **86**, 86 (2016).

[307] J. J. Cowan, C. Sneden, J. E. Lawler, A. Aprahamian, M. Wiescher, K. Langanke, G. Martínez-Pinedo, and F.-K. Thielemann, "Origin of the heaviest elements: The rapid neutron-capture process," Rev. Mod. Phys. **93**, 015002 (2021).

[308] R.E. Peierls and D.J. Thouless, "Variational approach to collective motion," Nucl. Phys. **38**, 154 (1962).

[309] S. Marcos, H. Flocard, and P.-H. Heenen, "Calculation of the Peierls-Yoccoz translational mass for Hartree-Fock wave functions," Phys. Lett. B **134**, 287 (1984).

[310] K. W. Schmid and F. Grümmer, "Translationally invariant treatment of the charge density in nuclei," Zeit. Phys. A **337**, 267 (1990).

[311] K.W. Schmid and P.-G. Reinhard, "Center-of-mass projection of Skyrme-Hartree-Fock densities," Nucl. Phys. A **530**, 283 (1991).

[312] K. W. Schmid, "Some considerations on the restoration of Galilei invariance in the nuclear many-body problem," Eur. Phys. J. A **14**, 413 (2002).

[313] R. R. Rodríguez-Guzmán and K. W. Schmid, "Spherical Hartree-Fock calculations with linear-momentum projection before the variation," Eur. Phys. J. A **19**, 45 (2004).

[314] K.W. Schmid, "On the use of general symmetry-projected Hartree–Fock–Bogoliubov configurations in variational approaches to the nuclear many-body problem," Prog. Part. Nucl. Phys. **52**, 565 (2004).

[315] N. W. Aschroft and N. D. Mermin, *Solid State Physics* (Saunders College, 1976).

[316] E. P. Segarra, J. R. Pybus, F. Hauenstein, D. W. Higinbotham, G. A. Miller, E. Piasetzky, A. Schmidt, M. Strikman, L. B. Weinstein, and O. Hen, "Short-range correlations and the

nuclear EMC effect in deuterium and helium-3," Phys. Rev. Res. **3**, 023240 (2021).

[317] A. W. Denniston, T. Ježo, A. Kusina, N. Derakhshanian, P. Duwentäster, O. Hen, C. Keppel, M. Klasen, K. Kovařík, J. G. Morfín, K. F. Muzakka, F. I. Olness, E. Piasetzky, P. Risse, R. Ruiz, I. Schienbein, and J. Y. Yu., "Modification of Quark-Gluon Distributions in Nuclei by Correlated Nucleon Pairs," Phys. Rev. Lett. **133**, 152502 (2024).

[318] P.-O. Löwdin, "Quantum Theory of Many-Particle Systems. II. Study of the Ordinary Hartree-Fock Approximation," Phys. Rev. **97**, 1490 (1955).

[319] W. Kohn and L. J. Sham, "Self-Consistent Equations Including Exchange and Correlation Effects," Phys. Rev. **140**, A1133 (1965).

[320] M. A. L. Marques, C. A. Ullrich, F. Nogueira, A. Rubio, K. Burke, and E. K. U. Gross, eds., *Time-Dependent Density Functional Theory*, Lecture Notes in Physics, Vol. 706 (Springer-Verlag, Berlin, 2006).

[321] M. A. L. Marques, N. T. Maitra, F. M. S. Nogueira, E. K. U. Gross, and A. Rubio, eds., *Fundamentals of Time-Dependent Density Functional Theory*, Lecture Notes in Physics, Vol. 837 (Springer, Heidelberg, 2012).

[322] R. Somasundaram, J. E. Lynn, L. Huth, A. Schwenk, and I. Tews, "Maximally local two-nucleon interactions at N^3LO in Δ-less chiral effective field theory," Phys. Rev. C **109**, 034005 (2024).

[323] A. Tichai, P. Arthuis, K. Hebeler, M. Heinz, J. Hoppe, T. Miyagi, A. Schwenk, and L. Zurek, "Randomized low-rank decompositions of nuclear three-body interactions," Phys. Rev. Res. **6**, 043331 (2024).

[324] B. Hu, W. Jiang, T. Miyagi, Z. Sun, A. Ekstroem, C. Forssen, G. Hagen, J. D. Holt, T. Papenbrock, S. R. Stroberg, and I. Vernon, "Ab initio predictions link the neutron skin of 208 Pb to nuclear forces (vol 18, pg 1196, 2022)," Nature Physics **18**, 1196 (2024).

[325] A. J. Tropiano, S. K. Bogner, R. J. Furnstahl, and M. A. Hisham, "Quasi-deuteron model at low renormalization group resolution," Phys. Rev. C **106**, 024324 (2022).

[326] A.J. Tropiano, S.K. Bogner, R.J. Furnstahl, M.A. Hisham, A. Lovato, and R.B. Wiringa, "High-resolution momentum distributions from low-resolution wave functions," Phys. Lett. B **852**, 138591 (2024).

[327] D. Lonardoni, A. Lovato, Steven C. Pieper, and R. B. Wiringa, "Variational calculation of the ground state of closed-shell nuclei up to $a = 40$," Phys. Rev. C **96**, 024326 (2017).

[328] Aurel Bulgac, "A critical assessment of the current implementations of the generator coordinate method," (2025), arXiv:2408.02173 [nucl-th].

[329] James J. Griffin and John A. Wheeler, "Collective motions in nuclei by the method of generator coordinates," Phys. Rev. **108**, 311–327 (1957).

[330] P. G. Reinhard, R.Y Cusson, and K. Goeke, "Time evolution of coherent ground-state correlations and the tdhf approach," .